UNIVERSITY OF OKLAHOMA

GRADUATE COLLEGE

RAPID FABRICATION OF FLEXIBLE CARBONACEOUS NANOCOMPOSITES FOR HUMAN MOTION DETECTION AND OIL SPILL CLEANUP

A DISSERTATION

SUBMITTED TO THE GRADUATE FACULTY

in partial fulfillment of the requirements for the

Degree of

DOCTOR OF PHILOSOPHY

By

BLAKE HERREN
Norman, Oklahoma
2021

RAPID FABRICATION OF FLEXIBLE CARBONACEOUS NANOCOMPOSITES FOR

HUMAN MOTION DETECTION AND OIL SPILL CLEANUP

A DISSERTATION APPROVED FOR THE
SCHOOL OF AEROSPACE AND MECHANICAL ENGINEERING

BY THE COMMITTEE CONSISTING OF

Dr. Yingtao Liu, Chair

Dr. Mrinal C. Saha, Co-Chair

Dr. M. Cengiz Altan

Dr. Binbin Weng

© Copyright by BLAKE HERREN 2021

All Rights Reserved.

DEDICATION

I dedicate this dissertation to my family, my mother Lisa, my father Kent, and my brother Zach. I also dedicate this dissertation to my girlfriend Sophia Lee. Without all your support and love I could have never accomplished my dreams that have begun to take shape. Thank you.

ACKNOWLEDGEMENTS

First, I would like to give my sincerest gratitude to my advisor Dr. Yingtao Liu for giving me this opportunity to grow as an engineering researcher in his lab at the University of Oklahoma (OU). Your ability to create an extremely supportive environment while also pushing me to reach my potential was exactly what I needed to develop a creative problem-solving skillset, and your guidance, advice, and teachings will stick with me for a lifetime. I will be forever grateful for you taking a chance on me and changing my life path for the better. I would also like to thank my Co-advisor Dr. Mrinal C. Saha and my committee members Dr. M. Cengiz Altan and Dr. Binbin Weng for their tremendous support for my research through the years. Your input, direction, and encouragement have helped me tremendously in accomplishing my goals in graduate school. I would also like to thank everyone at the School of Aerospace and Mechanical Engineering (AME) at OU. The AME staff including Billy Mays, Greg Williams, Bethany Burkland, Melissa Foster, Ellen McKenzie, and Martina Ferguson. Your friendships and advice I will always remember and cherish, and your hard work and dedication keeps AME the best school at OU! I also want to thank my close friends that I have gained through working in the lab at OU. Ben Hoelzel, Noah Golly, Ryan Cowdrey, Weston Sleeper, Colin Bray, Antonio Santiago, Mohammad Charara, Jingyu Wang, Jishan Luo, and Chris Billings, you have all made graduate school a time I will remember fondly because of the friendships and memories we made in the basement of Felgar Hall. A special thanks to my girlfriend Sophia Lee who has been there for me through the toughest of times and the best of times. I do not know how I could have made it through graduate school without your gracious encouragement and love. You made graduate school a time I will miss dearly. I also want to thank my mother Lisa, father Kent, and brother Zach for their love and for allowing me to be selfish with my time in graduate school to accomplish my goals. Thank you all very much!

TABLE OF CONTENTS

ABSTRACT

In this work, flexible carbonaceous nanocomposites are fabricated via microwave irradiation, direct ink writing (DIW), and a porogen mixing method to develop multifunctional devices. A thermoset elastomer (silicone rubber), carbon nanotubes (CNTs), and carbon black (CB) are the primary materials used for samples in this work. The effects of microwave-curing in comparison to traditional thermal-curing of polydimethylsiloxane (PDMS) containing dispersed CNTs are explored. Microwave-curing proves to enhance the electrical conductivity of the lowest conductive loading of nanocomposites by almost 150 % due to CNT dispersion and alignment improvements. In addition, the rapid curing procedure reduces the curing time by at least 96 %, lowers the modulus, and unaffected the compressive piezoresistive sensitivity of the material. Ecoflex silicone rubber is used to develop skin-attachable sensors for human motion detection. A DIW method known as embedded 3D printing (e-3DP) is employed to fabricate these sensors and tailor the sensitivity. Nanocomposite PDMS sponges are fabricated by mixing the prepolymer with sugar or salt porogen. The sponge sensors demonstrate useful piezoresistive behavior and embedded nanofiller for safe skin-attachable human motion detection. A nanocomposite PDMS sponge material is also investigated as a reusable sorbent material for oil/water separation. The oleophilic, hydrophobic, durability, and Joule heating properties of the sorbent sponge material are optimized for use in a cutting-edge sorbent-based oil skimmer (SOS) that is developed for continuous removal of oil spills. The SOS is a floating vessel containing a funnel-shaped sponge for continuous and efficient gravity-driven extraction of oil from the water surface. The SOS is used to extract fish tank-scale simulated oil spills. This work explores the rapid microwave-based fabrication of carbonaceous elastomeric nanocomposites and develops strain sensing devices for human motion monitoring and oil sorbents for the efficient removal of oil spills from water.

LIST OF TABLES

LIST OF FIGURES

CHAPTER 1: INTRODUCTION

1.1 Nanocomposite Development

Nanocomposite development typically includes incorporating nanomaterials into a matrix of standard material to impart improved properties or multifunctionality such as semiconductivity. In this work, polymer matrix nanocomposites were explored with a focus on carbonaceous elastomeric nanocomposites consisting of a thermoset elastomer matrix (i.e., silicone rubber) and carbon nanotubes (CNTs) or carbon black (CB) as the nanofiller. Various fabrication methods were used and developed in this work to decrease the fabrication time, enhance the dispersion and/or alignment of the nanofiller for improved properties, and control the geometry of the nanocomposites for innovative applications. The nanofiller played a vital role in both the functionality of the fabricated samples and the rapid fabrication methods. In this section, a relevant background of nanocomposites is provided.

1.1.1 Conductive Nanocomposites

Electrically conductive nanoparticles have been widely used in recent years as fillers in polymers to create conductive nanocomposites with versatile behavior for a wide variety of applications. Commonly used conductive nanoparticles including silver nanowires [1], gold nanowires [2], graphene [3], CB [4], carbon nanofibers [5-7], and CNTs [8-10] are typically either dispersed within a polymer matrix or attached to a substrate to fabricate nanocomposites with a wide variety of functions. Of these electrically conductive nanoparticles, CNTs have received widespread attention for their impressive properties. Many different polymers have been used as matrix

materials with dispersed CNTs to fabricate nanocomposites with improved mechanical [11], thermal [12], and electrical properties [13, 14]. Notably, CNTs have been utilized for many sensing applications including strain sensors [8], pressure sensors [15], gas sensors [16], and temperature sensors [17]. When CNTs are dispersed within a polymer matrix, the quality of dispersion and alignment have a substantial impact on the properties that they endow, including the sensing performance of the nanocomposites. Thus, substantial attention has been placed on improving the dispersion or controlling the alignment of these high aspect ratio nanoparticles to enhance the material properties or the functionality of the fabricated nanocomposite.

1.1.2 CNT Alignment

Due to the high-aspect-ratio of CNTs and their propensity to be dominated by van der Waals forces to form agglomerates, extensive consideration must be placed on achieving successful dispersion and controlling the relative alignment of the nanofiller. Different methods such as shear mixing, solvent-based ultrasonication, and chemical functionalization have been used to produce high-quality CNT dispersion in polymeric matrices [18]. In-situ alignment techniques include methods to achieve CNT alignment during the growing process, while ex-situ alignment techniques are implemented during the integration process of the CNTs [19]. Ex-situ alignment techniques include the use of electric fields [20, 21], magnetic fields [22], surface forces [23], acoustic waves [24], mechanical stretching [25, 26], and extrusion-based methods such as three-dimensional (3D) printing [27]. These techniques have proved useful to improve the CNT alignment in a chosen direction, often significantly enhancing the key material properties of the nanocomposite in the aligned direction of the heterogeneous microstructures [28].

1.1.3 Microwave-curing CNT Nanocomposites

Microwave-curing has emerged in recent years as an efficient method to cure composite laminates [29-31], thermoset resins [32], and has been proven beneficial in curing CNT doped epoxies with significantly reduced curing times and energy consumptions [33]. Due to their high microwave absorption performance, carbonaceous nanoparticles can be easily heated via microwave irradiation [34]. When exposed to microwave energy, CNTs experience significant heating effects that, when dispersed well within an uncured thermoset matrix, transfer localized heat to the matrix material inducing rapid polymerization of the nanocomposite. The mechanisms involved with microwave-induced heating of CNTs are not fully understood; however, the current explanation includes the CNTs transferring electromagnetic energy to mechanical vibrations and impurities in the nanoparticles producing Joule heating when subject to microwave irradiation [35, 36].

Notably, Chang et al. reported that microwave-curing of CNT-based epoxies resulted in alignment in some direction, shown by observing the significant difference in CNT pullout on two vertical fractures of their microwave-cured nanocomposites, compared to no differences seen in their thermally-cured samples [37]. In addition to CNT alignment induced by microwave irradiation, rapid polymerization via microwave-curing decreased the settlement effect of the CNTs improving the resulting dispersion within the cured nanocomposite. Both dispersion and CNT alignment play a vital role in the key material properties of nanocomposites. Therefore, it is essential to examine the effects of microwave-curing these materials. Several efforts have focused on improving the conductivity of one-dimensional carbon nanoparticle-enhanced nanocomposites including adding secondary conductive nanofillers such as CB [38], melt annealing of carbon nanofiber-based thermoplastic nanocomposites [39], and investigating the impact of CNT waviness [40], aspect ratio [41, 42], and agglomerate content [41, 43] on electrical conductivity. Also, many studies have

investigated rapid microwave-curing CNT-based epoxy nanocomposites and investigated the effects on the mechanical properties of the fully cured samples [33, 37, 44-47]. While these studies have proven useful, not enough work has been done to explore the influence of rapid microwave-curing of nanocomposites containing dispersed CNTs on the materials' electrical conductivities and the impact on mechanical and piezoresistive properties of flexible nanocomposites.

1.1.4 Embedded 3D Printing

Recently, Muth et al. developed a well-known manufacturing process known as embedded 3D printing (e-3DP) where a conductive carbon grease was printed via direct ink writing (DIW) into an Ecoflex resin bath with modified rheology to fabricate highly stretchable piezoresistive strain sensors [48]. Robocasting, or DIW, is an extrusion-based additive manufacturing technique where a paste-like material is extruded from a reservoir through a nozzle. Due to shear forces applied in the nozzle during DIW, high aspect ratio nanoparticles may be aligned along the printing direction, resulting in tailorable microstructures in 3D printed nanocomposites for enhanced sensor performance [49]. Although Muth et al. reported a relatively high sensitivity, the liquid sensing element produced sensors less than ideal for repeated long-term use as the sample must be punctured to be used as a piezoresistive sensor. With this method, the sensing element would not be suitable for long-term sensing use. Therefore, it was necessary to investigate the e-3DP method to fabricate fully cured nanocomposite sensors in this work.

1.1.5 Nanocomposite Sponges

Introducing porosity in flexible nanocomposites has received considerable attention due to having many facile fabrication methods, the ability to enhance compressibility and sensitivity of the sensors, and increasing the usability for several applications [50, 51]. Sponges have been fabricated from several different materials to develop highly compressible nanocomposite sensors

and oil sorbents for oil/water separation. Often, the multifunctionality or enhanced performance of the flexible sponges was introduced through the dispersion of nanoparticles within a flexible matrix or attaching nanoparticles to the pore walls. Some of the most common nanocomposite sponge fabrication techniques include dip-coating a neat polymer sponge in a suspension of dispersed conductive nanoparticles [52-54], using a sugar templating method where a sugar cube is infiltrated with resin and used as a sacrificial porogen [5, 53, 55, 56], and mixing salt or sugar porogen with the nanocomposite prepolymer before curing [57, 58]. In this work, nanocomposite PDMS sponges were fabricated via mixing a nanocomposite prepolymer with a porogen. Nanofiller was embedded in the sponge matrix to avoid nanoparticle detachment that may degrade the long-term performance of the nanocomposite, endanger the user of the human motion detecting sensor, or contaminate the environment or extracted oil during oil spill cleanup applications.

1.2 Flexible Nanocomposite Devices

Nanocomposites are often investigated for their multifunctionality as their unique properties allow the material to perform many different applications. Smart materials, also called responsive or intelligent materials, are materials that have properties that change in response to external stimuli. Carbonaceous nanocomposites typically exhibit semiconductive behavior that can be easily measured, recorded, and utilized for multifunctionality. Flexible semiconductive materials have often been utilized as smart materials including piezoresistive sensing behavior such that the measured resistance of the material changes due to applied stress or strain. Semiconductivity also allows the materials to be heated with an applied electrical current known as resistive heating (Joule heating) that can be utilized for various applications including oil spill absorption. Herein, an appropriate background of flexible carbonaceous nanocomposite devices is discussed.

1.2.1 Piezoresistive Sensors

Flexible electrically conductive nanocomposite sensors have recently received wide interest in several fields including biomechanics [59], biomedical and prosthetic devices [60-63], soft robotics [64, 65], electromagnetic shielding [66], structural health monitoring [67, 68], and wearable sensors and electronics [8, 49, 69]. Wearable nanocomposite sensors typically have a significantly increased stretchability and sensing range often beyond 100 % strain, while traditional metal strain gauges are only able to measure up to 5 % strain [70]. Three sensing mechanisms are typically demonstrated by flexible sensors including capacitive [71], piezoelectric [72], and piezoresistive effects [73]. Piezoresistivity is more commonly implemented when developing these sensors due to facile signal collection and fabrication [74, 75]. Piezoresistivity sensitivity is measured as the change in resistance of the semiconductive material due to an applied deformation. Highly flexible piezoresistive compression or pressure sensors typically decrease resistance during applied compressive strain due to a decrease in contact resistance made with the electrode, geometric changes of the sensor increasing current flow through the semiconductor, and conductive nanoparticles moving closer together to form new conductive networks. Flexible piezoresistive tensile strain sensors typically increase resistance when stretched in tension due to geometric changes of the semiconductive material and the conductive nanofiller moving further apart. Piezoresistive sensors often require the use of electrically conductive nanoparticles that are well-dispersed or aligned within a polymer matrix to form a conductive network that can deform under applied loads and change the electrical resistance of the nanocomposite. Piezoresistive sensors have been used for broad applications including pressure sensor arrays [6, 75, 76], large human motion detecting devices [8, 77], and highly sensitive voice recognition and pulse measurement sensors [78].

Novel manufacturing methods have been developed in recent years to fabricate and tailor the properties of these nanocomposite sensors to obtain enhanced electrical conductivity, sensitivity, and compressibility. For example, the conductivity of CNT-based nanocomposites has been enhanced through CNT alignment techniques [28, 79, 80], the addition of secondary conductive filler materials [38, 81], and efforts to determine the effects of various CNT structures and dispersion states on the electrical properties of nanocomposites [13, 40, 82]. Additionally, several studies have increased the sensitivity of these sensors through advanced manufacturing techniques to initiate cracks [83, 84], wrinkle conductive microstructures [85], overlap CNT structures [86], and implement SiO_2 microparticles to break apart conductive networks [87]. Increasing the compressibility of these sensors has been accomplished by different methods to initiate porosity in the nanocomposite including utilizing commercially available sponge materials [88, 89] and a commonly used sugar templating fabrication process [5, 90]. While these manufacturing techniques have proven to be successful in improving the conductivity, sensitivity, and compressibility of piezoresistive sensors, the manufacturing methods are usually time-consuming, high-cost, and difficult to scale. Therefore, there remains much work to be done to develop manufacturing methods to enhance the performance of these semiconductive nanocomposites while keeping the fabrication process simple, fast, low-cost, and scalable. In this work, piezoresistive sensors fabricated via microwave-curing, e-3DP, and a simple sponge manufacturing technique were developed to investigate the potential benefits of these rapid fabrication methods.

1.2.2 Skin-attachable Sensors

Wearable sensors and smart devices have been developed for various applications including quantification of biochemical profiles of athletes, rehabilitation of elderly patients,

electromechanical detection of small physiological body movements such as blood flow, and human motion monitoring [91-94]. Wearable strain sensors have been developed to produce signals dependent on the tensile or compressive strain applied to the sensor [95-101]. One of the key challenges in wearable sensors is the ability to combine the desired sensing functionality with a satisfactory degree of integration with the body. Human motion sensors are often attached to the skin which requires the devices to be safe, flexible, and conform well to the body to avoid slippage and ensure functionality [65, 100, 102-104]. Silicone rubbers such as PDMS and Ecoflex are often used as either a polymer matrix or substrate material for these highly flexible devices [65, 83, 102-107]. Notably, the commonly used Sylgard 184 PDMS has a high Young's modulus between 0.4 MPa – 3.5 MPa [108] which prevents comfortable and reliable adhesion with skin [65]. In contrast, Ecoflex has a low elastic modulus typically between 100 kPa – 125 kPa [65, 109, 110], which is more appropriate for skin-attachable strain sensing applications. Recently, multiple skin-attachable and ultrastretchable strain sensors have been developed by dispersing conductive nanoparticles in an Ecoflex matrix and coating Ecoflex substrates with conductive surfaces such as gold nanosheets or graphite thin films [83, 103, 111, 112]. These sensors utilized the highly stretchable nature of Ecoflex and their selected conductive material to produce nanocomposites capable of detecting strain applied to the material through either piezoresistive or capacitive effects [113]. While these studies demonstrated manufacturing methods to fabricate durable sensors with impressive stretchability, the strain sensors usually suffered from low sensitivity and little to no ability to control the microstructure during manufacturing. Notably, several studies have used models and experimental results to prove that CNT alignment in the strain sensing direction enhanced piezoresistive sensitivity [114-116]. The e-3DP method was used in this work to fabricate skin-attachable piezoresistive sensors with beneficial CNT alignment.

1.2.3 Piezoresistive Sponges Sensors

Sponges made of PDMS have received significant attention for their biocompatibility and wide functionality including triboelectric generators [117], oil/water separation [118], and piezoresistive sensors [119]. Piezoresistive PDMS sponges have been widely developed for applications including detecting speaking, breathing, and large human motions [119]. Often these sensors were applied to the skin of a user which required the sensor to be safe for the individual to have in close contact despite being functionalized by nanoparticles like CNTs that are believed to be detrimental to human health [120]. Piezoresistive sponges with nanoparticles on the walls of the sensor have a high likelihood of nanoparticle detachment under dynamic loading which could prove to be dangerous for the user and likely detrimental to the durability of the sensor [53]. In contrast, when nanoparticles are embedded within the PDMS matrix, there is a significantly lower likelihood of nanoparticle detachment from the sensor during use, thus the sensor can be safely applied on the skin of a user for several sensing applications.

Many studies that involved manufacturing PDMS sponges mentioned removing sacrificial porogen like salt or sugar was a difficult and time-consuming process. Several researchers in the field do not report the required time to remove the porogen, while some mention soaking their samples in warm water or a solvent for many hours or days. Much work is needed to be done to develop simple and low-cost fabrication methods to reduce time requirements to manufacture flexible highly porous nanocomposites. To solve these problems, researchers can look to implement fabrication techniques that utilize the functionality of the nanomaterials to rapidly fabricate or enhance the nanocomposite. In this work, nanocomposite PDMS sponges were rapidly fabricated via mixing the prepolymer with porogen before curing and utilizing a novel microwave-

based porogen removal method. The sponges were investigated for both their piezoresistive functionality for human motion detection and sorbent properties for oil spill cleanup applications.

1.2.4 Oil Spills and Sorbents

Due to the massive amount of exploration, storage, and transportation of oils and organic solvents, accidental spills in bodies of water remain a global challenge. While the yearly number of oil spills has reduced significantly in recent years [121], the technologies used to clean up oil spills have not significantly improved. Chemical dispersants and in-situ burning methods have been widely used to manage oil spills, however, these methods have contributed to additional environmental problems and increased health risks for the workers involved [122, 123]. Mechanical methods used for removing oil spills from the water include booms to corral the oil, skimmers to extract the congregated oil slicks, and sorbent materials to soak up thin oil sheens. To extract oil from water, traditional oil skimmers require energy input to rotate a typically oleophilic media (belts, discs, drums, tubes, etc.) through the oil layer to transfer the oil to a collection chamber where it can be extracted with a pump. This energy-consuming oil/water separation mechanism makes traditional oil skimmers difficult to deploy, scale up, and are highly inefficient for extracting thin oil layers from water [124]. Sorbent materials in sheet form are often deployed by hand to absorb and separate thin oil sheens from water. Most sorbents used in the industry today are single-use and account for significant solid waste that often far outweighs the liquid waste of the oil spill itself, with ratios as high as 400:1 [125]. This problem has made reusable and high sorption capacity sorbent materials a prominent field of research today.

Several researchers in the field have focused on modifying the surface of highly porous substrates to improve the hydrophobic and oleophilic properties of sorbent materials [126]. Desired characteristics of state-of-the-art oil/water separation materials include lightweight with high oil

sorption capacities, super-hydrophobicity, durability, reusability, low-cost, and facile fabrication [127]. Advanced sorbent materials have also been developed to include unique functionalities including resistance to ultrahigh temperatures for in-situ oil burn-off from the sorbent [128], magnetism to facilitate sorbent recovery via magnets [129, 130], and stimuli-responses such as Joule heating and photothermal effect for viscous oil absorption [131-133]. Joule heating a semiconductive sorbent material is arguably the most applicable and versatile of these advanced sorbent features to heat and lower the viscosity of nearby oils to facilitate rapid absorption of highly viscous pollutants. However, little work has been done to scale up these state-of-the-art sorbent materials by utilizing low-cost materials and facile fabrication methods.

The most promising sorbent-based technologies to reduce the amount of manual labor required and solid waste produced from oil spill cleanup includes oil collecting vessels and oil extraction devices [127]. The goal of these devices is to utilize the properties of the sorbent materials to collect the oil in a container or continuously extract the oil. The simplest of these devices includes placing a tube into the center of a sorbent, such as an oleophilic and hydrophobic sponge, and pumping to continuously extract the oil through the sorbent [134-136]. However, the oil extraction rate is extremely slow using this technique and often results in some water extracted through the sponge [137]. Vessel-type oil collectors utilize a sorbent material and gravity (or an external force) to fill an oil collection chamber or vessel [138-141]. A few studies have demonstrated the ability to remove oil collected in these sorbent-based devices with a pump for brief small-scale demonstrations [142-144]. However, to the best of the author's knowledge, no previous study has developed a fully reusable floating vessel-type device with continuous oil extraction capabilities. In this work, a novel device consisting of a funnel-shaped sponge with Joule heating sorption functionality in a floating vessel was developed and tested as a gravity-driven oil skimmer.

1.3 Scope of Work

The primary focus of this work was to explore the rapid fabrication of flexible carbonaceous nanocomposite devices for large strain sensing and oil spill cleanup applications. The material makeup of the fabricated samples and devices in this work remained consistent throughout including silicone rubber and dispersed carbonaceous nanoparticles. The rapid microwave-curing of PDMS containing dispersed CNTs was deeply investigated. Skin-attachable nanocomposite sensors for human motion monitoring were explored. Lastly, a novel gravity-driven oil skimmer consisting of a reusable funnel-shaped sponge and a floating vessel was developed to continuously extract oil from the water surface. This work has significance in the fields of elastomeric nanocomposites, rapid curing thermoset resins, additive manufacturing, highly flexible sensors, and oil spill cleanup technologies.

1.4 Objectives

The three main research objectives of this work are as follows:

I. Investigate the effects of rapid microwave-curing thermoset elastomer nanocomposites containing dispersed CNTs compared to traditional thermal-curing.

II. Fabricate and test highly flexible skin-attachable piezoresistive sensors that are safe for users and perform well for human motion detection.

III. Develop a novel funnel-shaped floating vessel oil skimmer with Joule heating sorption functionality for highly efficient oil spill cleanup applications.

CHAPTER 2: MICROWAVE-CURING NANOCOMPOSITES

2.1 Introduction

2.1.1 Motivation

The microwave-curing studies in this work were initiated after reading literature that CNTs superheat under microwave irradiation and have been dispersed in epoxy resins to reduce the time required to harden the resin via microwave-curing. However, no previous study had investigated microwave-curing a thermoset elastomer nanocomposite ink containing dispersed CNTs. Rapid curing may be useful for thermoset DIW 3D printing, thus investigating the rapid microwave-curing of a CNT-based silicone rubber nanocomposite aligned with my interests in additive manufacturing. Additionally, our lab observed that thermosets containing low-loadings of CNTs required extremely long curing times in the oven. Microwave-curing was thought to potentially be a solution to this problem and could help increase the rate of production in the future mass manufacturing of these materials. Therefore, studying the microwave-curing of CNT-based elastomeric nanocomposites was determined to be a valuable pursuit. The work in this chapter has resulted in two journal publications on microwave-curing PDMS nanocomposites [145, 146].

2.1.2 Background

In this study, the microwave-curing effects on the electrical, mechanical, and piezoresistive properties of PDMS nanocomposites containing dispersed multi-walled CNTs were investigated. Cylindrical nanocomposites were fabricated using both microwave-curing and thermal-curing methods. During the microwave-curing procedure, temperature measurements were taken between

each pulse of the microwave to investigate the rate of temperature increase. Their mechanical, electrical, and piezoresistive properties were compared. The quality of CNT dispersion within the nanocomposites was investigated with a scanning electron microscope (SEM). Cyclic compressive tests were conducted to determine the effects of the curing process on the materials' compressive moduli. The piezoresistive sensing responses of the nanocomposites cured with each curing method were compared by testing the samples under cyclic loads up to 20 % compressive strain. Next, the lowest conductive CNT loading was selected to investigate the potential for microwave-curing parameters to further enhance the electrical conductivity of the nanocomposites. After the optimal microwave parameters were established for curing the lowest loading conductive material, a final conductivity comparison was made with the thermal-curing method again to quantify the improvement of electrical conductivity made from the microwave-curing optimization process. The piezoresistive behaviors of the 1 wt% microwave-cured sensors were fully characterized through a series of cyclic tests with various strain rates, long-term sensing durability tests, and viscoelastic creep tests. Lastly, the developed nanocomposite sensors were demonstrated as wearable sensor arrays for human motion detection.

2.2 Experimental Methods

2.2.1 Materials

All materials were used as received from the suppliers unless otherwise stated. The tetrahydrofuran (THF) used for the solvent-based nanoparticle dispersion method was purchased from Sigma-Aldrich. The Sylgard 184 PDMS kit is a two-part PDMS including the base elastomer (part A) and curing agent (part B) which was purchased from Dow Corning. The multi-walled CNTs were purchased from Sigma-Aldrich and had a diameter between 50 – 90 nm and aspect ratios > 100.

2.2.2 Nanoparticle Dispersion

To sufficiently disperse the conductive nanoparticles throughout the elastomeric matrix, a solvent-based ultrasonication method was used. First, a predetermined amount of CNTs were mixed in 30 mL of THF with a magnetic stir bar at 350 rpm for 5 min to wet the nanoparticles. Then the CNT/THF mixture was sonicated with a 750-watt probe tip sonicator for 10 min to break apart the CNT agglomerates. Concurrently, a predetermined amount of the PDMS part A and 20 mL of THF were mixed with a magnetic stir bar at 350 rpm for 3 min to fully dissolve the base elastomer and lower the viscosity to allow for successful nanoparticle dispersion. Next, the CNT/THF mixture was added to the PDMS/THF solution and mixed with a stir bar at 350 rpm for 5 min. This mixture was sonicated for 30 min to successfully disperse the CNTs within the PDMS part A. Then the PDMS/CNT/THF mixture was mixed with a magnetic stir bar at 350 rpm on a 70 °C hot plate to evaporate most of the THF. Once the stir bar was no longer able to rotate due to the decreased amount of THF and high viscosity of the nanocomposite resin, the stir bar was removed, and the mixture was placed in a vacuum oven at 70 °C overnight to completely remove residual THF. Each batch of material prepared resulted in 15 g of PDMS/CNT resin including only the PDMS part A and dispersed CNTs.

2.2.3 Nanocomposite Sample Fabrication

The cylindrical microwave-cured PDMS/CNT (m-PDMS/CNT) and thermally-cured PDMS/CNT (t-PDMS/CNT) samples were fabricated using the method described in the schematic shown in Figure 2.1. To compare the compressive moduli, electrical conductivities, and piezoresistive sensitivities of nanocomposites fabricated with the microwave-curing method and thermal-curing of the PDMS/CNT nanocomposites, five batches of material with CNT loadings between 0.5 wt% - 2.5 wt% were prepared. Each batch of material was used to fabricate four t-PDMS/CNT and four

m-PDMS/CNT samples. After the CNTs were dispersed in the PDMS base elastomer using the solvent-based dispersion method described above, the PDMS/CNT was removed from the oven and allowed to cool to room temperature before adding the PDMS part B to the nanocomposite at a 1:10 curing agent to base polymer ratio. The curing agent was thoroughly hand-mixed into the nanocomposite resin for 5 min and then degassed in a vacuum chamber for 1 h to remove air bubbles. Then the nanocomposite prepolymer was loaded into a 3 mL syringe either through the open tip of the syringe with the plunger for lower viscosity resins, or the plunger was removed, and the higher viscosity resins were loaded in the larger back opening of the syringe.

To fabricate m-PDMS/CNT, a cylindrical glass mold (diameter = 11 mm, height = 9 mm) was filled with the PDMS/CNT prepolymer using the syringe, then the top surface was smoothed with a straight edge. The uncured nanocomposite resin in the glass mold was placed in the center of an unmodified 2.2 cubic feet General Electric 1200-watt microwave (inverter type) and rapidly cured via microwave irradiation. The microwave was run at 20 % power and pulsed on for a variable amount of time depending on the CNT loading and pulsed off for 10 s to take temperature readings with a Fluke Ti25 Thermal Imager. The number of pulse cycles and on time per cycle to fabricate the m-PDMS/CNT samples for 0.5 wt%, 1 wt%, 1.5 wt%, 2 wt%, and 2.5 wt% loadings of the nanocomposite were 4 pulses of 120 s, 3 pulses of 30 s, 3 pulses of 25 s, 3 pulses of 20 s, and 4 pulses of 15 s, respectively (Table 2.1). Many of the samples experienced a small amount of deformation above the top surface of the mold due to thermal shock. Therefore, the expanded top surface of each microwave-cured sample was removed with a razor blade to create a flat surface to facilitate material property characterization tests and expose the embedded CNTs for SEM imaging.

Table 2.1: *Microwave-curing parameters used for various loadings of PDMS/CNT.*

CNT (wt%)	Microwave power (%)	Number of pulses	Time on (s)	Time off (s)
0.5	20	4	120	10
1	20	3	30	10
1.5	20	3	25	10
2	20	3	20	10
2.5	20	4	15	10

To compare microwave-curing and thermal-curing of the nanocomposites, an aluminum mold was manufactured with a CNC milling machine to approximately the same size and shape as the glass mold used for microwave-curing. During the mold loading procedure, one loaded syringe was used to fill one glass mold and one aluminum mold with PDMS/CNT prepolymer, alternating the order to ensure a fair comparison. The aluminum mold containing all four samples was placed in a 150 °C oven right before beginning to fabricate the m-PDMS/CNT samples one at a time. The oven curing times for the t-PDMS/CNT samples with 0.5 wt%, 1 wt%, 1.5 wt%, 2 wt%, and 2.5 wt% CNT loadings were 30 min, 1 h, 3 h, 5 h, and 7 h respectively.

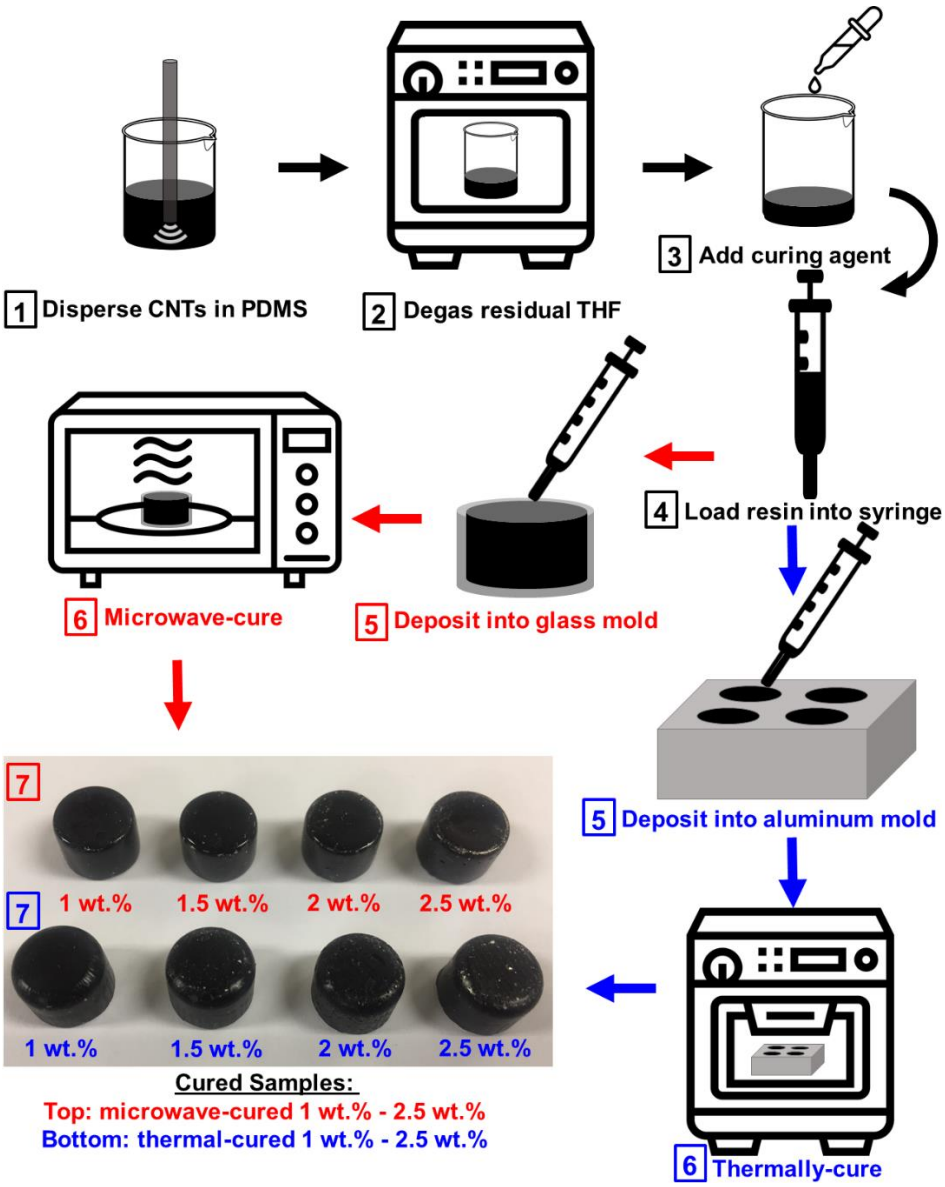

Figure 2.1: *Schematic illustration of the sample fabrication method for m-PDMS/CNT and t-PDMS/CNT.*

2.2.4 Porosity Measurements and SEM Imaging

Microwave-cured nanocomposites containing CNT concentrations of 1 wt% and 2.5 wt% were imaged via SEM. A Zeiss Neon EsB SEM was used to study CNT dispersion and pores that remained in the nanocomposites. The topography of the bottom surface of 1 wt% m-PDMS/CNT and 1 wt% t-PDMS/CNT were imaged to characterize the surface impact of the glass and

aluminum molds. All the samples were sputter-coated before SEM imaging with about 5 nm of AuPd to reduce potential charging effects and aid in imaging. The volume of each sample was determined by measuring the diameter and height of each cylindrical sample with a caliper and micrometer. The mass of each sample was measured with a digital scale then the porosity of each sample was calculated with these measurements.

2.2.5 Key Properties Comparison of Curing Methods

The resistance of each sample was first measured using an Instron 3345 single column mechanical testing machine and an Agilent 34401a multimeter. Each sample was placed in between two copper plates soldered to wires connected to the multimeter, and a 2 N load was applied in compression to ensure complete contact with the nanocomposite sample. The resistance was averaged over 1 min after the measurement had adequately stabilized. Next, a layer of silver epoxy and the copper tape was applied to each flat surface of the nanocomposite samples and allowed to harden. The resistance of the sample excluding the contact resistance between two copper plates was measured by clamping both extended ends of the copper tape to the multimeter and waiting for the resistance measurement to stabilize before averaging over 1 min. The reported contact resistance was the first measured resistance between the copper plates subtracted by the second measured resistance using the attached silver epoxy and copper tape. The conductivity of each sample was calculated from the resistance measured with the silver epoxy and copper tape.

The compressive moduli of the nanocomposites manufactured by the two curing methods were tested under compressive loads up to a maximum strain of 10 % for 20 cycles. Next, the piezoresistive sensing responses of both microwave-cured and thermally-cured nanocomposites with 1 wt% CNTs were tested under cyclic compressive loads on the Instron machine. Nanocomposite samples were tested for 20 cycles with a crosshead speed of 2 mm/min at each

maximum strain of 3 %, 5 %, 10 %, 15 %, and 20 % to evaluate their sensitivity by calculating the gauge factor at certain applied strains. Electrical resistance variation was continuously recorded during all the cyclic tests.

2.2.6 Microwave-Curing Optimization for Conductivity Enhancement

To investigate the optimal microwave settings for producing the highest conductivity m-PDMS/CNT samples with a 1 wt% CNT loading, two studies were performed varying the number of pulse cycles and the power of the microwave used to cure the samples. For each study, one batch of 1 wt% PDMS/CNT resin was prepared, as this was the lowest conductive loading of material found during the initial curing method comparison.

The pulse study was performed using a constant microwave power of 50 % and 10 s off was allowed between each pulse on to take temperature measurements. After filling three glass molds with uncured PDMS/CNT prepolymer, the m-PDMS/CNT samples were cured for 8 pulses of 5 s, 3 pulses of 10 s, and 1 pulse (one-step) of 20 s. This process was repeated four times producing a total of 12 samples with about 15 min between the fabrication of each set of samples.

The power study was completed using one-step microwave irradiation at microwave powers of 20 %, 50 %, and 80 %. Again, 12 total samples were prepared including one sample per power level in each set of samples and about 15 min between the fabrication of each set. Each sample from both the pulse study and power study was tested for their conductivity using silver epoxy and copper tape applied to both flat ends of the cylindrical nanocomposites.

To determine the maximum increase of conductivity using the optimal microwave-curing settings for the lowest conductive loading of PDMS/CNT, one batch of 1 wt% PDMS/CNT was prepared. The optimal microwave power and pulse settings (one-step at 50 % power) were used to cure four

samples of m-PDMS/CNT while simultaneously curing four t-PDMS/CNT samples in the oven at 150 °C for 1 h. During the loading procedure into the molds, one loaded syringe was used to fill one glass mold and one aluminum mold alternating the order for each set of samples. The conductivity of each prepared sample was measured using the two-probe method with silver epoxy and copper tape electrodes applied on both flat ends of the nanocomposites.

2.2.7 Characterization of Piezoresistive Sensor Properties

Detailed characterization on the piezoresistive sensing function of the microwave-cured nanocomposites with 1 wt% CNTs was performed through additional cyclic tests. These tests included investigating various strain rates, long-term durability tests up to 800 cycles, and viscoelastic creep tests to fully characterize the performance of the developed sensors under various load conditions. First, the nanocomposite sensors were compressed for 20 cycles of 10 % maximum strain and various strain rates including 5 %/min, 10 %/min, 25 %/min, 50 %/min, 100 %/min, and 200 %/min. Next, the piezoresistive sensors were tested up to 800 cycles of 10 % maximum strain to evaluate its sensing durability and examine any relative electrical resistance drift that could impede long-term usage. In addition, the nanocomposite sensor was held at a 10 % compressive strain for 2 h to observe its creep behavior. The electrical resistance of each sample was continuously recorded during all the above-mentioned piezoresistive tests.

2.2.8 Demonstration as Wearable Sensors

The microwave-cured nanocomposite sensors were tested for wearable sensor applications. New sensors were manufactured and both top and bottom surfaces of the sensors were sputter-coated with AuPd to ensure good contact with the electrodes made from copper tape. The microwave-cured nanocomposites with 1 wt% CNTs were attached to socks and gloves to test the sensor's viability for detecting pressures during common human movements. The electrical resistance was

recorded throughout each test with the Agilent multimeter mentioned above. A pressure sensor array was placed on the heel and sesamoid bone of the right foot by gluing one end of the copper tape attached to the sensors to a sock. The first test was performed on the sesamoid sensor by standing for 15 min continuously to compare the resistance drift from creep with the simulated creep test using the Instron machine. Next, both the heel and sesamoid sensors were tested under three human motions including sitting and standing, swaying/leaning left to right, and swaying front to back. Lastly, the sensors were attached to the fingertips of a latex glove to demonstrate the ability to detect the grabbing and squeezing motions of a human hand.

2.3 Results and Discussion

2.3.1 Microstructure of Fabricated Nanocomposites

Successful dispersion of CNTs within the PDMS elastomer was imperative to endow the best and most consistent mechanical, electrical, and piezoresistive properties to the nanocomposites. Mechanical properties can vary widely, and electrical properties can have an order of magnitude difference between well-dispersed and poorly-dispersed CNTs within a polymeric matrix [147]. Therefore, it was imperative to evaluate the quality of CNT dispersion within the PDMS matrix.

SEM images were used to qualify the CNT dispersion and remaining porosity within the nanocomposite sensors. The nanocomposite with the highest CNT loading was first studied to prove the high-quality dispersion because high CNT concentrations tend to result in poor dispersion and potentially agglomerates. Two representative SEM images identifying the CNT dispersion are shown in Figure 2.2(a) and Figure 2.2(b). The SEM images indicate high-quality CNT dispersion, and no agglomerates were observed during imaging.

Although degassing was performed during the manufacturing process, it was observed that resins with high CNT loadings did not fully release embedded air bubbles due to the increased viscosity endowed by CNTs on the prepolymer. Additional porosity may have been introduced while transferring the uncured nanocomposites into the molds before curing. Therefore, it was necessary to characterize the pores in nanocomposites with the lowest CNT loading of 1 wt% and the highest CNT loading of 2.5 wt%. A representative image of a small pore seen in the nanocomposites with 1 wt% CNT loadings is shown in Figure 2.2(c). Large pores within the nanocomposites with 2.5 wt% CNT are shown in Figure 2.2(d). Since large pores in the nanocomposite sensors can be significantly detrimental to consistent piezoresistive and mechanical performance, the nanocomposites with 1 wt% CNT were selected for piezoresistive characterization and wearable sensor applications.

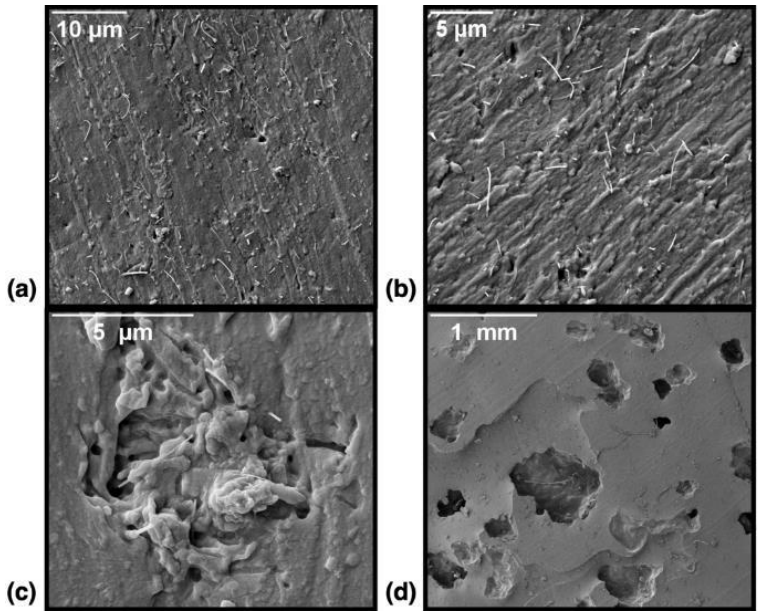

Figure 2.2: *SEM images of (a, b) CNT dispersion within m-PDMS/CNT with 2.5 wt% CNT loading, (c) a small pore found within the nanocomposite with 1 wt% CNT loading, and (d) larger pores found in the nanocomposite with 2.5 wt% CNT loading.*

2.3.2 Comparison of Electrical Properties

The percolation curves for both m-PDMS/CNT and t-PDMS/CNT were compared to investigate the hypothesis that rapid microwave-curing may reduce the CNT settlement effect and therefore result in higher electrical conductivity. The settlement effect within CNT doped polymers was a result of gravity and van der Waals forces attracting the nanoparticles together reforming agglomerates and reducing the overall quality of dispersion. It was observed that this effect decreased the overall conductivity of the nanocomposites due to fewer opportunities for conductive networks to form. A schematic of this nanoparticle settlement effect for low and high loadings of CNTs is shown in Figure 2.3.

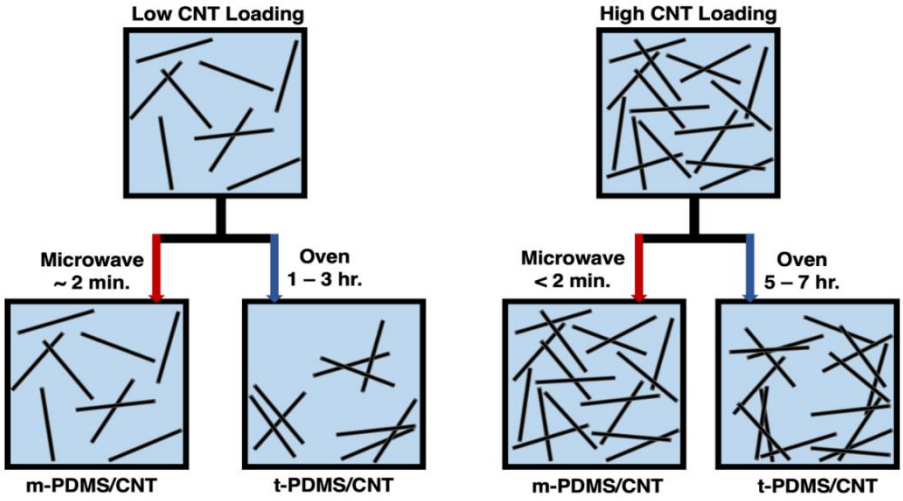

Figure 2.3: *Schematic of enhanced dispersion in m-PDMS/CNT due to reducing CNT settlement effect apparent in t-PDMS/CNT for low and high CNT loadings.*

Additionally, there have been reports that the microwave-curing of CNT doped epoxies likely leads to the alignment of these high aspect ratio nanoparticles in some direction [148]. The alignment of CNTs within the matrix material may provide a second mechanism to increase the

overall conductivity of the microwave-cured nanocomposites. Therefore, it was essential to investigate the conductivity improvements that could be obtained through microwave-curing the same batch of PDMS/CNT resin at different CNT loadings between 0.5 wt% and 2.5 wt%. Furthermore, it was important to measure the temperature of each sample during the microwave-curing process to aid future researchers in the microwave-curing of PDMS/CNT or materials with similar CNT content. The temperatures between pulses of each loading of prepared m-PDMS/CNT and the percolation curves for both m-PDMS/CNT and t-PDMS/CNT are shown in Figure 2.4.

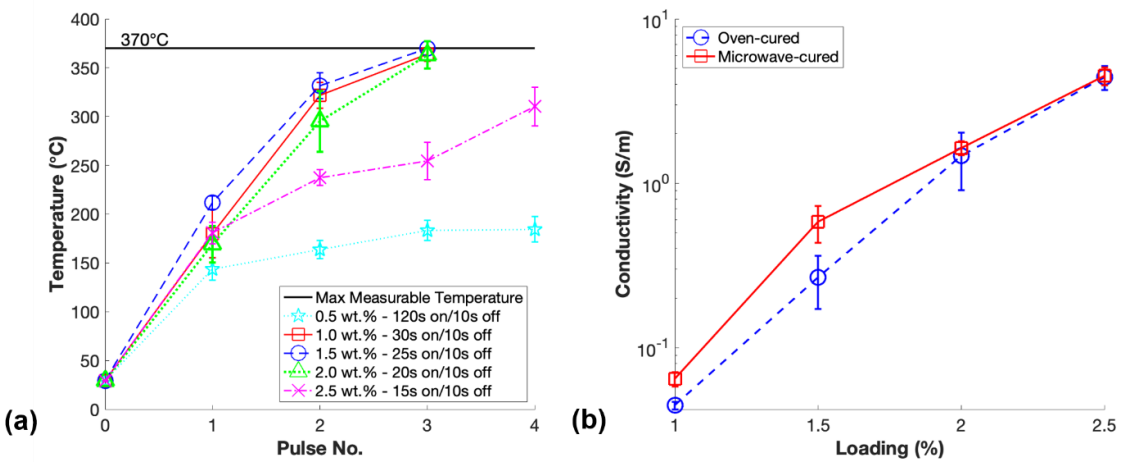

Figure 2.4: *(a) Average temperature measurements between pulses of m-PDMS/CNT for each CNT loading prepared and (b) conductivity averages for each loading of m-PDMS/CNT and t-PDMS/CNT.*

The maximum measurable temperature was included in Figure 2.4(a) as this was the maximum measurable temperature of the thermal imager, and during the last step of curing 1.5 wt% m-PDMS/CNT, the temperature reached slightly above this threshold. Progressively shorter pulsing times of 20 % microwave power were chosen for higher loading material to prevent the thermal shock expansion of the material from ripping the samples apart, which was observed if the

temperature rose too quickly. Increments of 5 s were chosen to make the pulsing cycles simple to consistently achieve manually pulsing the microwave at the correct time. The nonconductive 0.5 wt% PDMS/CNT required a significantly longer curing time of 4 pulses of 120 s showing the significant impact semiconductivity has on the microwave coupling and rapid heating of the material. Although 2.5 wt% m-PDMS/CNT had the highest conductivity due to having the highest loading of materials tested, the rate of temperature change was the slowest of the conductive resins due to the relatively short time of 15 s used for each microwave pulse.

The percolation curves for both m-PDMS/CNT and t-PDMS/CNT shown in Figure 2.4(b) indicated that for each conductive loading, the microwave-cured samples had a higher conductivity than the thermally-cured samples. The average percentage increase of conductivity for m-PDMS/CNT over t-PDMS/CNT for loadings 1 wt%, 1.5 wt%, 2 wt%, and 2.5 wt% were 44.8 %, 118 %, 11.7 %, and 1.8 % respectively. At higher loadings, 2 wt% and 2.5 wt%, the conductive networks were more saturated, thus the CNT settlement effect on the decrease of conductivity was less impactful, illustrated by the schematic shown in Figure 2.3. Additionally, any microwave-induced CNT alignment effects that generated an increase in conductivity were also likely less impactful in nanocomposites with higher loadings of CNTs. Surprisingly, the increase of conductivity due to microwave-curing in this study was significantly more dramatic for the 1.5 wt% PDMS/CNT. This indicated that at this CNT loading in the middle of the percolation curve there were a larger number of conductive networks that were either newly formed or beneficially aligned due to the microwave-curing procedure. It may be important to note that the trend of the relative rate of temperature increase for each loading during microwave-curing matched the trend of the percentage increase of conductivity from their thermally-cured counterparts. These findings

and observations proved useful in future studies in this work to optimize the microwave settings to produce the lowest loading samples at the highest conductivity.

Another notable finding in this study was the difference in the contact resistance of these conductive elastomeric nanocomposites. Contact resistance is a commonly unreported issue with these materials that is usually overcome in the field with the use of silver paste, or in our case, silver epoxy and copper tape. Results of the measured contact resistance of the m-PDMS/CNT and t-PDMS/CNT samples are shown in Figure 2.5, along with SEM images of the surfaces of the samples that were in contact with their respective molds during fabrication.

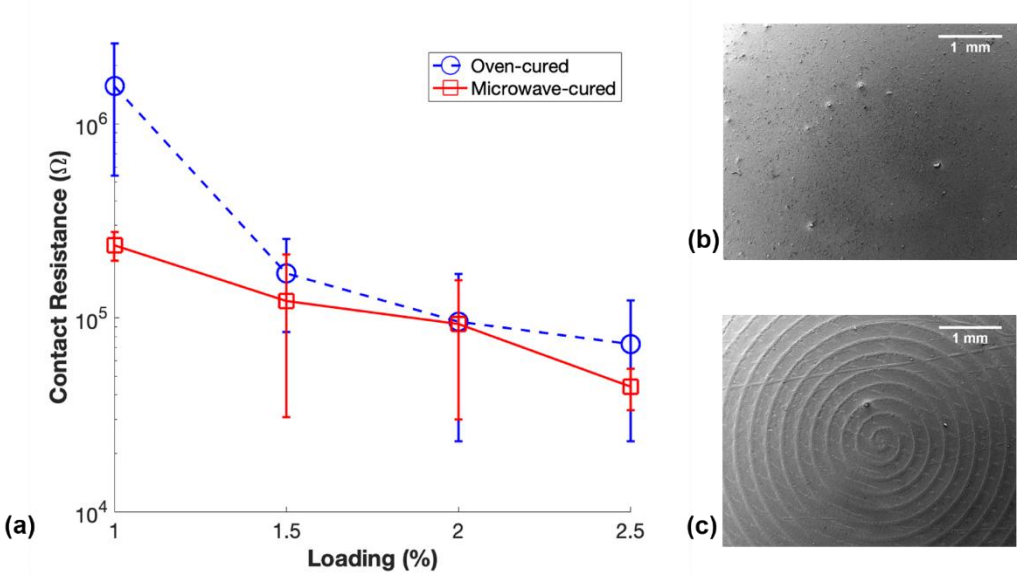

Figure 2.5: *(a) Contact resistance of m-PDMS/CNT and t-PDMS/CNT for each conductive loading, (b) SEM image of m-PDMS/CNT surface cured in contact with glass mold, and (c) SEM image of t-PDMS/CNT cured in contact with aluminum mold.*

The general trend in Figure 2.5(a) shows that m-PDMS/CNT samples had a lower average contact resistance than t-PDMS/CNT, likely due to surface effects of the molds and potentially CNT settlement. The error bars are large due to a relatively inconsistent method used to cut the top

expanded surface of the samples by hand with a razor blade. However, the average contact resistances for 1 wt%, 1.5 wt%, 2 wt%, and 2.5 wt% m-PDMS/CNT were 84.9 %, 28.4 %, 2.8 %, and 39.8 % less respectively than the average contact resistance of t-PDMS/CNT. This can most likely be explained by the surface effects on the samples introduced by the glass and aluminum molds. The SEM image displayed in Figure 2.5(b) shows the smooth surface of 1 wt% m-PDMS/CNT advantageous for smooth consistent contact with the copper plate electrodes. In contrast, Figure 2.5(c) shows an SEM image of the spiral-shaped uneven surface of 1 wt% t-PDMS/CNT because of the toolpath of the CNC milling machine used to create the aluminum mold. These differences in surface topography of m-PDMS/CNT and t-PDMS/CNT may have led to the differences in average contact resistance when loaded between the two electrodes.

2.3.3 Characterization of Porosity and Stiffness

Any trace amount of solvent or air bubbles left in the nanocomposite prepolymer can expand dramatically during the microwave-curing procedure and cause embedded pores in the fully cured nanocomposite sensors. Although researchers have shown that well-distributed pores within conductive nanocomposites can improve the piezoresistive sensitivity, the mechanical properties of the cured materials can be reduced [5, 149]. In this paper, the porosity of cured nanocomposites was calculated using the density method. The volume of each sample was determined by measuring each cylindrical sensor with a caliper and micrometer to find the diameter and height of each nanocomposite sensor. The density of each sensor was calculated with these measurements and the resulting porosity was determined with Equation (2.1)

$$\text{Porosity} = \left(1 - \frac{\rho_m}{\rho_s}\right) \times 100\% \tag{2.1}$$

where ρ_m is the calculated density of the manufactured nanocomposite and ρ_s is the calculated density of the completely solid nanocomposite. The average porosities of the microwave-cured and thermally-cured nanocomposites are shown in Figure 2.6(a).

The curing process can also affect the mechanical properties of polymers. Microwave irradiation of CNT-based nanocomposites has proven to provide potentially improved or often similar mechanical properties in comparison to the thermally-cured counterparts [150]. To the best of the authors' knowledge, the effects of microwave irradiation on the mechanical properties of CNT-based elastomeric nanocomposites have not been well-reported in the literature. Therefore, it was still necessary to compare the average compressive modulus of the microwave-cured and thermally-cured nanocomposites in this paper. The compressive modulus of each sample was taken as the slope of the linear section of the stress-strain curve during the compressive mechanical tests. The results of the average compressive moduli of the nanocomposite sensors at each CNT loading are shown in Figure 2.6(b).

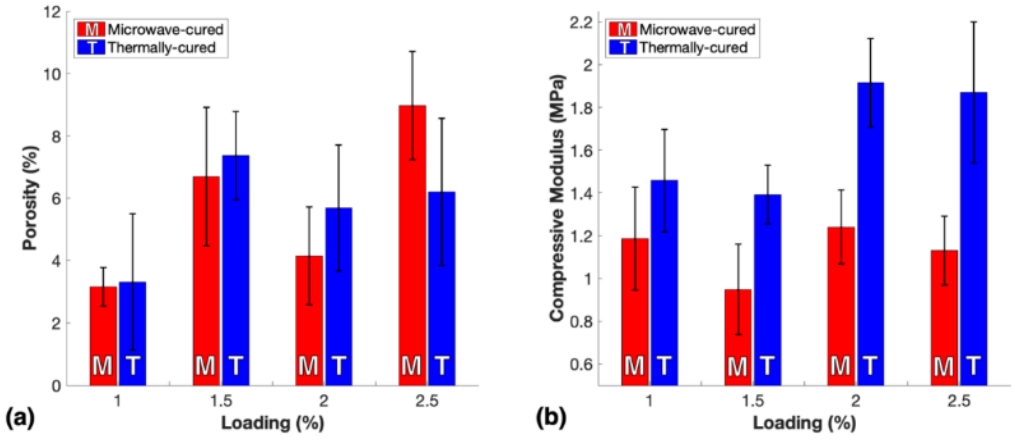

Figure 2.6: *Comparison of 1 wt%, 1.5 wt%, 2 wt%, and 2.5 wt% loadings of m-PDMS/CNT and t-PDMS/CNT including the (a) average porosity and (b) the average compressive moduli of the sensors.*

The porosity significantly affected the mechanical properties of the elastomeric nanocomposites. During compression, pores collapsed, and the void space was filled due to deformations within the material. Thus, the porosity increased the compressibility of the sensors which resulted in a lower compressive modulus than the completely solid material. Increased CNT content would typically result in a higher modulus of elastomeric nanocomposites, however, the comparison of the average porosities between each loading explained any discrepancies with this trend as the increased porosity reduced the stiffness more significantly than the reinforcing nanofiller increased the stiffness. Since the porosities between the microwave-cured and thermally-cured nanocomposites of the same CNT loadings were comparable, it is reasonable to consider the differences in moduli between the two curing methods for each CNT loading.

The most notable discovery from this study was the substantially higher compressive modulus measured from the thermally-cured nanocomposites over the microwave-cured ones. The average decreases of compressive modulus for the microwave-cured nanocomposites in comparison to the thermally-cured nanocomposites with CNT loadings of 1 wt%, 1.5 wt%, 2 wt%, and 2.5 wt% were 18.7 %, 31.9 %, 35.2 %, and 39.6 %, respectively. This may be attributed to rapid microwave-curing likely leading to lower crosslinking density in the cured thermoset sample compared to thermally-cured due to a significant reduction in the curing time. Notably, it was observed that microwave-curing led to the hardening of the thermoset elastomer in the internal core before fully hardening the outer surfaces of the material during the quick curing time of 2 min or less. In contrast, thermal-curing in an aluminum mold required substantially more time (1 h - 7 h) to cure fully. During curing in an oven, heat propagated from the outside inward until the material reached near the oven temperature and slowly cured. Interestingly, nanocomposites with higher CNT loadings required significantly more time in the oven to cure. However, higher CNT loadings

required less time to microwave-cure due to CNTs producing substantial heat under microwave irradiation. The differences in the curing mechanisms, the total curing time, and potentially the differences in the degree of cure likely influenced the elastic moduli of the cured nanocomposites. Therefore, the microwave-curing method produced nanocomposites with relatively low compressive modulus due to the matrix material experiencing higher temperatures for a significantly shorter time than the nanocomposites cured in an oven.

2.3.4 Comparison of Piezoresistive Capabilities

Microwave-curing PDMS/CNT offered a significant time savings of at least 96 % in the curing process of cylindrical piezoresistive sensors in comparison to traditional thermal-curing. These tremendous time savings would lead to dramatic cost savings during the mass manufacturing of these nanocomposites. It was necessary to compare the piezoresistive response of the microwave-cured and thermally-cured nanocomposites to determine if microwave-curing could adequately replace traditional thermal-curing of these nanocomposite sensors. The nanocomposites with 1 wt% CNT loading were selected for piezoresistive comparison. The microwave-cured and thermally-cured nanocomposites with 1 wt% CNTs had the two lowest average porosities that were also the most comparable between curing methods than any other CNT loading tested. Therefore, piezoresistive sensors with 1 wt% CNTs were chosen for the compression sensing comparison. Typically, the dispersion quality and alignment of CNTs within nanocomposites affect the piezoresistive response and the sensitivity of these sensors. The results of the piezoresistive sensing comparison for varying strains between 3 % and 20 % for the microwave-cured and thermally-cured nanocomposites with 1 wt% CNTs are shown in Figure 2.7. The relative change in resistance is calculated using Equation (2.2)

$$\frac{\Delta R}{R_0}(\%) = \frac{R - R_0}{R_0} \times 100\,\% \tag{2.2}$$

where ΔR is the change in resistance, R is the immediate resistance, and R_0 is the initial resistance. The relative resistance change can be used to determine the sensitivity of the sensor or gauge factor using Equation (2.3) where $\Delta\varepsilon$ is the applied strain.

$$\text{Gauge Factor} = \frac{R - R_0}{R_0 \cdot (\varepsilon - \varepsilon_0)} = \frac{\Delta R}{R_0 \cdot \Delta\varepsilon} \tag{2.3}$$

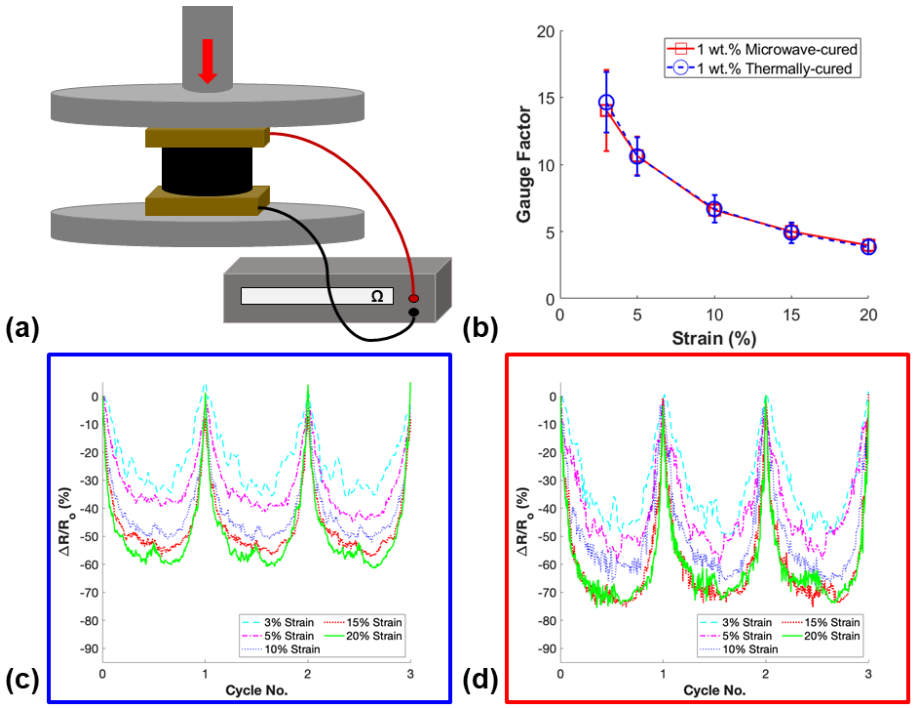

Figure 2.7: *(a) Schematic of the piezoresistive test setup to measure the resistance change of the sensor during compressive loading, (b) average gauge factors of m-PDMS/CNT and t-PDMS/CNT with 1 wt% CNTs through 3 %, 5 %, 10 %, 15 %, and 20 % strains, representative plots of the relative resistance change for each applied strain on (c) t-PDMS/CNT and (d) m-PDMS/CNT with a 1 wt% CNT loading.*

The microwave-cured nanocomposites demonstrated equivalent piezoresistive sensitivity in comparison to the thermally-cured samples. The results displayed in Figure 2.7(b) show remarkably similar average gauge factors between the two curing methods for sensors with 1 wt% CNT loading. The average gauge factors for 3 %, 5 %, 10 %, 15 %, and 20 % strain for the microwave-cured nanocomposites with 1 wt% CNTs were 14.0, 10.6, 6.6, 5.0, and 4.0, respectively; and the thermally-cured sensors had average gauge factors of 14.6, 10.6, 6.7, 4.9, and 3.8 for the same strain range. Both sensors exhibited negative piezoresistive behavior, thus the relative resistance decreased during the initial compression due to CNTs generally being brought closer together forming more conductive networks, geometric changes of the samples, and likely changes in contact resistance with the copper electrodes during compression. This relative resistance change was followed by some amount of hysteresis that proved to be minimal and relatively inconsistent at maximum compression. Overall, these studies proved that microwave-curing the CNT-based nanocomposites produced piezoresistive sensors with similar piezoresistive sensitivity compared to thermal-curing. These findings, in conjunction with the significantly reduced curing times, exhibited the potential for microwave-curing to replace traditional thermal-curing when manufacturing elastomeric CNT-based piezoresistive sensors.

2.3.5 Optimization of Microwave Parameters for Enhanced Conductivity

To isolate the microwave-curing parameters and explore their impact on the conductivity of m-PDMS/CNT, the lowest conductive loading of material (1 wt%) was chosen for further microwave-curing investigation. The first investigation performed was the pulse study to examine whether pulsing the microwave on and off had an impact on the conductivity of the fabricated nanocomposites. Each sample was cured in 2 min or less to effectively negate settlement effects and isolate the microwave-induced CNT alignment effects to observe their impact on the

conductivity of the samples. The temperature and conductivity results for the pulse study varying the number of 50 % power microwave pulses to cure 1 wt% PDMS/CNT are shown in Figure 2.8.

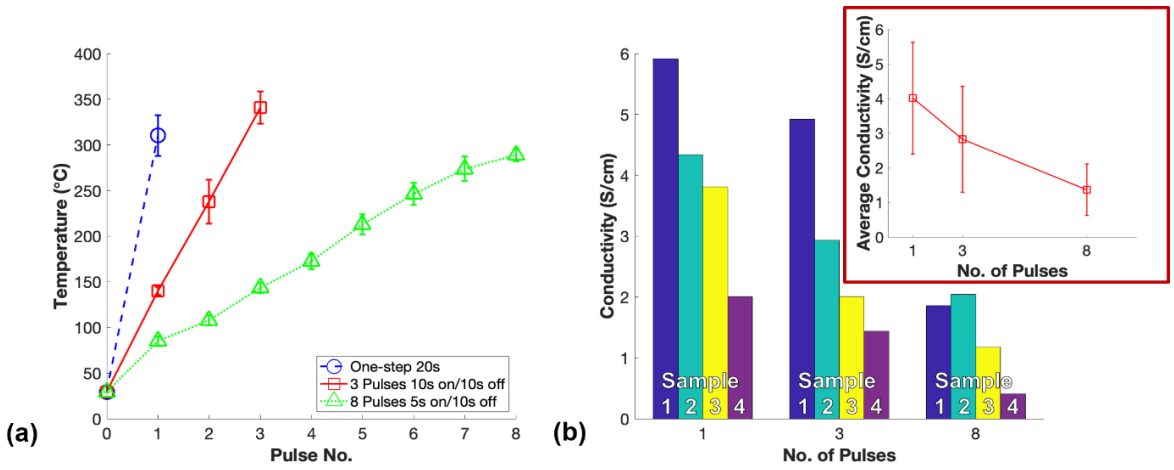

Figure 2.8: *Pulse study - (a) Average temperature measurements between pulses of 50 % microwave power used to cure 1 wt% PDMS/CNT and (b) conductivity of each set of samples for the varying number of pulses used to fabricate m-PDMS/CNT.*

As expected, the temperatures of the samples during microwave-curing rose quicker for the samples cured with fewer pulses of longer periods of continuous microwave irradiation exposure. In this study, one-step microwave-curing of PDMS/CNT nanocomposites produced the highest average conductivity followed by 3 pulses and lastly 8 pulses as shown in Figure 2.8(b). The faster increase in temperature during the microwave-curing process corresponded with the higher average conductivity of the samples. The increased overall time of the microwave pulsed off during the curing process allowed polymerization to continue during this time due to substantial heat remaining within the resin. The resin partially cured while not being exposed to microwave irradiation and likely increased the viscosity of the matrix resin which in turn resisted the alignment mechanism advantageous for enhanced conductivity when exposed to microwaves again.

Therefore, the CNT alignment effects induced by microwave exposure were highest for one-step microwave-curing resulting in the highest average conductivity. Notably, the conductivity of each fabricated sample shown in Figure 2.8(b) exhibited the influence of 15 min of settlement effect within the PDMS/CNT prepolymer that occurred between the fabrication of each set of samples. This settlement effect between various sets of samples explained the large error bars seen for the average conductivities, however, the trend for each set of samples was consistent which indicated the significance of one-step microwave-curing to fabricate the highest conductivity nanocomposite.

The power study was performed using one-step microwave irradiation to isolate the microwave power setting of the unmodified commercial microwave as a parameter that could impact the conductivity of m-PDMS/CNT. While the CNT alignment effects generated by microwave irradiation have not been well understood, it is important to investigate all possibilities that may impact this alignment. In this work, the potential CNT alignment was measured as the conductivity of the fabricated nanocomposites. Therefore, the impact of 20 %, 50 %, and 80 % microwave power during one-step microwave-curing of 1 wt% PDMS/CNT prepolymer was investigated and the results are shown in Figure 2.9.

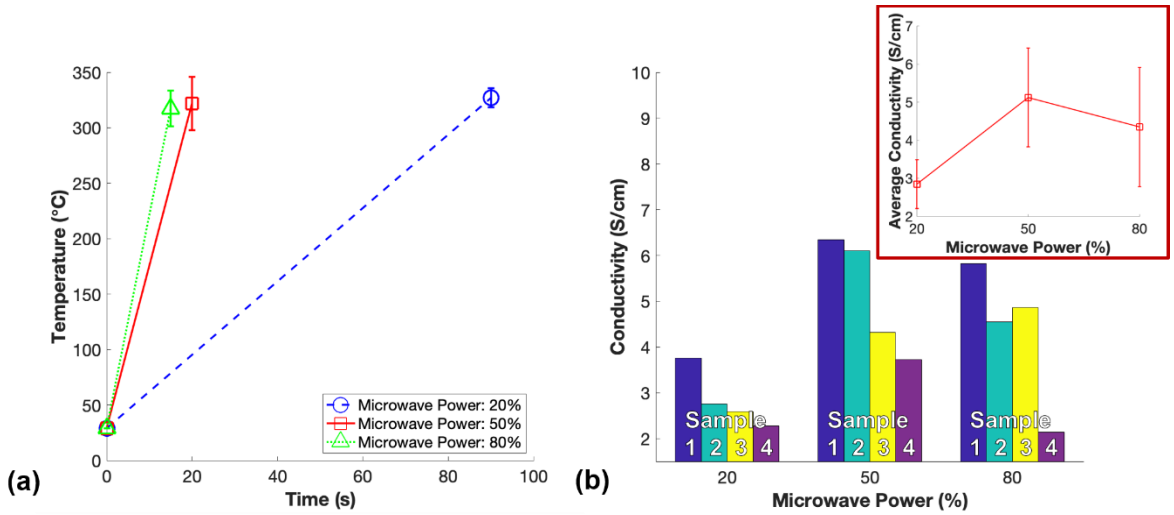

Figure 2.9: *Power study - (a) average temperature measurements after microwave-curing nanocomposites with 1 wt% CNT for one-step at variable microwave powers and (b) the conductivities of each sample cured with varying microwave powers used to fabricate m-PDMS/CNT.*

Notably, an inverter microwave was used in this study that supplies constant microwave power throughout even at lower powers, where a non-inverter microwave would not. At 20 % microwave power, the temperature of 1 wt% PDMS/CNT increased significantly slower than 50 % and 80 % power. The 20 % microwave power may have simply not been sufficiently powerful enough to induce the CNT alignment effect, which could explain why 20 % microwave power cured samples resulted in the lowest electrical conductivity on average. Surprisingly, m-PDMS/CNT cured at 80 % power had a slightly lower average conductivity than the samples cured at 50 % power. This could be due to an enhanced rate of heating and polymerization slowing the CNT alignment process through thixotropic effects or rapid curing locking the orientation of the CNTs in place before fully aligning. On the contrary, polymerization may have not fully propagated through the sample by the time the temperature had built up to above 300 °C, where the microwave exposure was stopped to prevent the samples from ripping apart due to intense thermal shock. Thus, the sample may have finished curing after microwave exposure ceased and the 5 s shorter time exposed

to microwave irradiation as a resin would result in less CNT alignment and a slightly lower average conductivity. However, the average conductivity of m-PDMS/CNT cured at 50 % power and 80 % were reasonably close, so they both may have reached near maximum conductivity enhancement for microwave-curing 1 wt% PDMS/CNT. Regardless, one-step microwave irradiation at 50 % power was found to be the optimal parameters to fabricate 1 wt% m-PDMS/CNT with the highest conductivity.

2.3.6 Optimized Microwave-curing Conductivity Improvement

After optimizing the microwave-curing parameters to obtain the highest conductivity of 1 wt% m-PDMS/CNT, it was imperative to compare the optimal microwave-cured samples with thermally-cured samples to quantify the improvements made through the optimization process. For the final comparison, one-step 50 % power microwave irradiation was used to fabricate 1 wt% m-PDMS/CNT while simultaneously fabricating 1 wt% t-PDMS/CNT in an oven at 150 °C. These optimized microwave settings were believed to improve the alignment of CNTs within the nanocomposite further increasing the conductivity of the nanocomposite as shown in Figure 2.10(a). The conductivity of each sample produced from both curing methods and the results of the temperatures that the PDMS/CNT encountered from microwave-curing are shown in Figure 2.10(b) and Figure 2.10(c), respectively.

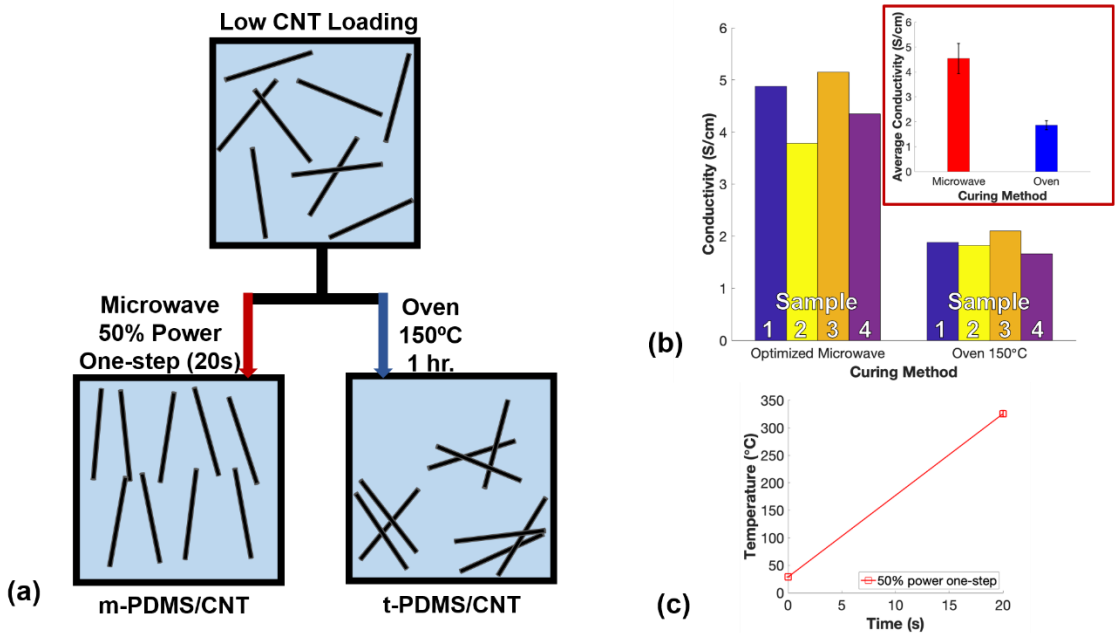

Figure 2.10: *Optimized comparison - (a) Schematic showing improved CNT dispersion and alignment for nanocomposites cured with optimal microwave parameters, (b) conductivity of each set of samples for optimal m-PDMS/CNT and t-PDMS/CNT, and (c) average temperature measurements after microwave-curing 1 wt% PDMS/CNT for one-step at 50 % power.*

The microwave temperature results in this study shown in Figure 2.10(c) matched the temperature results shown in Figure 2.8(a) and Figure 2.9(a) for the same microwave parameters and the same 1 wt% CNT loading in the cured nanocomposites. These results confirmed that the relatively consistent microwave-curing temperatures were produced between batches of 1 wt% m-PDMS/CNT. The average conductivities of the optimal m-PDMS/CNT and t-PDMS/CNT were 4.54 S/cm and 1.87 S/cm, respectively, indicating a 142.8 % improvement of conductivity for the microwave-cured nanocomposites using the optimized microwave parameters. This was a huge improvement from the initial 44.8 % conductivity enhancement demonstrated in the first comparison using 20 % microwave power and 3 pulses of 30 s. The findings in this study demonstrated the impact of optimizing commercial microwave settings to achieve the largest conductivity enhancements for CNT-based nanocomposites fabricated via microwave-curing.

2.3.7 Piezoresistive Sensing Characterization

After finding that the microwave-cured nanocomposites with 1 wt% CNTs were the best performing piezoresistive sensors (Figure A.1, Appendix A), it was critical to fully characterize the piezoresistive behavior of the sensor. The first piezoresistive test to characterize the sensor was a strain rate test. A constant maximum strain of 10 % was applied on the nanocomposite while varying the strain rate (5 %/min, 10 %/min, 25 %/min, 50 %/min, 100 %/min, 200 %/min) to determine if the piezoresistive response of the sensor was dependent on strain rate. Additionally, a durability test was performed on the sensor where 800 compressive loading cycles of 10 % maximum strain were applied to determine if the sensor had significant resistance drift, which is commonly reported in piezoresistive sensors. The results of these two tests are shown in Figure 2.11.

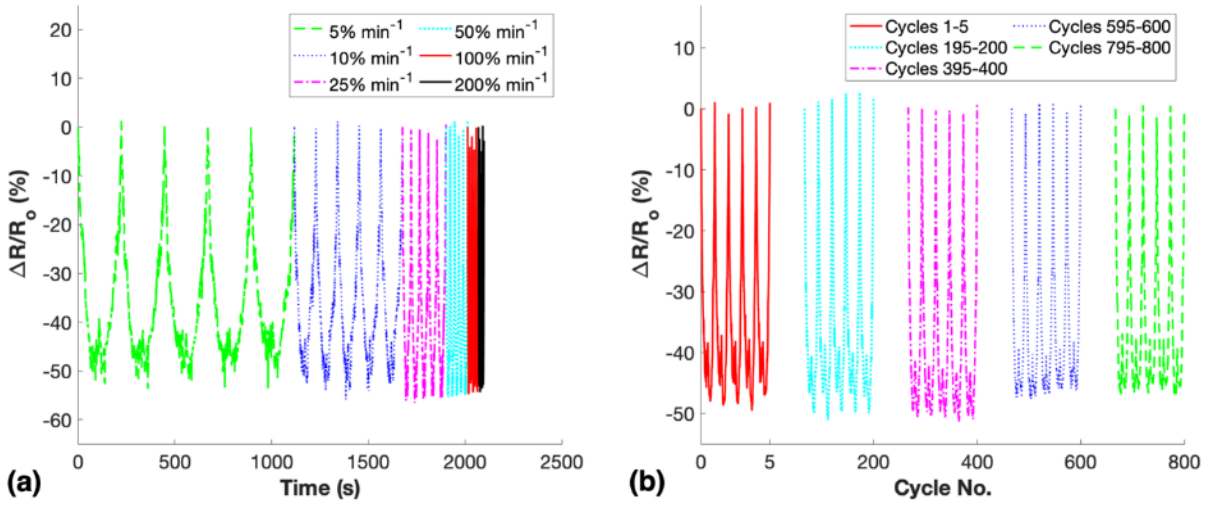

Figure 2.11: *Representative plots of the relative resistance change of 1 wt% m-PDMS/CNT sample up to 10 % maximum compressive strain (a) at various strain rates and (b) for 800 cycles.*

The sensor showed little to almost no dependency on strain rate, as the relative resistance change, shown in Figure 2.11(a), did not fluctuate significantly. The largest percentage difference of the average relative resistance change between strain rates was about 8.6 % which indicated a consistent piezoresistive response relatively independent of the rate at which deformation was applied. Notably, the plot in Figure 2.11(a) shows relatively large discrepancies of the maximum and minimum resistance measurements for higher strain rates. This can be explained by the small sampling frequency of 3 Hz used for the test. The durability test, shown in Figure 2.11(b), indicated some small drift of the relative resistance change that is unsurprising for the nature of the nanocomposite material. During constant cyclic loading, the elastomeric matrix material likely warmed up due to intermolecular friction as energy was applied to the material which may have influenced the resistance drift displayed. During the first 200 cycles, the average relative resistance changes of the representative cycles in Figure 2.11(b) increased by about 6 %. By the end of the test, the average relative resistance change had progressively decreased by about 10 %. This drift was moderately noticeable and important to consider during the long-term use of the sensor.

The creep behavior of the piezoresistive sensor was characterized as it is an important characteristic to consider for applications where the sensor is held at a constant strain. The results of the simulated creep test are shown in Figure 2.12. During the creep test, the rate of decrease of the recorded relative stress within the material correlated well to the rate of decrease of the relative resistance change in the sensor. This result suggested that the reorganization of the conductive networks during the experiment may be dependent on the creep behavior of the matrix material. This creep behavior could be explained by the viscoelastic material settling into the newly established boundary conditions until equilibrium within the material was reached. In the simulated test, the relative resistance of the sensor dropped by about 25 % in only about 15 min

where the measurement remained relatively stable. The rate of decrease of the relative stress in the sample had decreased significantly after 30 min, however, the relative stress continued to decrease slightly until the end of the 2 h test. These results were not surprising considering the nature of the nanocomposite material and were important to quantify in a simulated test to compare with the piezoresistive creep behavior apparent in an application.

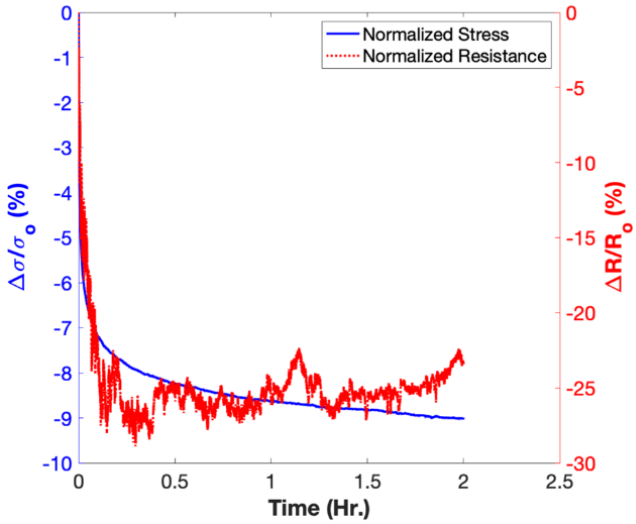

Figure 2.12: *Stress and piezoresistive creep behavior of 1 wt% m-PDMS/CNT loaded to 10 % compressive strain and held for 2 h.*

2.3.8 Wearable Sensor Applications

Potential applications for this flexible piezoresistive sensor include soft robotics, prosthetics, and human motion detection. In this study, human motion detection was explored as possible applications for these piezoresistive sensors, whereby the sensors were attached to a sock and glove. For the first application demonstrated, two sensor locations were chosen on the sock to align with the user's heel and sesamoid bone on their right foot as shown in Figure 2.14(a). First, the simulated creep test was compared to an application that would apply a relatively constant strain

to the sensor. In this study, the sensor was attached to the sesamoid bone of the foot and the user remained standing for 15 min to compare the piezoresistive creep response with the simulated test. The results of the comparison of the simulated creep test with the relevant application are shown in Figure 2.13. The relative change in resistance due to creep aligned very well for the simulated test in comparison to the sesamoid sensor in the standing application. This result confirmed that the resistance decreases during creep conditions in an application matched closely with the creep behavior demonstrated in the simulated test.

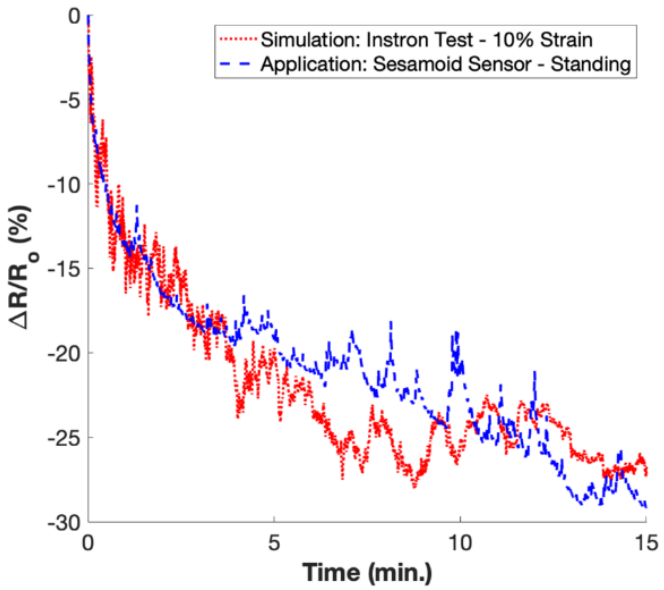

Figure 2.13: *Comparison of simulation and application of the piezoresistive creep behavior of a 1 wt% m-PDMS/CNT sample.*

For the first human motion detection study, both sensors were attached to the sock and put on the right foot of the user, as shown in Figure 2.14(b). Only one sensor location on the right foot was tested at a time while the user went through three motion cycles which included sitting and standing, swaying left to right, and swaying front to back, as shown in Figure 2.14(c). The relative

resistance changes of the sensors during these tests are shown in Figure 2.14(d) – Figure 2.14(f). Notably, the sesamoid sensor experienced less resistance change than the heel sensor due to the stiffness of the flesh likely being lower at that location. This application demonstrated the sensor's ability to detect human body motion and offers the potential to use as a sensor array on both feet to detect more complex motions including the movement of a user's center of gravity, walking, running, jumping, etc.

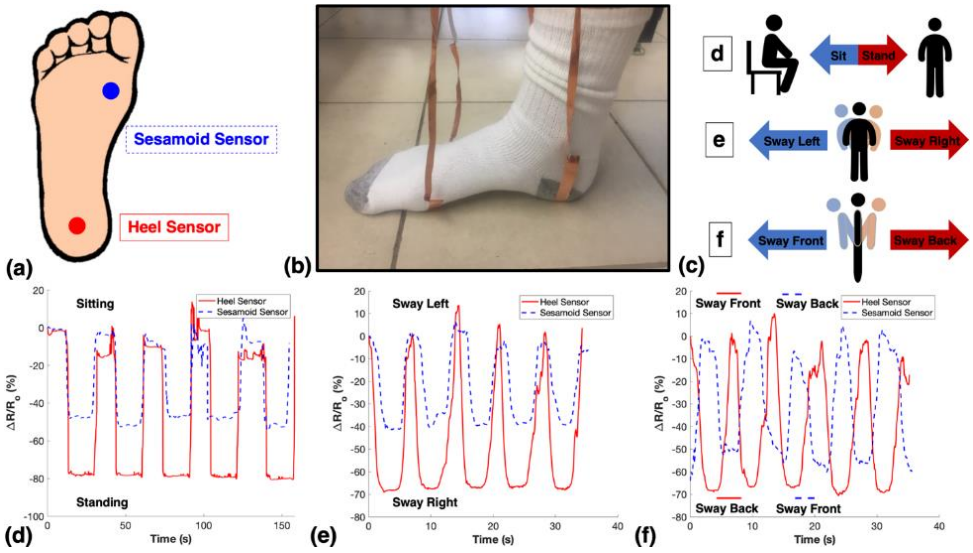

Figure 2.14: *Foot sensors - (a) Sensor locations for the 1 wt% m-PDMS/CNT samples on the ball of the foot (sesamoid bone) and the heel, (b) picture of the experimental setup, (c) schematic illustrating the experimental procedures, and relative resistance changes of both sensors during (d) sitting and standing, (e) swaying left to right, and (f) swaying front to back.*

Four sensor locations were chosen on the tips of each finger, excluding the thumb, to detect the cyclic grabbing and squeezing of an object, as shown in Figure 2.15(a). One sensor was tested at a time while the user grabbed and squeezed a glass bottle repeatedly, as shown in Figure 2.15(b). The results of the relative resistance change during the tests for each finger are shown in Figure 2.15(c) – Figure 2.15(f). The sensors detected small differences between the various forces applied

from each finger, which indicated a potential for the piezoresistive sensors to be used as sensory feedback sensors on prosthetic devices.

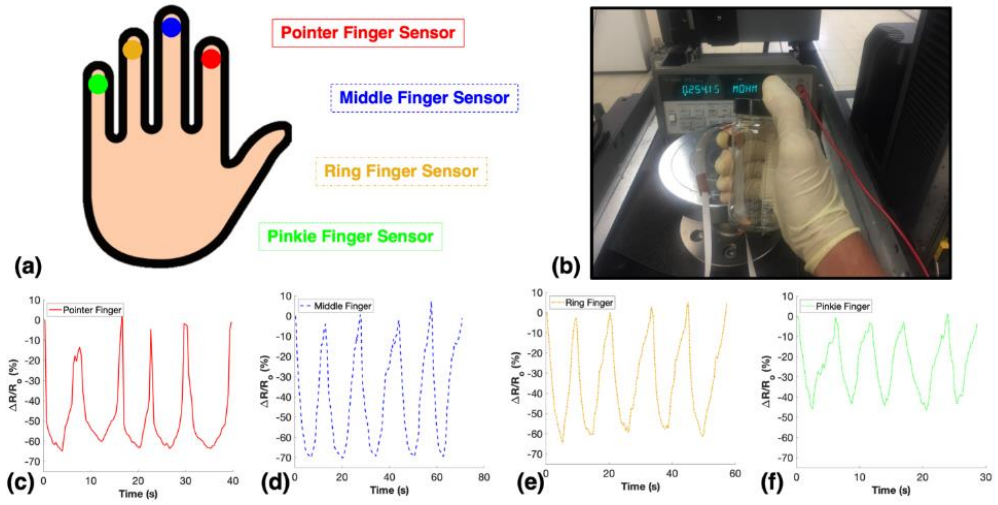

Figure 2.15: *Fingertip sensors - (a) Sensor locations for the 1 wt% m-PDMS/CNT samples on the fingertips of the pointer, middle, ring, and pinkie fingers, (b) a picture of the experimental setup, and the relative resistance change of the sensor when placed on the (c) pointer finger, (d) middle finger, (e) ring finger, and (f) pinkie finger.*

2.4 Conclusions

In this chapter, CNT-based PDMS nanocomposites were prepared via microwave-curing and traditional thermal-curing in an oven for electrical, mechanical, and piezoresistive comparison. Microwave-curing was found to enhance the electrical conductivity due to faster curing times, improved dispersion, and potentially beneficial CNT alignment. The moduli of microwave-cured nanocomposites were found to be significantly lower than thermally-cured counterparts and the piezoresistive sensitivity in compression was unaffected by the curing method. Therefore, microwave-curing was determined to have the potential to replace thermal-curing of CNT doped elastomeric piezoresistive sensors, with the advantages of significantly reducing the curing time

to as little as 15 s and enhancing the compressibility. The piezoresistive sensors fabricated in this study were highly sensitive and detected a minimum of 3 % strain. The piezoresistive response of the microwave-cured nanocomposites with 1 wt% CNTs under various compressive strains, different strain rates, 800 cycles of loading, and viscoelastic creep conditions were characterized. Two applications detecting common human movements were demonstrated by attaching the sensors to the foot and fingertips of a user. The microwave-curing parameters, including the number of pulses and microwave power, were optimized to produce the highest conductivity samples of the lowest conductive CNT loading of 1 wt%. The optimal microwave settings to enhance the electrical conductivity were found to be one-step exposure at 50 % microwave power. Experimental results demonstrated that microwave-curing nanocomposites with 1 wt% CNT loading were able to increase the overall electrical conductivity of the nanocomposite by 142.8 % over thermally-cured samples due to reducing the settlement effect of the nanoparticles and likely improving CNT alignment. Overall, the microwave-curing technique of these nanocomposite sensors led to tremendous time-savings during curing, no change in piezoresistive sensing performance, significantly enhanced conductivity, and reduced compressive modulus. Therefore, microwave-curing should be considered as a viable manufacturing technique in the field of carbonaceous nanocomposite piezoresistive sensors.

CHAPTER 3: EMBEDDED 3D PRINTING STRAIN SENSORS

3.1 Introduction

3.1.1 Motivation

While investigating the compressive piezoresistive behavior and sensing applications of bulk PDMS/CNT nanocomposites in the previous study, tensile strain sensing for large human motion applications piqued my interest. One can imagine the impact strain sensing wearables will have on the way we communicate with our electronic devices. One premier example includes the potential application of strain sensors on a full-body suit or clothing articles to monitor the angles of each joint to effectively duplicate the user's movements into the digital world/virtual reality. To measure these body angles most accurately, sensors may be attached to the skin of the user, however, safety is of paramount importance when dealing with nanocomposites. Therefore, to avoid the potential of nanoparticle detachment and potentially harming the user, the e-3DP technique was used in this study to fabricate and tailor strain sensors for human motion detection. The studies in this chapter have been published in Composites Part B: Engineering [151].

3.1.2 Background

In this study, an Ecoflex/CNT nanocomposite ink was developed for the e-3DP of a highly flexible skin-attachable strain sensor. The objective of the study was to optimize the fabrication parameters, including the loading of CNTs, the curing temperature, and the DIW nozzle size to produce the most sensitive strain sensor. The most sensitive embedded sensor fabricated in this study was fully characterized to investigate its functionality as a piezoresistive skin-attachable sensor. The sensor

was attached to several human joints to demonstrate the ability of the wearable sensor to detect normal bending movements. Lastly, the freeform design and fabrication capabilities of the e-3DP process were demonstrated. This study provides a relevant guideline for improving the sensitivity of a CNT-based nanocomposite strain sensor fabricated by the e-3DP process.

3.2 Experimental Methods

3.2.1 Materials

Ecoflex 00-30, Slo-Jo Platinum Silicone Cure Retarder, Silicone Thinner, and Thivex were purchased from Smooth-On. Multi-walled CNTs with an average diameter between 50 – 90 nm with aspect ratios > 100 were purchased from Sigma-Aldrich. Isopropanol alcohol (99 %) was obtained from Sigma-Aldrich. Unless otherwise noted, all materials were used as received and as the manufacturer recommended.

3.2.2 Nanocomposite Ink Preparation

Nanocomposite resin containing various loadings of multi-walled CNTs was mixed and dispersed via a probe tip sonication method (Figure A.2, Appendix A). Multi-walled CNTs were mixed in 40 mL of isopropanol with a magnetic stir bar at 500 rpm for 5 min. The suspension was ultrasonicated with a Sonics Vibra-Cell VCX 750-watt ultrasonic homogenizer with a CV33 probe for 10 min at a 28 % amplitude, pulsing on for 5 s and off for 2 s. The Ecoflex 00-30 Part A was added to 20 mL of isopropanol and mixed at 500 rpm for 5 min. Next, the CNT suspension was added to the Ecoflex and alcohol solution and mixed at 500 rpm for 2 min. The mixture was sonicated for 30 min, then mixed at 500 rpm overnight on an 85 °C hot plate. The resulting nanocomposite resin was placed in a vacuum oven at 85 °C overnight. The nanocomposite resin

was mixed with Ecoflex Part B and loaded into a syringe and mixed for 20 min and defoamed for 15 min in a planetary centrifugal mixer (Thinky AR100).

3.2.3 Nanocomposite Conductivity

Cylindrical nanocomposites were cured at 90 °C in an aluminum mold (diameter = 11 mm; height = 9 mm). The resistance was measured with a Hioki RM3545-02 Resistance Meter using the two-probe method to determine the average conductivity at each CNT loading.

3.2.4 Embedded Printing Process

A commercial 3D printer was modified to function as a pneumatic DIW printing system with a pressure regulator maintaining constant extrusion pressure during printing. The e-3DP method developed by Muth et al. was used for the embedded printing procedure [48]. The method requires the bath resin to be the same material, but with two layers of modified rheology resin as shown in the schematic illustration in Figure 3.1(a). The bottom layer (reservoir) must be a high viscosity resin to support the higher density ink, and the top layer (filler) a low viscosity resin to fill the wake behind the needle as it moves through the reservoir that often leads to inaccurate deposition. The reservoir was prepared by mixing the Ecoflex 1 Part A: 1 Part B (containing 2 wt% Slo-Jo) with 0.5 wt% Thivex and degassed in a vacuum chamber to remove trapped air. The filler fluid was prepared by mixing 1 Part A: 1 Part B (2 wt% Slo-Jo) with 10 wt% Silicone Thinner and then degassed. The filler fluid layer was 1 mm thick on top of the 3 mm thick reservoir layer. The nozzle was 1.5 mm from the base of the Petri dish during printing at a constant speed of 1 mm/s. A constant needle diameter of 0.41 mm was used to print 1.5 wt%, 2 wt%, and 2.5 wt% Ecoflex/CNT at extrusion pressures of 172 kPa, 241 kPa, and 310 kPa, respectively. The embedded sensors were fully cured at 90 °C for 1 h, 3 h, and 9 h respectively. Additional 1.5 wt% printed samples were prepared by curing at various temperatures including room temperature, 90 °C, and 150 °C for 24

h, 1 h, and 0.5 h, respectively. Ink with 1.5 wt% CNTs was printed with various nozzle diameters including 0.2 mm, 0.25 mm, 0.33 mm, 0.41 mm, and 0.61 mm at constant extrusion pressures of 414 kPa, 345 kPa, 207 kPa, 172 kPa, and 138 kPa, respectively and the resulting extrusion cross-sections are shown in Figure 3.1(d). Each metal needle tip nozzle was 12.7 mm long.

3.2.5 Sensor Preparation and Sensitivity Comparison

Each sensor was cut out of the cured bath, stretched to 120 % strain, and silver epoxy and copper tape were applied to the exposed DIW printed electrodes to establish a reliable electrical contact (Figure A.3, Appendix A). An Instron 3345 single column mechanical testing machine was used with a 100 N load-cell in conjunction with a Hioki RM3545-02 Resistance Meter to measure the resistance of the sensors during each experiment. Samples with CNT loadings of 1.5 wt%, 2 wt%, and 2.5 wt% were loaded and unloaded with a quasi-static strain rate of 0.5 %/s up to 100 % maximum strain. Each fabricated sensor was dynamically loaded at a constant strain rate of 50 %/min for 15 cycles of 10 %, 25 %, 50 %, and 100 % strain.

3.2.6 Sensor Characterization

The most sensitive 1.5 wt% sensor printed with the 0.41 mm nozzle and cured at 150 °C was loaded for 15 cycles of 10 %, 25 %, and 50 % maximum applied strain at varying strain rates including 10 %/min, 50 %/min, 100 %/min, 250 %/min, 500 %/min, and 1000 %/min. The sensor was loaded stepwise at a constant strain rate of 100 %/min up to maximum strains of 10 %, 25 %, and 50 % including pauses for 6 s, 15 s, and 30 s respectively at maximum and minimum strains. The sensor was also stretched stepwise at a strain rate of 0.5 %/s, pausing for 10 s at each 10 % strain increment, up to 50 % maximum strain. A 400-cycle test was applied to the sensor at a constant 100 %/min strain rate up to 50 % maximum strain.

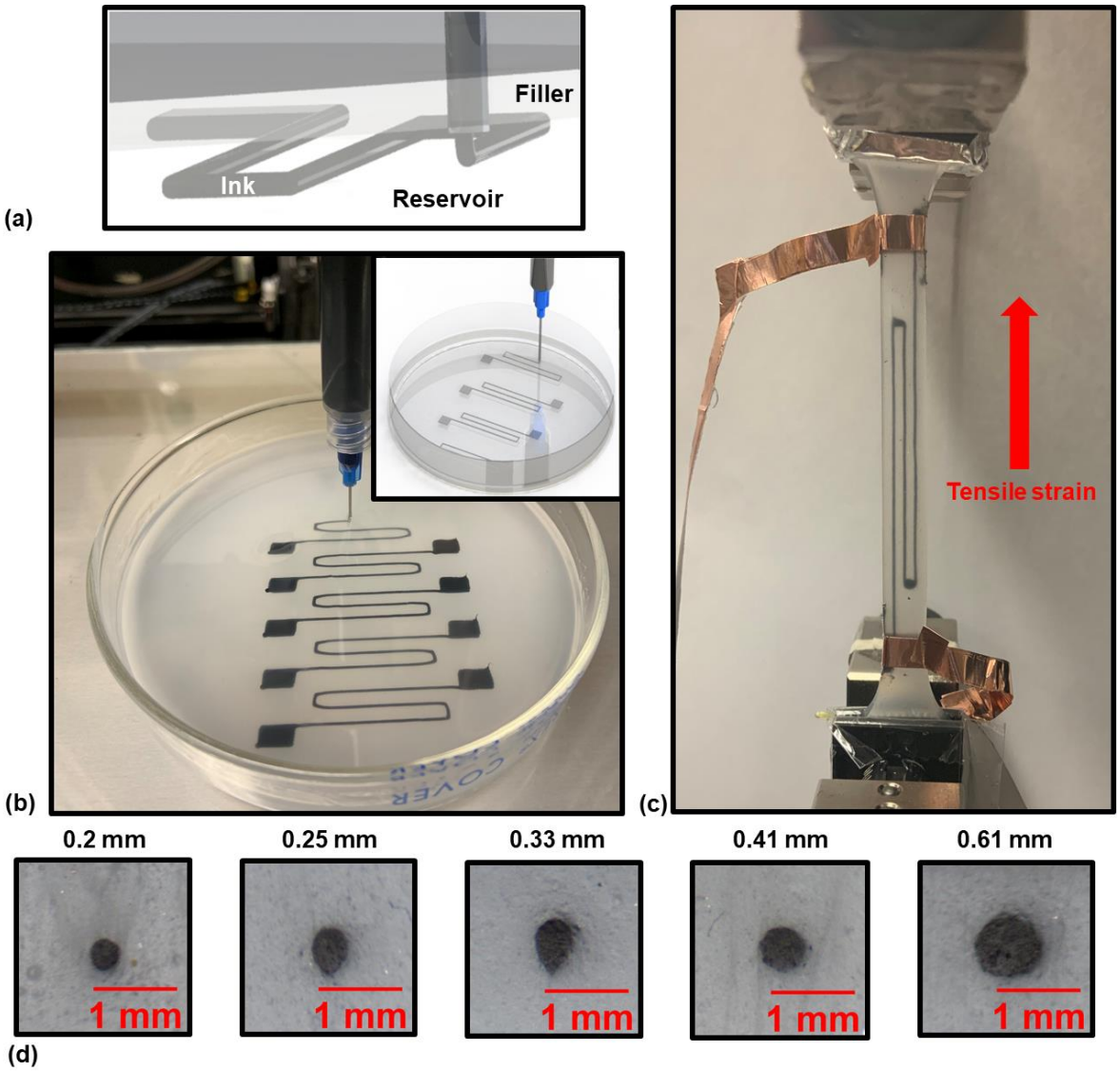

Figure 3.1: *Pictures and schematic illustrations of the (a) e-3DP process including the Ecoflex/CNT ink, filler, and reservoir, (b) sensor fabrication process, (c) experimental setup used for strain sensing tests, and (d) cross-sectional images of the embedded sensor path fabricated with various nozzle diameters.*

3.3 Results and Discussion

3.3.1 Electrical Properties

The percolation curve of the Ecoflex/CNT nanocomposite material is shown in Figure 3.2(a), in addition to the resistance of the sensors fabricated with loadings 1.5 wt%, 2 wt%, and 2.5 wt%. As

expected, the conductivity of the nanocomposite material increased significantly as the loading of CNTs increased. The percolation threshold of Ecoflex/CNT was found to be 0.6 wt%. The resistance of the fabricated sensors increased by almost 700 % as the loading of CNTs decreased from 2.5 wt% to 1.5 wt% as expected. Due to the sensor design containing a thin 90 mm-long nanocomposite wire, the lowest loading capable of producing conductive strain sensors was found to be 1.5 wt%. As often reported in the literature, nanocomposite strain sensors with lower loadings of CNTs closer to the percolation threshold typically demonstrated better piezoresistive sensitivity [43, 152, 153]. The relative change in the number of conductive networks when strain is applied is generally larger when fewer initial conductive networks are present due to the dominance of tunneling resistance at lower conductive loadings.

3.3.2 Piezoresistive Sensitivity Optimization

To optimize the manufacturing parameters to produce the most sensitive nanocomposite sensor, dynamic piezoresistive strain sensing tests were performed. To compare the sensing functions of the fabricated embedded sensors, the resistance of the sensor was measured throughout each test, and the relative resistance change was calculated using Equation (3.1).

$$\frac{\Delta R}{R_0}(\%) = \frac{R - R_0}{R_0} \times 100\% \tag{3.1}$$

First, the sensors were loaded quasi-statically to characterize the baseline piezoresistive functionality of the sensors and to compare the sensing functions of the sensors containing varying loadings of CNTs. The quasi-static sensing test results are shown in Figure 3.2(b), displaying a nonlinear response of relative resistance change when stretched to 100 % tensile strain. The sensors

containing nanofiller loadings closer to the percolation threshold demonstrated a greater relative change in resistance due to applied tensile strain. To quantify the sensitivity of the piezoresistive sensors, the gauge factor was calculated using Equation (3.2).

$$\text{Gauge Factor} = \frac{R-R_0}{R_0 \cdot (\varepsilon-\varepsilon_0)} = \frac{\Delta R}{R_0 \cdot \Delta\varepsilon} \tag{3.2}$$

The gauge factor was determined at each applied strain, and the averages of the gauge factors were used to determine the overall sensitivity of the sensors fabricated with the specified parameters. During the manufacturing optimization process, sensors were fabricated with different CNT loadings, curing temperatures, and nozzle diameters. The average gauge factors in a wide strain range of embedded sensors with 1.5 wt%, 2 wt%, and 2.5 wt% CNT loadings are shown in Figure 3.2(c). The 1.5 wt% embedded strain sensors demonstrated the highest sensitivity with gauge factors of 2.4, 1.9, 1.2, and 0.8 for tensile strains 10 %, 25 %, 50 %, and 100 % respectively. Representative sensing signals of the sensors under dynamic loading at each strain applied are shown in Figure 3.2(d). Due to the nature of the elastomeric matrix material, hysteresis was apparent during unloading and the initial reloading at each repeated cycle and became more pronounced with lower concentrations of CNTs. The hysteresis may be explained by a bi-dimensional motion of the CNT conductive networks driven by a competition between percolating network formation and breakdown due to the Poisson effect of the elastomeric matrix [154].

Next, the curing temperature was investigated as a likely parameter that could affect the functionality of the sensor. The average gauge factors of 1.5 wt% embedded sensors cured at room temperature, 90 °C, and 150 °C are shown in Figure 3.2(e). Higher curing temperatures resulted

in moderately improved sensitivity due to reduced curing times likely limiting the amount of nanofiller subject to settlement effect. The settlement effect is a time-dependent agglomeration of the dispersed CNTs due to gravity and Van der Waals forces interacting with the nanoparticles while the nanocomposite is in resin form. Several reports have modeled or visually shown CNT re-agglomeration effects and discussed their influence on the electrical and piezoresistive performance of nanocomposites [43, 155, 156]. In Chapter 2, we demonstrated a significant reduction of electrical conductivity in CNT-based nanocomposites due to just 15 min of settlement effect [145]. Due to the expected influence of the settlement effect, as well as the potential for CNTs to bleed into the Ecoflex reservoir, the embedded strain sensors fabricated with the fastest curing method demonstrated the highest average gauge factor as shown in Figure 3.2(e). Therefore, 150 °C was chosen as the optimal curing temperature to produce the highest sensitivity strain sensors and was used to examine the effect of nozzle size on the sensing performance.

The extrusion-induced CNT alignment method has been implemented to produce nanoparticle alignment in the printing direction due to shear forces and flow-induced alignment mechanisms [27]. Lewicki et al. proved that carbon fibers within a polymeric matrix were highly aligned in the printing direction during the DIW 3D printing method, and the degree of the alignment could be altered by nozzle diameter, filler loading, and feed rate [27, 157]. Due to the no-slip velocity condition at the needle wall, the viscous Ecoflex/CNT resin mixture had significantly reduced flow velocities along the walls compared to the flow at the center of the nozzle. Therefore, the higher shear rates near the wall would likely produce shear-induced alignment of the CNTs along the flow direction. In addition to these shear rates, the CNTs would be subjected to varying shear stress (τ) along the radial direction as expressed in Equation (3.3)

$$\tau = \mu \frac{du}{dy} \tag{3. 3}$$

where μ is the dynamic viscosity of the fluid flow, u is the fluid flow velocity in the direction of the nozzle wall, and y is the distance away from the nozzle wall. The shear stress levels may be sufficiently high such that larger CNT clusters may break into smaller ones and a higher degree of alignment may be achieved during extrusion.

The relative alignment of conductive nanoparticles can have a substantial effect on the electrical conductivity and piezoresistive performance of CNT-based nanocomposites due to the high aspect ratio of the nanotubes. Previous studies have used varying DIW nozzle diameters, or other methods of controlling CNT alignment in nanocomposites, to improve the piezoresistive sensitivity in the alignment direction of CNT-based strain sensors [49, 114]. In addition, analytical models have been developed to describe the increased piezoresistive sensitivity of CNT nanocomposites containing quality dispersion, loadings closer to the percolation threshold, and partial nanoparticle alignment in the direction of applied strain [115, 116]. Therefore, the nozzle size needed to be optimized in this study as well to produce embedded CNT-based strain sensors with the highest sensitivity. The average gauge factors in a wide strain range for varying nozzle diameters are shown in Figure 3.2(f). The nozzle with an inner diameter of 0.41 mm proved to contribute the most beneficial partial CNT alignment for piezoresistive strain sensing, producing an average gauge factor of 1.8. Therefore, the manufacturing optimization studies determined that the optimal fabrication parameters to produce the highest sensitivity sensors were a 1.5 wt% CNT loading, 150 °C curing temperature, and a nozzle diameter of 0.41 mm.

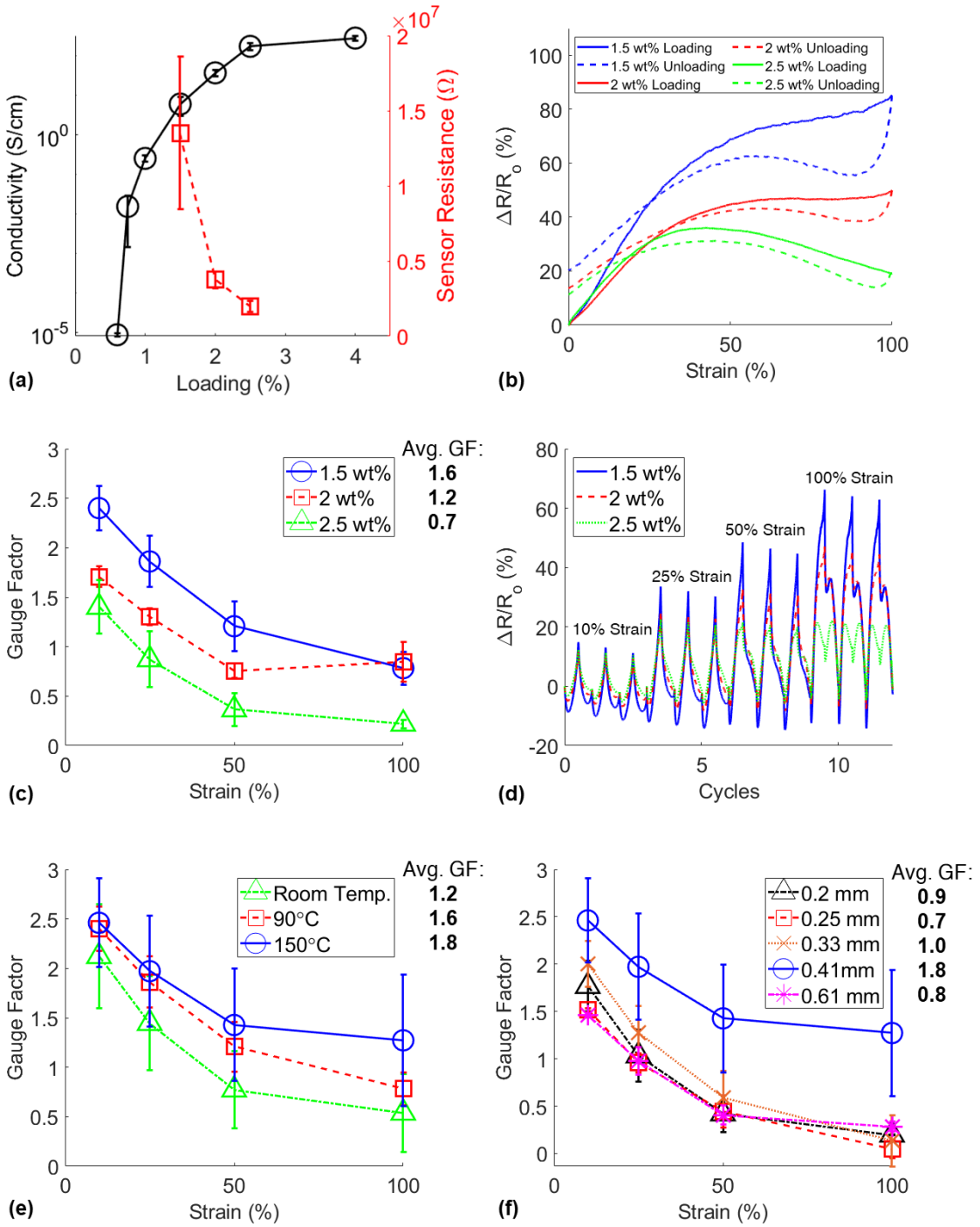

Figure 3.2: *(a) The electrical percolation curve for Ecoflex/CNT and the average sensor resistances at various loadings, (b) representative quasi-static sensing of the nanocomposite sensors, (c) CNT loading influence on gauge factor and (d) representative signal responses through a wide strain range, (e) gauge factors of 1.5 wt% sensors cured at room temperature, 90 °C, and 150 °C, and (f) gauge factors of 1.5 wt% sensors printed with various needle diameters.*

3.3.3 Sensor Characterization

The most sensitive embedded sensor manufactured in this study was fully characterized as an ultrastretchable strain sensor with a wide sensing range. The maximum stretchability of the sensor was found to be greater than 500 % strain (Figure A.4, Appendix A). To fully characterize the piezoresistive behavior of the nanocomposite, the sensor was dynamically stretched at varying maximum strains and strain rates. Representative signal responses, as well as the calculated gauge factors for each strain and strain rate tested, are shown in Figure 3.3(a). The sensor showed little to no change in the sensing function between strain rates of 50 %/min and 500 %/min. However, a slight progressive decrease in the gauge factor was apparent as the strain rate increased between these two rates with an average gauge factor of 3.4 at 50 %/min to an average gauge factor of 3.1 at 500 %/min. In contrast, the lowest strain rate of 10 %/min demonstrated the lowest average gauge factor of 2.7. At a strain rate of 1000 %/min, the sensor did not produce an identifiable sensing response at 10 % strain and revealed an increase of noise within the sensing function which is likely due to the limited sampling frequency of the multimeter.

Stepwise sensing tests were performed on the embedded sensor to establish the apparent sensing function when held at different strains. Two tests were performed to display the sensing behavior of the sensor when held at maximum and minimum strains during cyclic loading, and incremental strains during one cycle. The results of these two tests are shown in Figure 3.3(b) and Figure 3.3(c), respectively. The relative resistance change of the sensor during loading and unloading was very consistent with the applied strain. As expected with these materials, the resistance steadily decreased during the periods of being held at a constant strain. However, during the incremental pauses within the unloading cycle, the sensing response shown in Figure 3.3(c) revealed some hysteresis such that the relative resistance change increased slightly during the beginning of each

unloading increment. With this exception, the embedded strain sensor consistently produced a recognizable signal output during stepwise sensing tests, which would likely translate during relevant applications of the sensor.

A durability test of 400 cycles of dynamic loading up to 50 % maximum strain was performed to demonstrate the robustness of the nanocomposite sensor, characterize the resistance drift, and investigate any changes in the signal response during long-term use. The results of the piezoresistive durability test are shown in Figure 3.3(d). The sensor demonstrated excellent piezoresistive durability with an impressively stable relative resistance change during each cycle. As demonstrated by many piezoresistive strain sensors, the first cycle exhibited a larger relative change in resistance, and the overall resistance of the sensor progressively decreased throughout the long-term dynamic sensing test [158-161].

Lastly, the stress-strain curves during loading and unloading at varying strains of 10 %, 25 %, 50 %, and 100 % are shown in Figure 3.3(e) in addition to the average elastic modulus of the sensor. The stress-strain curves showed elastic behavior remained notably consistent when different maximum strain levels were applied. In addition, the average elastic modulus of the sensor was 83.4 kPa which is significantly lower than the modulus apparent in the human epidermis (i.e., approximately 200 ± 50 kPa for the forearm dermis and 250 ± 75 kPa for the palm dermis) [162]. Therefore, the ultrastretchable sensor was soft enough to be appropriately applied to the human skin to detect strains expected during normal human movements. Overall, the optimized embedded Ecoflex/CNT sensor demonstrated improved gauge factors over previously reported Ecoflex/CNT nanocomposite sensors due to beneficial alignment imparted by the e-3DP process optimization, in addition to a very low elastic modulus applicable for skin-attachable sensors [103, 109, 163].

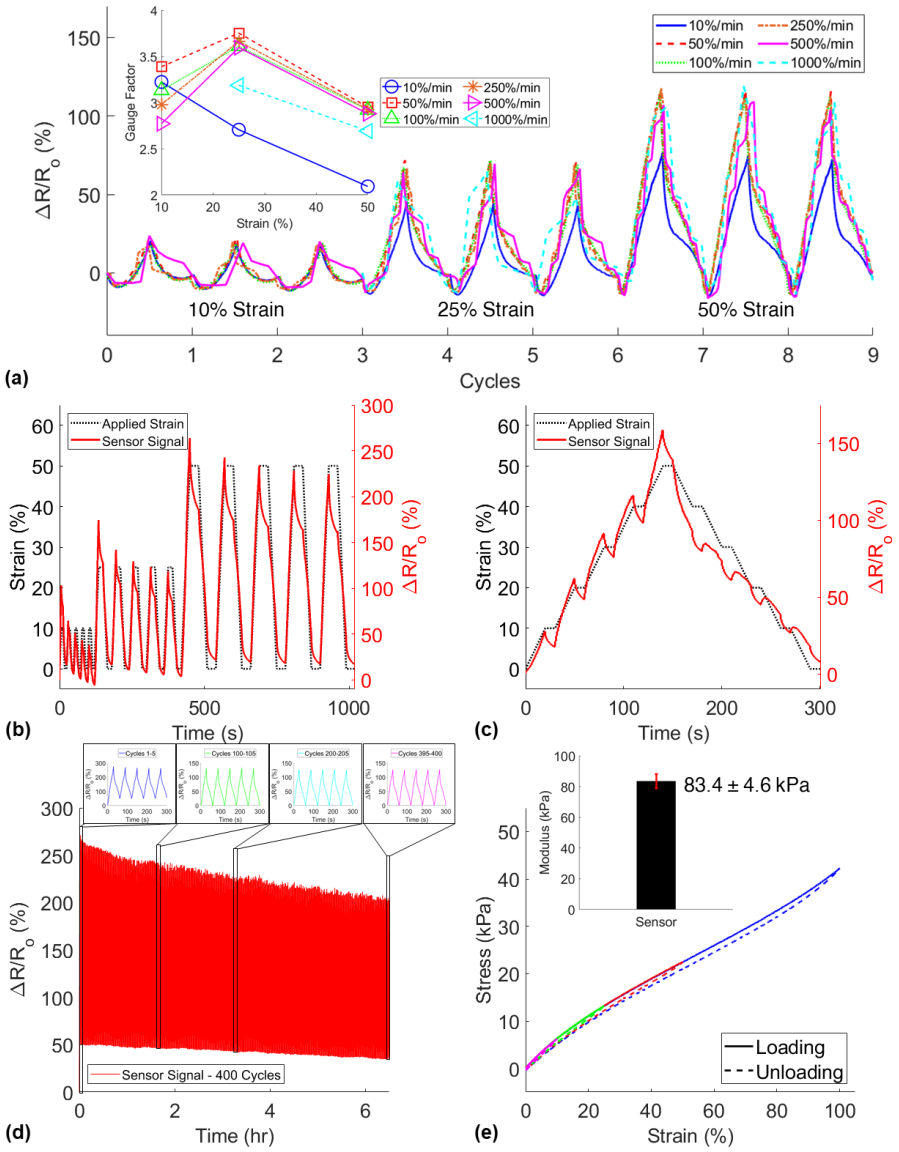

Figure 3.3: *Optimized 1.5 wt% embedded sensor characterization - (a) gauge factors and representative sensor response for varying strain rates at 10 %, 25 %, and 50 % strain. Stepwise sensing holding at (b) maximum and minimum applied strains and (c) 10 % incremental strains during loading and unloading. (d) Durability sensing test for 400 cycles of 50 % strain at 100 %/min. (e) Stress-strain curves and average Young's modulus of the skin-attachable sensor.*

3.3.4 Applications

The embedded nanocomposite sensor offered high stretchability, good sensitivity in a wide strain range, stable sensing response, and a low elastic modulus compatible with the human skin. In

addition, the nanocomposite sensing element embedded in a neat polymer offered a significant reduction in health risks associated with the use of these nanoparticles [120, 164]. The embedded strain sensor was attached to the skin of a user to detect normal human motions. The sensor was mounted to the elbow, finger, wrist, and ankle to demonstrate the versatility of the skin-attachable strain sensor. Large dynamic elbow bending motions were detected as a large strain was applied to the sensor and the resulting signal is shown in Figure 3.4(a). Alternatively, small strains were detected during dynamic finger bending shown in Figure 3.4(b), thus demonstrating a wide applicable sensing range and variety of dynamic human motions detectable by the sensor. In addition, stepwise sensing was detected on both the wrist and the ankle during wrist bending and calf raises with pauses at both the unstretched and maximum stretched positions. The signal responses of the sensor for the stepwise sensing applications are shown in Figure 3.4(c) and Figure 3.4(d). These results confirm that the developed embedded skin-attachable sensors can be integrated on many joints on the body to detect large and small bending and extension motions during normal human actions.

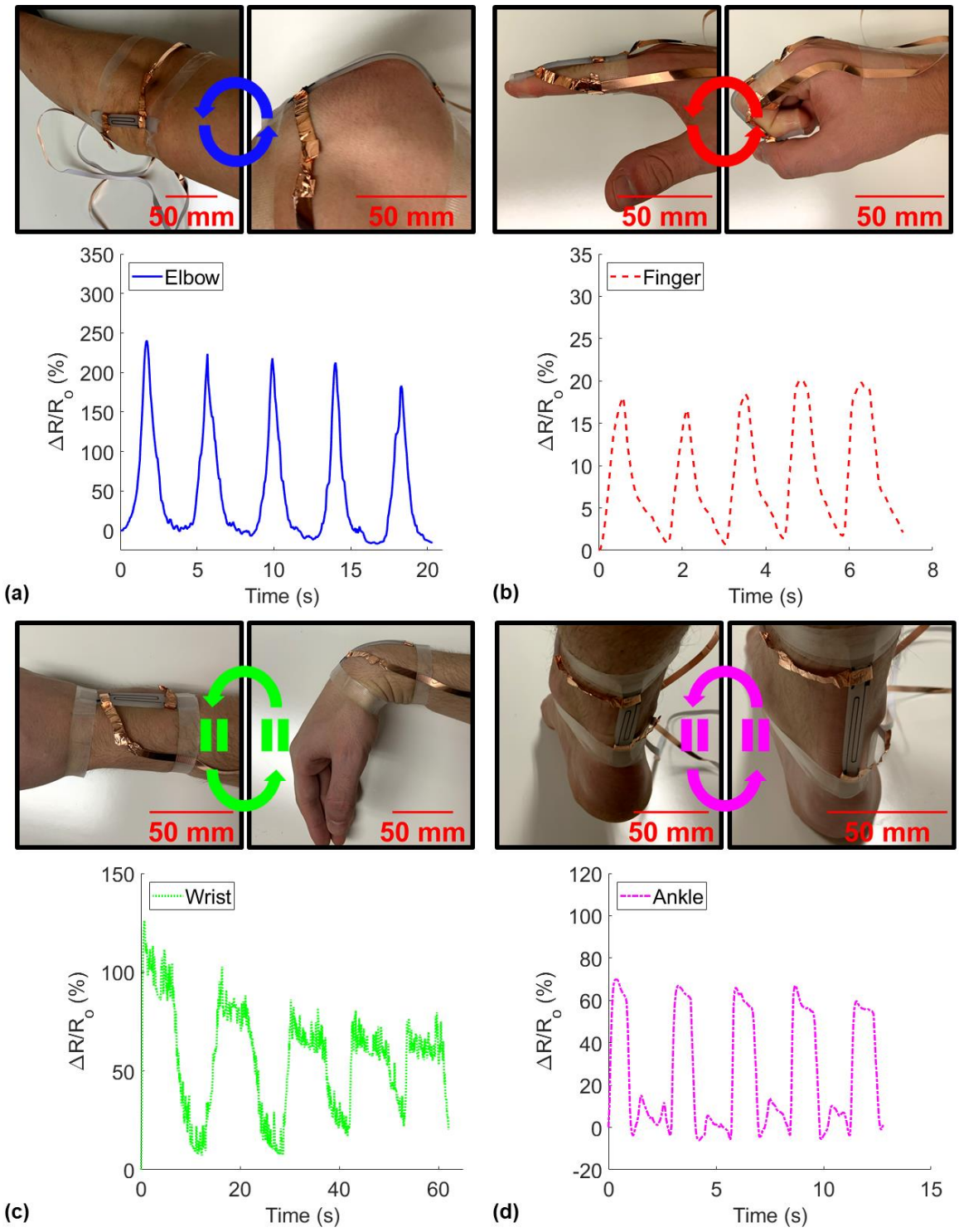

Figure 3.4: *Skin-attachable sensor applications demonstrating sensor response during dynamic cyclic bending of the (a) elbow and (b) pointer finger, and during stepwise sensing when attached to the (c) wrist and (d) ankle.*

3.3.5 Embedded Printing Capability

To demonstrate the complex printing capabilities of the e-3DP process, two printing techniques were explored. The first included printing a University of Oklahoma logo and an intricate triangular-shaped illusion within a 2 mm-deep bath to prove the potential to fabricate embedded 2D complex designs shown in Figure 3.5(a) and Figure 3.5(b). This capability could prove useful for future design and manufacturing of embedded thin elastomer circuits and sensors. In addition, a 15 mm tall embedded vertical coil was printed within the Ecoflex bath. The free-standing design of the coil shown in Figure 3.5(c) was supported by the reservoir material during the printing process shown in Figure 3.5(d) allowing the deposited nanocomposite resin to maintain its location after deposition. The fully cured embedded nanocomposite coil is shown in Figure 3.5(e). This printing capability demonstrated the potential for freeform 3D design and fabrication of embedded nanocomposites using the e-3DP method.

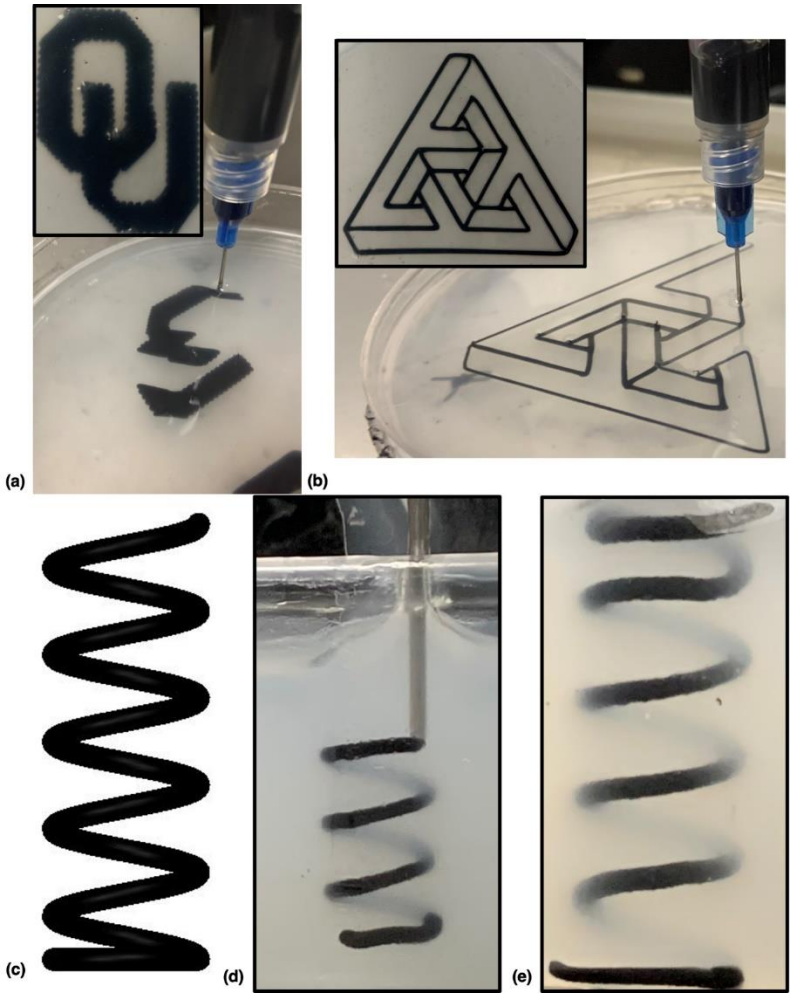

Figure 3.5: *Pictures of embedded printing of a 2D (a) University of Oklahoma logo and (b) triangular-shaped illusion. Printing of an embedded coil including the (c) design, (d) the e-3DP process, and (e) the fully cured embedded nanocomposite coil.*

3.4 Conclusions

Ultrastretchable strain sensors were fabricated via the e-3DP process to develop a fully cured sensor with a wide strain range, good sensitivity, high durability, and low modulus for use as a skin-attachable human motion detecting device. Nanocomposites composed of Ecoflex and well-dispersed CNTs were mixed at different CNT loadings to investigate the optimal nanoparticle concentration that would result in the highest sensitivity of the sensor. In addition, fabrication parameters such as curing temperature and nozzle size were optimized to produce the highest

average gauge factor in a wide sensing range. The optimal sensor consisting of 1.5 wt% Ecoflex/CNT nanocomposite printed with a 0.41 mm inner diameter nozzle and cured at 150 °C was fully characterized as a highly flexible strain sensor that can repeatedly detect up to 100 % strain. Piezoresistive characterization tests performed on the most sensitive fabricated sensor revealed little variance of the signal response between strain rates of 50 %/min – 500 %/min, good stepwise sensing functionality, high durability, and a low Young's modulus suitable for use on the human skin. These characteristics of the ultrastretchable strain sensor proved to be beneficial for the detection of a large variety of human body movements accurately when attached to the skin of a user. Additionally, complex designs were printed to demonstrate the unique fabrication capabilities of the e-3DP manufacturing process.

CHAPTER 4: FLEXIBLE PIEZORESISTIVE SPONGE SENSORS

4.1 Introduction

4.1.1 Motivation

During the studies focused on microwave-curing PDMS/CNT, two observations were made that inspired the study in this chapter. The first was that the bulk sensors were not easily compressible, and therefore were not very well suited for comfortable human motion detection. The second was that the elastomeric nanocomposite expanded due to thermal shock when exposed to microwave irradiation. Therefore, highly compressible sponge nanocomposite sensors were desired, and to stay in line with the previous study, the nanoparticles were embedded in the polymer to reduce the potential for nanoparticle detachment since the sensor would be used on a human body. Additionally, the observed expansion of the nanocomposite polymer under microwave irradiation could be used to increase the rate of porogen removal, a time-consuming step that has been reported as a notable struggle in the field of PDMS sponge fabrication. In this way, the following study aligns with the focus of this work including rapid microwave-based nanocomposite fabrication and flexible strain sensing for human motion detection. The studies in this chapter have been published in Nanomaterials [165].

4.1.2 Background

In this study, PDMS sponges containing dispersed CNTs were developed for human motion detection applications. A novel microwave irradiation method was used to rapidly remove the sugar porogen of a fully cured heterogeneous mixture of sugar and PDMS containing embedded

CNTs. During the microwave-assisted porogen removal, the fully cured CNT-based nanocomposite absorbed significant heat and likely expanded the sponge walls to allow water to easily flow through the continuous open-cell pores and dissolve the sugar rapidly. The electrical, piezoresistive, and mechanical properties of the sensors were tailored by adjusting the CNT loading and sugar porogen amount. An SEM was utilized to image the microstructure, the quality of nanofiller dispersion, and to confirm the CNTs were embedded within the polymer. The sensor properties were fully characterized, and various sensing applications were demonstrated including implementation on a 3D printed prosthetic hand and skin-attachable human motion detection.

4.2 Experimental Methods

4.2.1 Materials

The multi-walled CNTs with an average diameter between 50 – 90 nm and aspect ratios > 100 were purchased from Sigma-Aldrich. The THF was obtained from Sigma-Aldrich. The Sylgard 184 PDMS kit was purchased from Dow Corning. Sugar was purchased from Walmart. Unless otherwise noted, all materials were used as received and as the manufacturer recommended.

4.2.2 Nanocomposite Sponge Fabrication

The nanocomposite sponge sensors were fabricated with a solvent-based sonication method to disperse the CNTs well within the PDMS matrix. The fabrication method used in this study can be seen in Figure 4.1. First CNTs were measured and mixed in 50 mL of THF with a magnetic stir bar. The CNT suspension was then ultrasonicated with a probe tip sonicator for 10 min, pulsing on for 5 s and off for 2 s. During the sonication process, PDMS Part A was measured and mixed in THF with a magnetic stir bar. After sonication, the dispersed CNT suspension was poured into

the PDMS/THF solution, mixed with a magnetic stir bar for 2 min, and sonicated for 30 min. Next, the mixture was placed on a 75 °C hot plate and mixed until the magnetic stir bar stopped spinning due to THF evaporation. Then, to fully evaporate the THF from the nanocomposite resin, the material was held under vacuum at 75 °C overnight. Next, the curing agent was added at a 1:1 ratio (Part A: Part B) and mixed by hand to create the nanocomposite prepolymer (PDMS/CNT). A predetermined amount of sugar porogen was added to PDMS/CNT and mixed by hand. The moldable nanocomposite mixture was cured in an oven at 110 °C and a razor blade was used to cut out cube-shaped sensors of roughly 10X10X10 mm. Nanocomposite sponges were prepared at a constant sugar porogen amount of 70 wt% with a varying CNT loading including 1.5 wt% (CNT1.5P70), 2 wt% (CNT2P70), 2.5 wt% (CNT2.5P70), and 3 wt% (CNT3P70). Additionally, sponges were fabricated at a constant CNT loading of 3 wt% and varying sugar porogen amounts including 75 wt% (CNT3P75), 80 wt% (CNT3P80), and 85 wt% (CNT3P85). Designations for the sponge materials fabricated in this study are also shown in Table A.1.

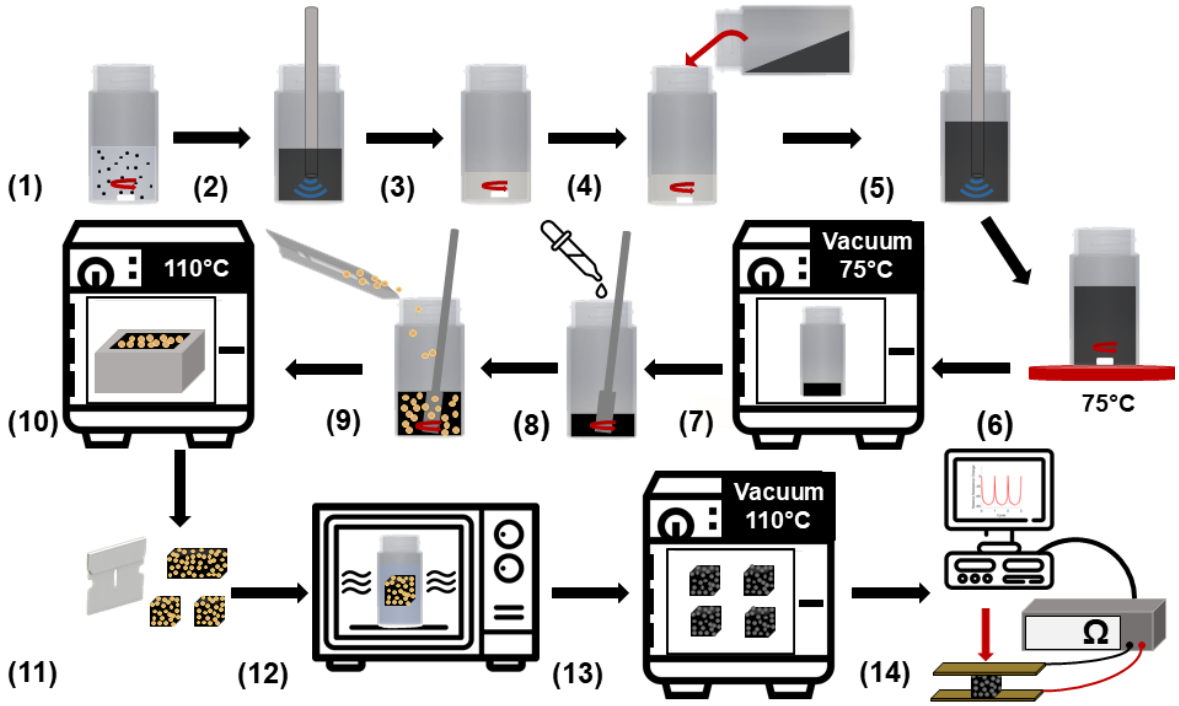

Figure 4.1: *Schematic of the fabrication method used to manufacture the highly porous nanocomposite sponge sensors.*

4.2.3 Rapid Porogen Removal

To rapidly remove the sugar porogen from the cured nanocomposite, a novel microwave irradiation leaching process was used. Each sample was placed in a glass bottle with 100 mL of distilled water and heated under microwave irradiation for several pulses, replacing the water after each pulse. A General Electric 1200-watt unmodified commercial microwave oven was used for the porogen removal process. The CNT1.5P70, CNT2P70, CNT2.5P70, and CNT3P70 nanocomposite sponges were pulsed 5 times in the microwave for 60 s, 55 s, 50 s, and 45 s, respectively. The CNT3P75, CNT3P80, and CNT3P85 sponges were pulsed 5 times in the microwave for 43 s, 40 s, and 37 s, respectively. After complete removal of the sugar porogen, the samples were dried in a vacuum oven overnight. To quantify the rate of porogen removal, fully

cured 3 wt% nanocomposite samples containing 70 wt% sugar, were weighed between each microwave pulse after drying the samples completely.

4.2.4 SEM

Before imaging with a Zeiss Neon EsB SEM, each sample was sputter-coated with approximately 10 nm of AuPd to diminish charging artifacts. The pores of each sample containing a constant CNT loading (3 wt%) and various loadings of sugar porogen (70 wt%, 75 wt%, 80 wt%, and 85 wt%) were imaged to compare the microstructure of the sponges. In addition, CNTs were imaged on the cut surface of the sponge to confirm a high-quality nanoparticle dispersion was achieved within the elastomeric matrix, and an uncut surface was imaged to show the quality of CNT embedding in the matrix.

4.2.5 Piezoresistive Sensor Characterization

To investigate and compare the performance of each sensor fabricated in this study, dynamic compression tests were performed on an Instron 3345 single column mechanical testing machine with a 100 N load cell. The piezoresistive sensors were placed in between two copper plates that were electrically connected to a Hioki RM3545-02 Resistance Meter to measure the resistance of the semiconductive sensor throughout each dynamic compression test. Using this experimental setup, the sensors were cyclically compressed for 10 cycles at each maximum strain including 2 %, 3 %, 5 %, 10 %, 25 %, and 50 % at a constant strain rate of 2 %/s. The mechanical properties including the stress-strain curves and compressive moduli were determined from the first cycle of 50 % maximum strain. The piezoresistive functionality including the durability and strain rate dependence of the CNT3P70 and CNT3P85 were compared. The durability test included 360 cycles of 50 % maximum compressive strain at a constant strain rate of 50 %/min. The varying

strain rate test included 10 cycles at each strain rate (20 %/min, 100 %/min, 250 %/min, 500 %/min, and 1000 %/min) for each compressive strain (5 %, 10 %, 25 %, and 50 %) applied.

4.2.6 Flexible Sensor Applications

The piezoresistive sensors were attached to the fingertips of a 3D printed prosthetic hand with PDMS sleeves and copper tape electrodes. The sensors demonstrated a change in resistance due to the pressure-induced on the fingertips of the prosthetic while cyclically grabbing an object. Additionally, the sensors were taped on the chest, inside of the elbow, and behind the knee of a user. The user compared basic human motions including breathing slow versus fast, walking versus running, and elbow bending versus a throwing motion to demonstrate the ability of the sensor to detect human motions.

4.3 Results and Discussion

4.3.1 Rapid Porogen Removal

Porosity controllability is an important capability for piezoresistive sponge fabrication that most methods lack. Porosity has a major impact on the mechanical and piezoresistive properties of these porous sensors. Porous sensor manufacturing methods should have the ability to control the porosity of the sensors as the compressibility of the sponge sensors may greatly influence the appropriate applications, pressure sensitivity, and viscoelastic behavior. The fabrication method developed in this study allows the manufacturer to significantly vary the porosity and compressive modulus of the sensors by varying the sugar porogen amount between 70 wt% - 85 wt%. The varying porosity measurements of the fabricated sensors and the percentage of sugar porogen removed for each microwave pulse are shown in Figure 4.2.

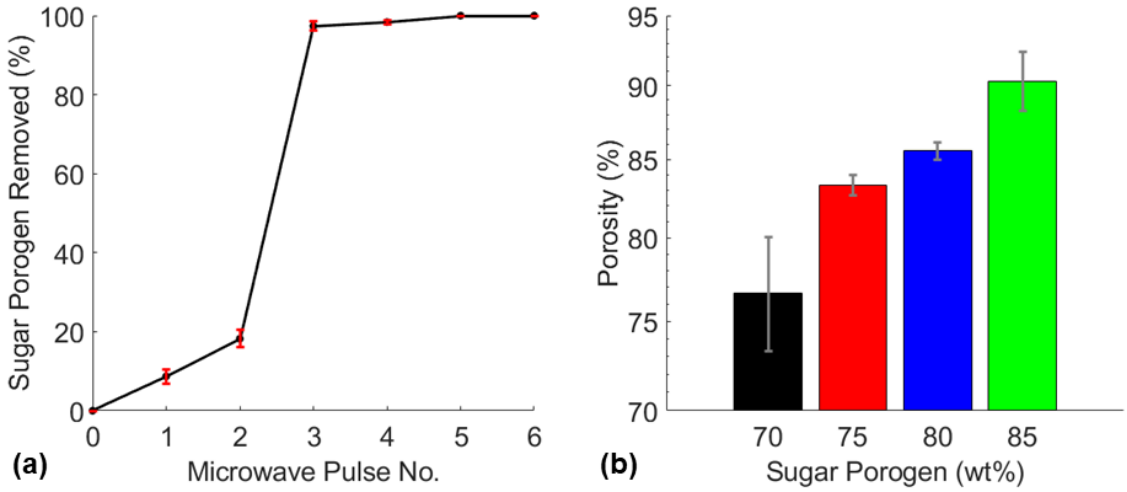

Figure 4.2: *(a) Sugar porogen removed after each microwave pulse of CNT3P70 sponges and (b) the varying porosities of CNT3P70, CNT3P75, CNT3P80, and CNT3P85 sponges.*

The quantification of sugar porogen removal during the microwave-based leaching process shown in Figure 4.2(a) revealed the sugar porogen was 100 % removed after the fifth pulse. Additionally, the experiment showed that 80 % of the total sugar porogen was removed from the third microwave pulse. This may likely be explained by the fully cured sugar infiltrated nanocomposite being unable to expand under microwave irradiation in the first two pulses due to the sugar template constricting the elastomer. However, before the third pulse, almost 20 % of the sugar porogen had been removed which allowed the sponges to expand and open the pores of the sample, leading to significant porogen dissolution due to microwave-induced thermal expansion. The last two pulses removed residual sugar that remained on the pore walls of the sponge. The fabrication technique demonstrated the ability to remove sugar porogen amounts of 70 wt%, 75 wt%, 80 wt%, and 85 wt% which produced nanocomposite sponges with porosities of 77 %, 83 %, 86 %, and 90 % respectively as shown in Figure 4.2(b).

Many studies have used a variety of materials as a porogen to create PDMS sponges and several mentioned the difficulty and time-consuming process typically required to remove the porogen. Table 4.1 shows the time required to remove the porogen in this study versus other studies that reported this time. Nanoparticles in parenthesis were attached to the surface of a neat PDMS sponge (after porogen removal) while nanofiller listed after a slash were dispersed within the PDMS matrix (before porogen removal). This is noteworthy as typically the stiffness of an elastomer is increased with nanofiller making porogen removal more difficult. However, this study used the embedded CNTs to aid in the porogen removal process, resulting in a process that required less than 5 min to complete. This impressive time efficiency demonstrated the potential for this method to be valuable for the mass production of these nanocomposite sponges.

Table 4.1: *Comparison of time required to remove the porogen via microwave-assisted dissolution with different porogen removal methods used to fabricate PDMS sponges.*

Material	Porogen	Removal Method	Time	Reference
PDMS/CNT	sugar	underwater microwave irradiation	< 5 min	this work
PDMS/CNT	sugar	boiling water & sonication	> 24 h	[129]
PDMS/CNT	salt	immersed in heated water	72 h	[58]
PDMS/$SrTiO_3$	salt	stirring in water	4 h	[117]

PDMS	polycaprolactone	sonication in acetone	1 h	[118]
PDMS	salt	dissolution in water	12 - 24 h	[166]
PDMS	polystyrene spheres	dissolved in acetone	24 h	[167]
PDMS	sugar	dissolution in water	24 h	[168-170]
PDMS	citric acid monohydrate	dissolved in ethanol	6 h	[171]
PDMS (graphene)	nickel	15 wt% HCL immersion	12 h	[172]
PDMS (graphene)	sugar	sonication in water	2 h	[56]
PDMS (graphene)	salt	dissolution in heated water	72 h	[173]
PDMS (nanodiamond)	sugar	dissolution in water	3 h	[174]
PDMS (CNTs)	sugar	sonication in hot water	1 h	[119]

4.3.2 Sponge Structure

The goal of developing these flexible nanocomposite sensors was to make a device that was highly porous for high compressibility and safe for use on the human body. Several studies in the field have used a simple dip-coating method to attach nanoparticles to the surface of foam or sponges to functionalize the material [52-54]. However, many of these studies ignored the high likelihood

of nanoparticle detachment from these materials. Detachment of CNTs from a sponge during use as a skin-attachable human motion detection device may introduce serious health risks to the users [120, 175]. In this study, CNTs were dispersed well within the PDMS matrix to significantly reduce the risk of nanoparticle detachment. Therefore, the piezoresistive behavior of the sensors may largely be attributed to the collapsing of semiconductive pores within the samples during compression as illustrated in Figure 4.3. Additional likely piezoresistive mechanisms in the compression sensors include surface effects including the contact between the elastomeric nanocomposite and copper electrodes and a reduction in average tunneling distance as conductive nanofiller are brought closer together within the matrix.

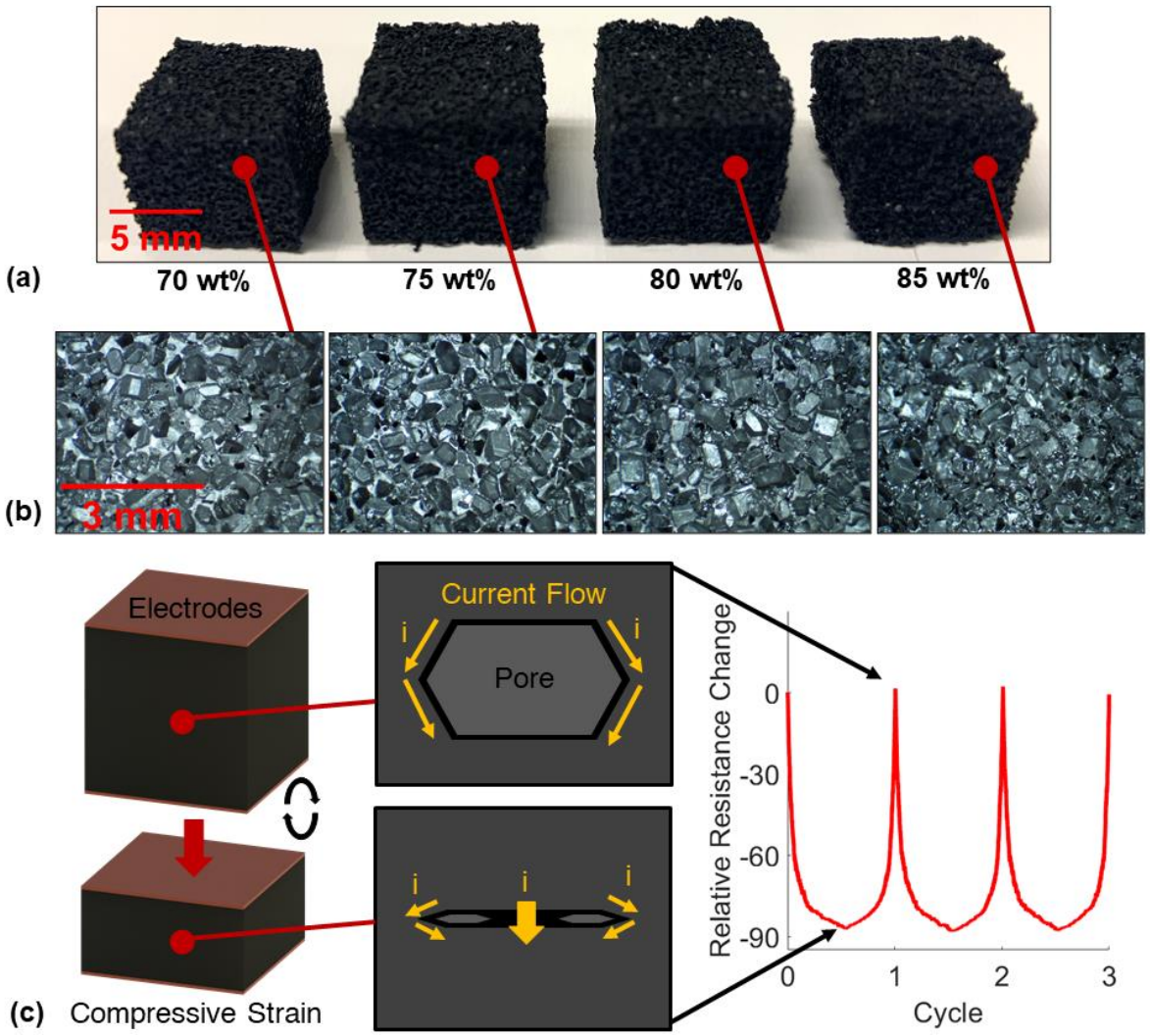

Figure 4.3: *(a) Picture of the various porosity sponges with CNT loadings of 3 wt%, (b) microscopic images of the microstructure of the varying porosity sponges, and (c) a schematic illustrating the collapsed pore piezoresistive mechanism in the sponge sensors.*

To visually investigate the structure of the sponges including the varying porosity, quality of CNT dispersion within the matrix, and determine if CNTs were successfully embedded into the polymer, SEM images were taken. First, the microstructures of the varying porosity sponges were imaged and the results for CNT3P70, CNT3P75, CNT3P80, and CNT3P85 are shown in Figure 4.4. As expected, a higher porosity sponge displayed a greater number of pores visible in the microstructure. These pores were a pathway for water to travel during the porogen removal

process, which explains why removing the sugar was easier and required shorter microwave pulse times for samples with a higher amount of sugar porogen. Next, the nanostructure of a sponge was imaged, and the results are shown in Figure 4.5. A surface that was cut with a razor blade was imaged to determine the quality of CNT dispersion within the matrix. No noticeable agglomerates were seen during imaging and the images shown in Figure 4.5(a) and Figure 4.5(b) demonstrated a uniform distribution of CNTs within the PDMS matrix. Images of the uncut surface of the sponge shown in Figure 4.5(c) and Figure 4.5(d) confirmed the successful embedding of the CNTs within the polymer matrix.

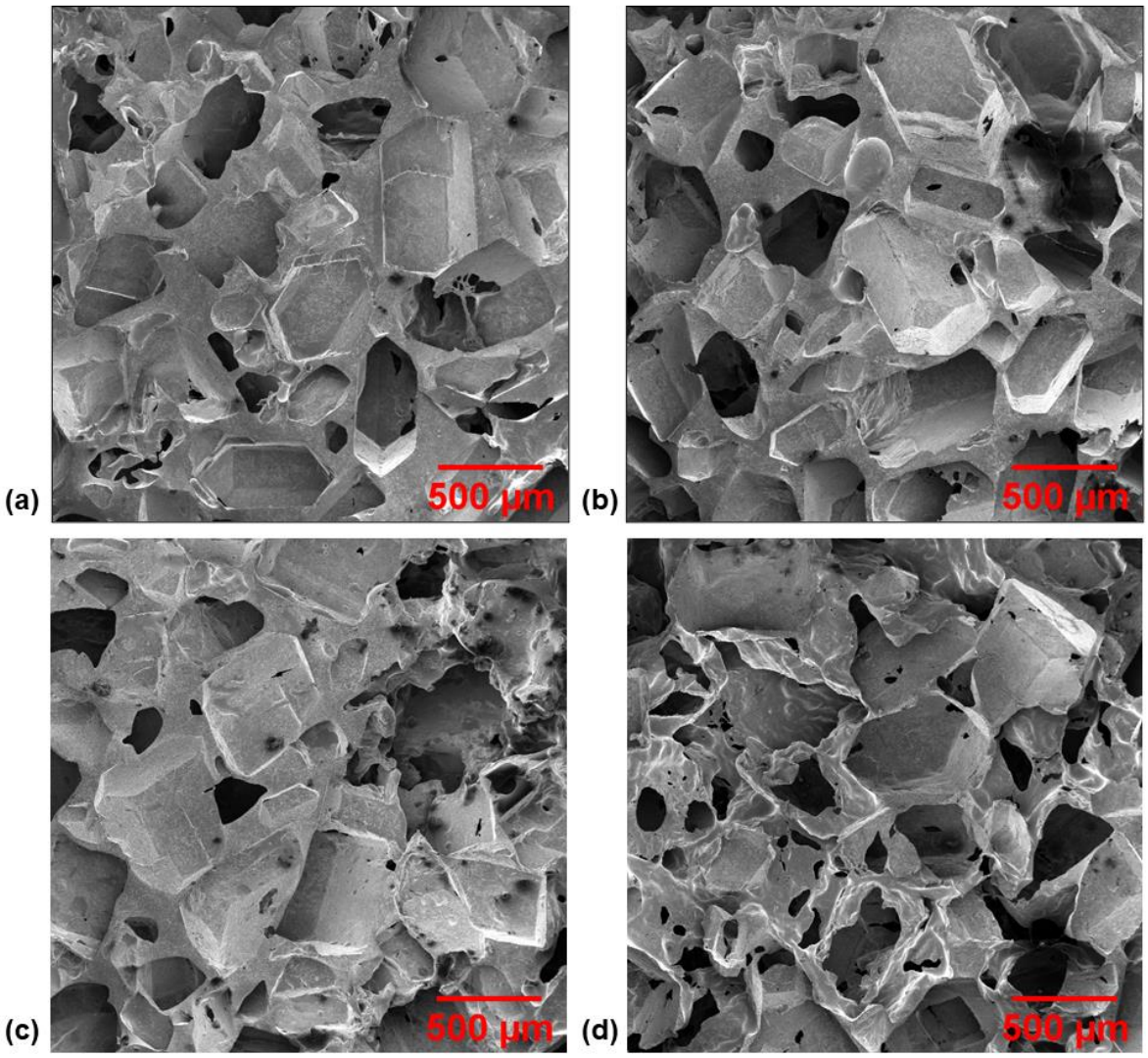

Figure 4.4: *SEM images of the microstructure of various porosity sponges with 3 wt% CNT loadings and (a) 70 wt%, (b) 75 wt%, (c) 80 wt%, and (d) 85 wt% sugar porogen.*

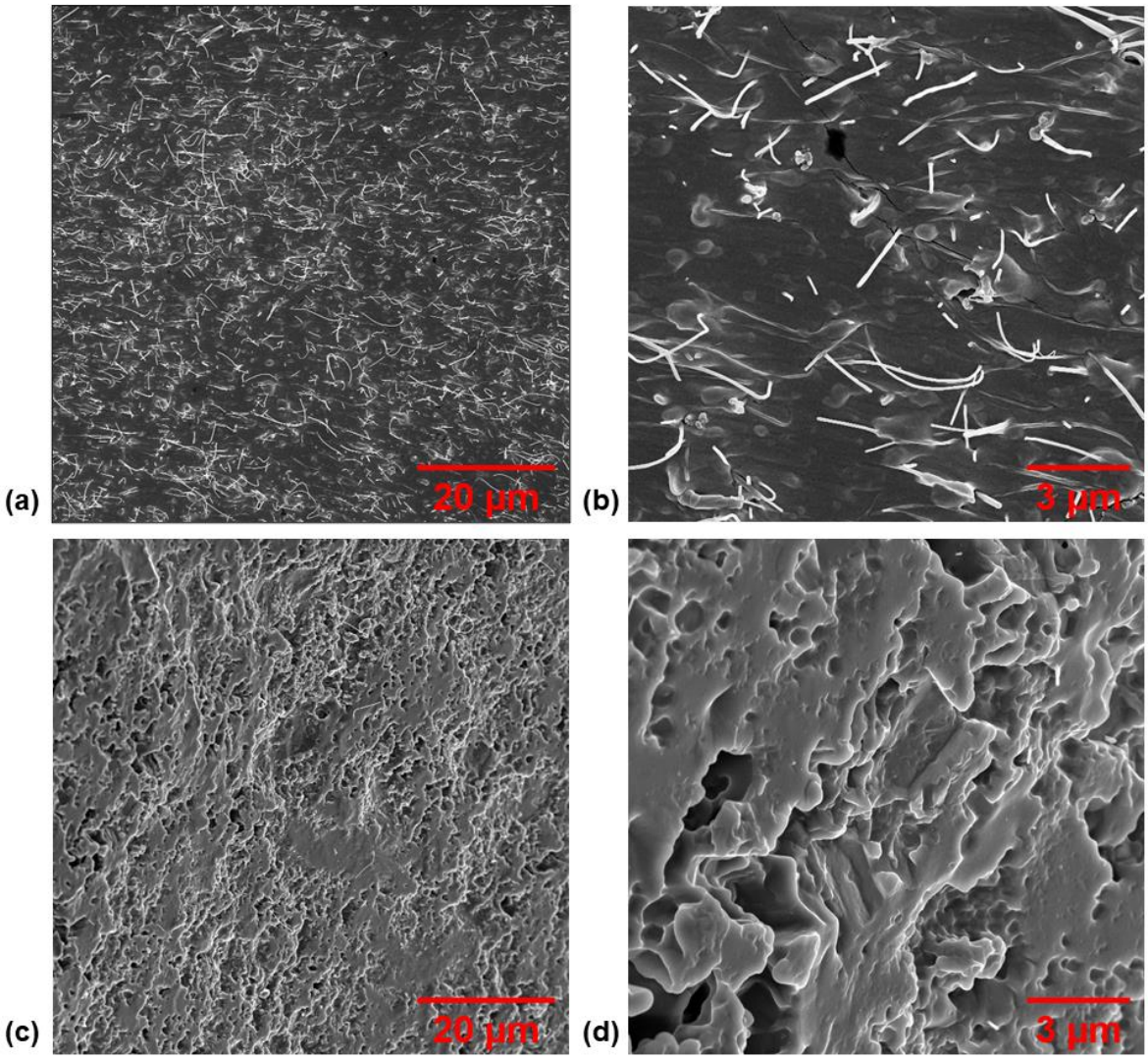

Figure 4.5: *SEM images of the nanostructure of a nanocomposite sponge including (a, b) a cut surface of sponge exposing the ends of dispersed embedded CNTs and (c, d) an uncut surface of a sponge demonstrating successful embedding of the nanofiller within the polymer matrix.*

4.3.3 Piezoresistive Sensor Characterization

The fabrication technique implemented in this study gives us the ability to fabricate piezoresistive sponges with varying porosity and varying CNT loading. Therefore, it was necessary to characterize and compare the piezoresistive sensitivity of the sensors fabricated with various formulations to determine the differences in behavior and benefits of certain sponge materials. The

sensitivity in a wide strain range of every fabricated sensor was compared by determining the gauge factor at each applied strain. The gauge factor was calculated using Equation (4.1).

$$\text{Gauge Factor} = \frac{R - R_0}{R_0 \cdot (\varepsilon - \varepsilon_0)} = \frac{\Delta R}{R_0 \cdot \Delta \varepsilon} \tag{4.1}$$

In this study, the preloaded strain was kept constant while the sensors were cyclically loaded at varying maximum compressive strains between 1 % - 50 %. The piezoresistive signals and the mechanical properties of each sensor were determined by these compression tests. The results of the comparison of CNT1.5P70, CNT2P70, CNT2.5P70, and CNT3P70 sponges are shown in Figure 4.6.

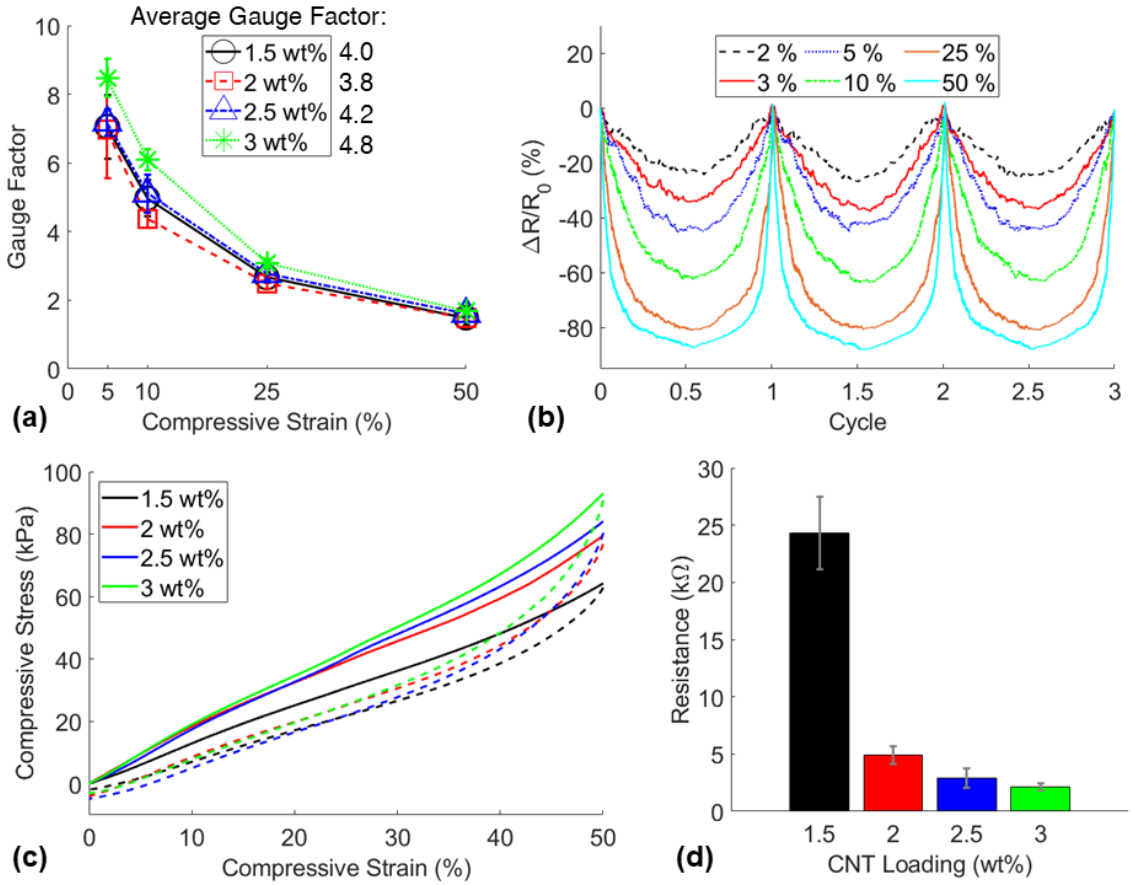

Figure 4.6: *(a) Sensitivity comparison of CNT1.5P70, CNT2P70, CNT2.5P70, and CNT3P70 sponges, (b) representative relative resistance change signals of a CNT3P70 sponge, (c) stress-strain curves of sensors in compression, and (d) the average resistances of the sensors.*

Although similar piezoresistive sensitivity was observed in each sensor, the sponges containing 3 wt% CNT loading demonstrated the highest average sensitivity with a gauge factor of 4.8 as shown in Figure 4.6(a). Additionally, the CNT3P70 sensors displayed the best minimum compressive strain detection of 2 % and the representative signals are shown in Figure 4.6(b). The mechanical properties were not significantly affected by the varied loading of CNTs with a relatively consistent compressive modulus of 160 ± 29 kPa between all the sensors. No significant trend was found for the compressive modulus or porosity of each sensor likely due to significant variances in viscosity between the nanocomposite resins [50], varying sugar particle sizes, and potential

inadequacies in the hand-mixing process resulting in varied porosities in the samples (Figure A.5, Appendix A). Representative stress-strain curves for the sponges fabricated with varied CNT loadings and consistent sugar porogen loading of 70 wt% are shown in Figure 4.6(c). The electrical properties displayed in Figure 4.6(d) demonstrated the significant impact of the nanofiller loading on the resistance of the sensors with an order of magnitude difference between CNT loadings 1.5 wt% and 3 wt%. The highest CNT loading (3 wt%) displayed the highest number of conductive networks, and therefore the lowest resistance, which proved to be beneficial for reliable contact with the copper electrodes. Due to demonstrating the highest piezoresistive sensitivity and the highest electrical conductivity, 3 wt% CNT loading was chosen to fabricate sensors with various sugar porogen amounts.

Sugar porogen amounts were varied to demonstrate the wide range of mechanical behavior of the sponges capable of being manufactured with this method. Additionally, the piezoresistive sensitivities of the sponges with various porosities were compared to determine the highest performing sensor. The results of this study are shown in Figure 4.7.

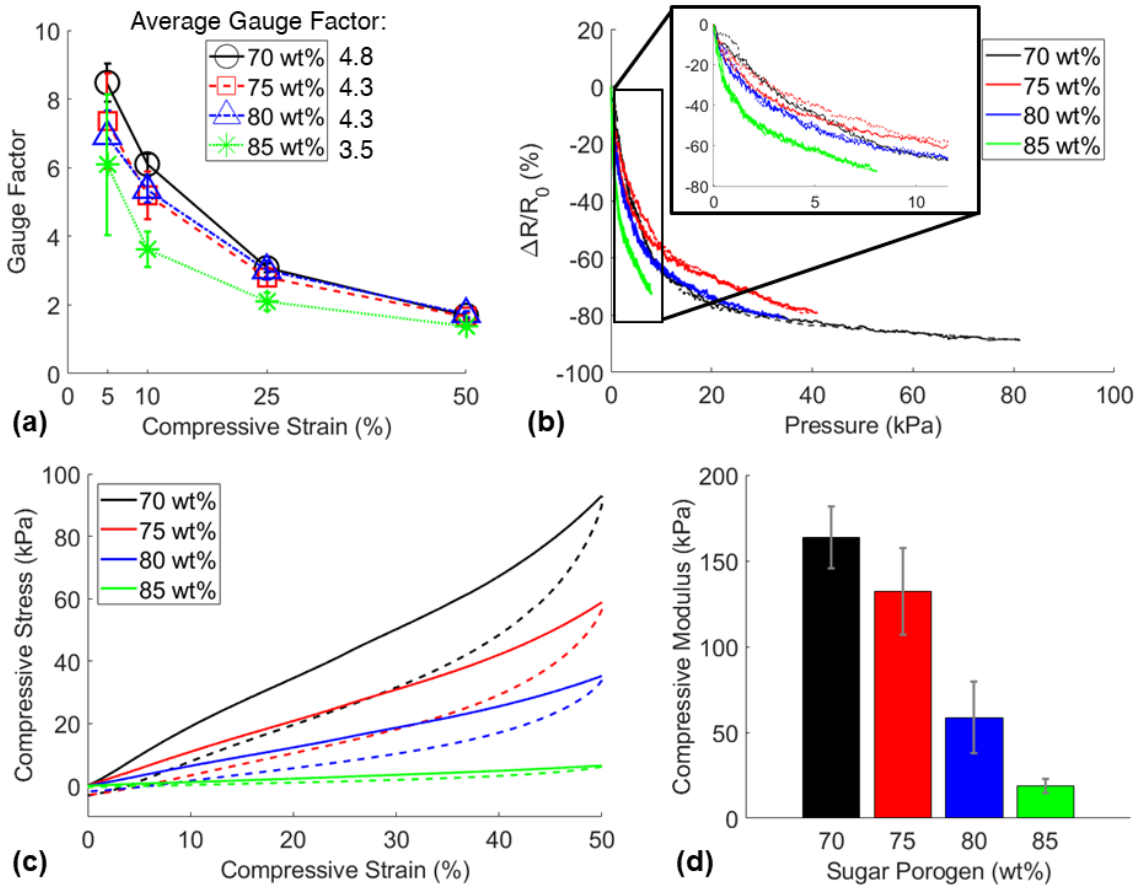

Figure 4.7: *(a) Piezoresistive sensitivity comparison of sponges fabricated with various sugar porogen amounts and 3 wt% CNT loading, (b) representative relative resistance change signals of each sensor due to pressure applied during a 50 % strain cycle, (c) stress-strain curves of sensors up to 50 % compression, and (d) the compressive moduli of the sensors.*

The lowest porosity compression sensor displayed the highest average gauge factor between the strain range 5 % - 50 % as shown in Figure 4.7(a) likely due to the pores within the more porous sponges not collapsing fully within this strain range. However, the most porous sensors fabricated with 85 wt% porogen were more sensitive to applied pressure as shown in Figure 4.7(b). This was due to the significantly lower compressive stiffness of the more porous sponges as the average compressive moduli of sensors fabricated with 70 wt%, 75 wt%, 80 wt%, and 85 wt% displayed in Figure 4.7(d) were 164 kPa, 132 kPa, 59 kPa, and 18 kPa, respectively. The stress-strain curves shown in Figure 4.7(c) denoted typical viscoelastic behavior where the area between the loading

(solid line) and unloading (dashed line) curves is the energy absorbed by the material and the area below the unloading curve is the energy returned. Clearly, the lower porosity sponges displayed greater energy absorbed and energy returned than the higher porosity sponges. This proves the key capability of the developed manufacturing method to fabricate piezoresistive sponges with controllable mechanical behaviors offering the potential for the sensors to be used in a wide variety of applications. Further comparison of the piezoresistive function for the highest porosity sponge (CNT3P85) and the lowest porosity sponge (CNT3P70) was explored to determine the differences in piezoresistive behavior for sponges with widely different porosities.

To determine the usability of these sensors, long-term durability and strain rate dependence tests were performed, in addition to stepwise sensing and viscoelastic creep relaxation tests that are shown in Figure A.6 (Appendix A) and Figure A.7 (Appendix A), respectively. The results of the durability piezoresistive compression tests are shown in Figure 4.8(a) and Figure 4.8(b). Both sensors demonstrated some inconsistencies in the relative resistance change over 12 h of cyclic compressive loading, however, the least porous sponge demonstrated the more stable piezoresistive behavior. Additionally, the CB3P70 sponge displayed more consistent piezoresistive sensitivity than the CB3P85 sponge for significantly varying strain rates as shown in Figure 4.8(c) and Figure 4.8(d). This result may be explained by the significantly larger energy absorbed and energy returned in the least porous sponge compared to the most porous sponge as shown in the stress-strain curves in Figure 4.7(c). Due to the differences in the viscoelastic responses of the material, the CNT3P70 sponge displayed more consistent piezoresistive sensitivity regardless of strain rate, except for very small strains at 1000 %/min strain rate. In contrast, the CNT3P85 sponge displayed more noticeable decreases in piezoresistive sensitivity as the strain rate increased. Overall, these additional piezoresistive tests showed that CNT3P70

sponges displayed the most dependable piezoresistive behavior, therefore, the material formulation was considered optimal and was used for sensor application demonstrations.

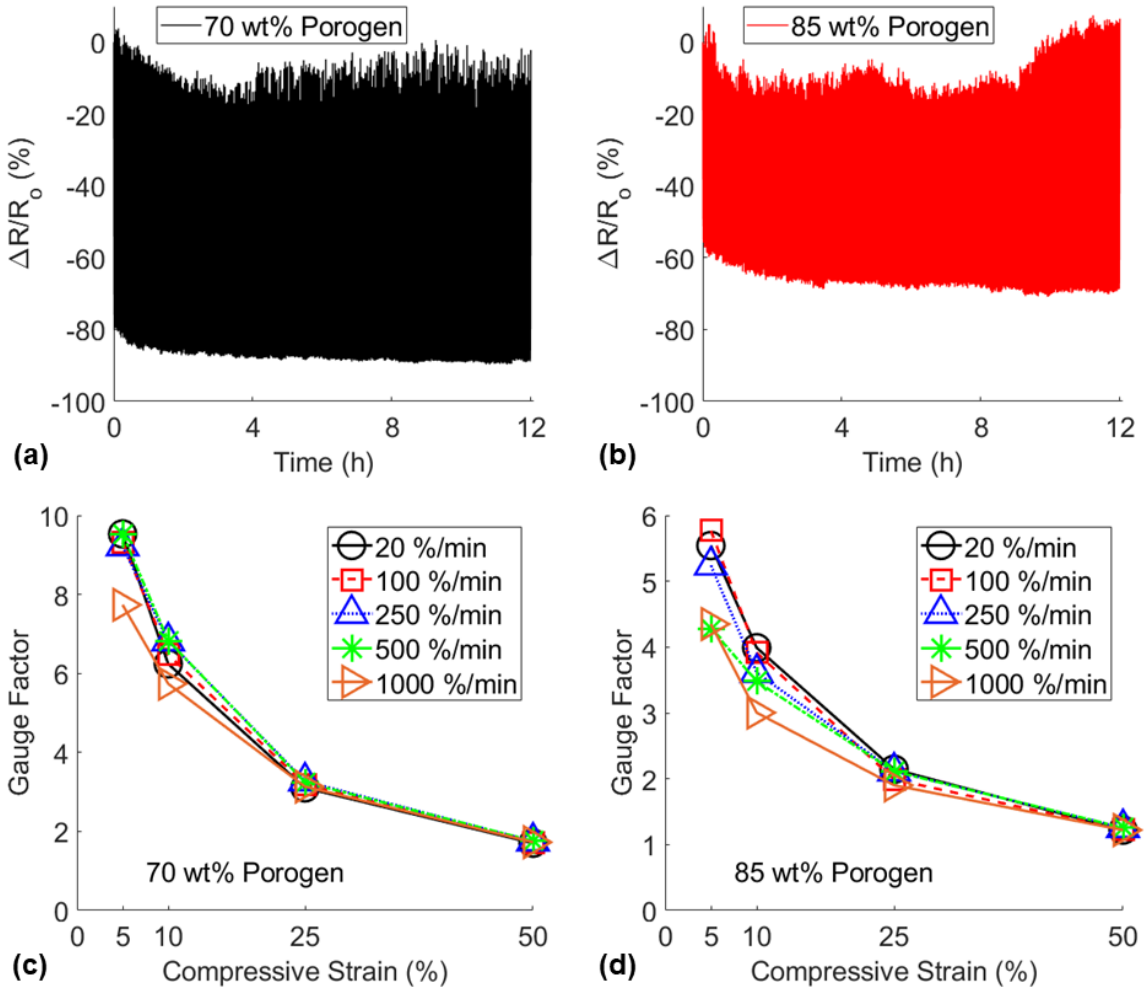

Figure 4.8: *Durability piezoresistive compressive strain sensing tests for 12 h of cyclic loading for (a) CNT3P70 and (b) CNT3P85 nanocomposite sponges. Effects of strain rate on the piezoresistive sensitivity of (c) CNT3P70 and (d) CNT3P85 sponges.*

4.3.4 Flexible Sensor Applications

It is imperative to consider the health implications when developing any nanocomposite sensor that will be attached to or used by a person as CNTs and other nanoparticles may be detrimental

to the health of humans. Many studies have fabricated highly sensitive piezoresistive sponges that have nanoparticles attached to the pore walls of a neat PDMS sponge. This common sensor manufacturing technique, when implemented for human motion detection, ignores the high likelihood that nanoparticles become detached from the surface of the elastomer due to repeated cycles and could be harmful to the health of the user and therefore not appropriate for commercial human motion detection products. This study embedded the nanoparticles within the polymeric matrix to significantly reduce the likelihood of nanoparticle detachment during use. This advantage made the sensors in this study more applicable for skin-attachable sensors and prosthetic sensors for dynamic and stepwise motion detection. Piezoresistive signals of the sensors during the applications demonstrated are shown in Figure 4.9.

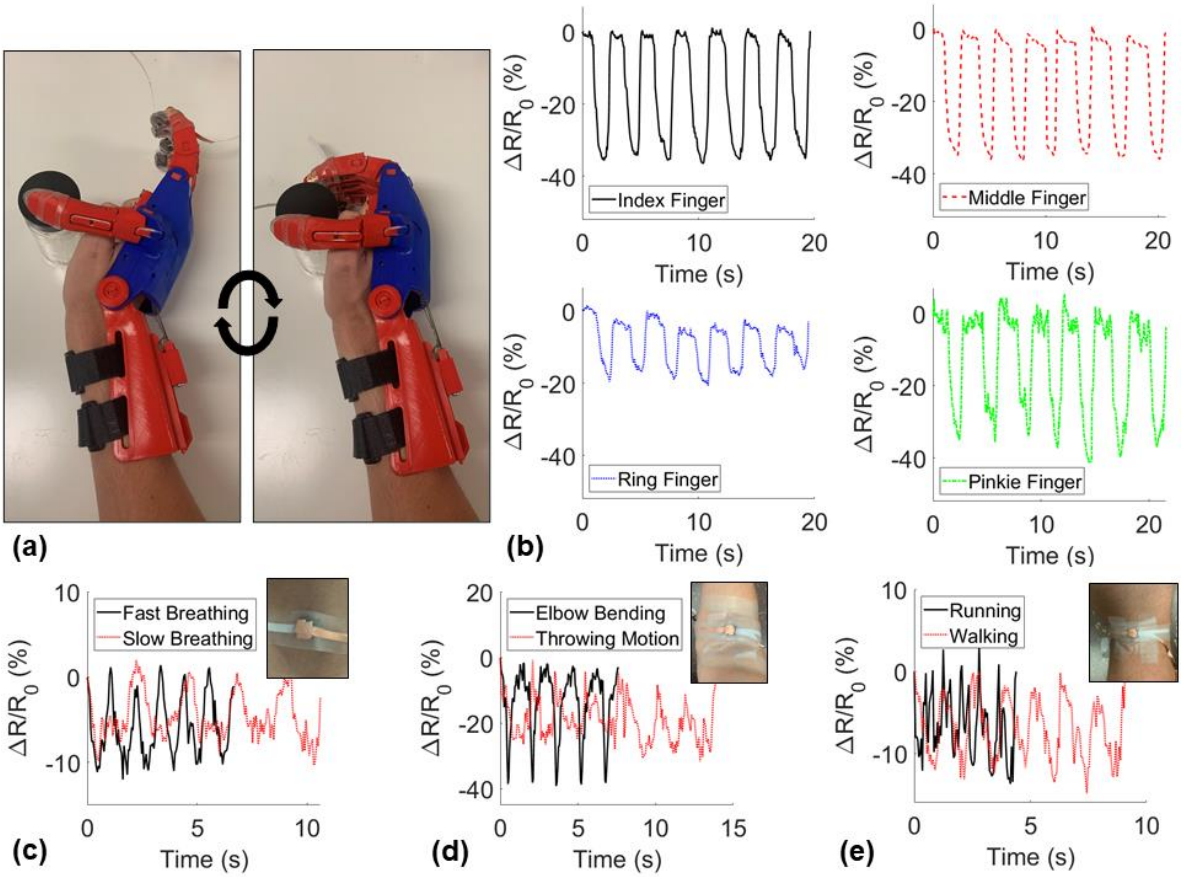

Figure 4.9: *Demonstration of applications of sponge sensors including (a, b) fingertip pressure detection on a prosthetic hand cyclically grabbing an object, and skin-attachable human motion detection on the (c) chest, (d) inside of the elbow, and (e) backside of the knee.*

The piezoresistive responses of the sponges attached to each finger of the prosthetic hand, seen in the pictures in Figure 4.9(a), are shown in Figure 4.9(b) where the minimum relative resistance measurements denoted grabbing an object and the maximum occurring after releasing the object. The sponges demonstrated consistent negative piezoresistive behavior during the stepwise sensing application. Next, the sponges were attached to the skin of a user on the chest, on the crease of the elbow, and behind the knee to detect normal human motions. An individual's breathing was measured before and after light exercise while the sensor was attached to the chest as shown in Figure 4.9(c). The sensor attached to the elbow as seen in Figure 4.9(d) was able to produce

distinctly different signals for different motions including a dynamic bending motion and a cyclic throwing motion. With the sensor attached behind the knee as seen in Figure 4.9(e), the sensor detected both running and walking motions. These demonstrations proved the potential for these nanocomposite sponge sensors to be used in a variety of motion-detecting applications. Lastly, a University of Oklahoma logo sponge, a gradient porosity sponge, and a triangular pyramid-shaped sponge were fabricated showing the diversity of sponge geometries able to be fabricated with the method used in this study (Figure A.8, Appendix A).

4.4 Conclusions

Piezoresistive sponges with tailorable electrical and mechanical properties were manufactured with a fabrication process that utilized a novel microwave-assisted rapid porogen removal method that significantly reduced the manufacturing time. The resistance and stiffness of the sponges were able to be varied by an order of magnitude by fabricating with various CNT loadings and sugar porogen amounts. The optimal CNT loading for the sensor was found to be 3 wt% to produce sponges with the highest conductivity and compressive piezoresistive sensitivity. The least porous sensor (CNT3P70) demonstrated the highest gauge factor (between 5 % - 50 % strain) of all the sponge sensors tested in this study. The highly sensitive lowest porosity sensor demonstrated higher piezoresistive consistency for a long-term cyclic durability test and a strain rate dependency test compared to the most porous sensor. The best sensor formulation was determined to be CNT3P70 and was demonstrated to be applicable as a skin-attachable sensor for dynamic human motion detection and stepwise sensing detection on a prosthetic hand.

CHAPTER 5: THE SORBENT-BASED OIL SKIMMER

5.1 Introduction

5.1.1 Motivation

It is well known that PDMS sponges display oil attracting (oleophilic) and water-repelling (hydrophobic) properties suitable for oil/water separation applications. During the previous study, it was observed that the nanocomposite prepolymer and porogen mixture behaved like sticky wet sand or could be explained as having a clay-like consistency. This unique consistency allowed the prepolymer mixture to be easily molded into various 3D shapes before curing. This moldability introduced the possibility to fabricate an oil sorbent in novel and advantageous shapes. The first idea was to make a sorbent with exceedingly high mass sorption capacity such that most of the sponge would be hollow by covering a large porogen with the prepolymer and porogen mixture before curing and removing the porogen. However, due to the buoyancy of the sponge on water, only a small portion of the hollow sponge was filled with oil when deployed in a simulated oil spill. Through these preliminary experiments, the sorbent-based oil skimmer (SOS) was designed by striving to better take advantage of the gravity-driven oil/water separation mechanism observed. The key to achieving this design was the ability to fabricate unique geometries of oil sorbent sponges with the prepolymer and porogen mixture. The nanofiller selected in this study was CB instead of CNTs for the low-cost and facile dispersion benefits. Notably, the semiconductive samples were able to be microwave-cured showing the potential to rapidly fabricate the sorbent in the SOS. Additionally, oil spill cleanup has always interested me for the potential positive impact

innovations in this field may have on our environment. There have not been enough noteworthy solutions to the oil spill cleanup problem. To this day, alarming amounts of solid waste from single-use sorbents are produced during oil spill cleanup scenarios. Reusable sorbent-based devices like the SOS may provide a solution to this crisis and may help progress our oil spill cleanup capabilities.

5.1.2 Background

In this study, for the first time, a floating vessel-type oil collector capable of continuous oil extraction from the water surface was developed. The novel SOS was created and tested to demonstrate continuous oil extraction from water, facile deployment, and high reusability. The gravity-driven oil/water separation mechanism of the novel oil skimmer required no energy input. The material properties of the nanocomposite sponges with varying porosities and CB loadings (Table A.2, Appendix A) were investigated including Joule heating, durability, hydrophobicity, and oleophilic properties. The reusability of the SOS was tested, various sponge funnel sheet designs were explored, and the ability of the SOS to extract different types of oil from fish tank-scale oil spill simulations was demonstrated.

5.2 Experimental Methods

5.2.1 Materials

Sylgard 184 PDMS was obtained from Dow Corning. Salt, gasoline, and diesel fuel were acquired from Walmart. Motor oil (30W-50) and polylactic acid (PLA) filament was purchased from Amazon. The EPON 862 epoxy, CB, Epikure 9553 curing agent, ethanol, THF, chloroform, acetone, silicone oil, and pump oil were bought from Sigma-Aldrich.

5.2.2 Sponge Fabrication

First, PDMS Part A and Part B (10:1) were mixed with CB via centrifugal mixing to create a nanocomposite prepolymer (PDMS/CB). The PDMS/CB was hand-mixed with salt to create a homogenous mixture (PCS). The PCS with various salt and CB loadings (Table A.2, Appendix A) was molded with 3D printed templates (Figure A.9, Appendix A) into small (1x1x1 cm) and large (5x5x5 cm) cubes. The samples were cured, submerged in water to remove the salt porogen, cleaned with ethanol, and dried.

5.2.3 Characterization

A light microscope was used to image waterdrop contact angle tests and Joule heating motor oil absorption experiments by depositing a droplet (~10 μL) onto a sponge. A Zeiss Neon EsB SEM was used to image the surface of the various sponges. Sponge cubes were placed in various oils and organic solvents and measured and weighed before and after absorption. The mass sorption capacity (C) was calculated following Equation (5.1)

$$C = \frac{(M - m)}{m} \tag{5.1}$$

where M is the weight of the sponge after oil absorption and m is the dry weight of the sponge. The swelling ratio (S) was calculated with Equation (5.2)

$$S = \frac{V}{v} \tag{5.2}$$

where V is the volume of the sponge after oil sorption and v is the volume of the dry sponge. All mechanical compression tests were performed on an Instron 3345 single column mechanical

testing machine. A Brookfield DV-II+ Viscometer was used to measure the viscosity of the motor oil at various temperatures. Silver epoxy and copper tape were applied on sponges as electrodes for Joule heating experiments measured with a Fluke 54 II Digital Thermometer and to measure the resistances of the small sponges with a Hioki RM3545-02 Resistance Meter (Figure A.10, Appendix A).

5.2.4 SOS Construction

The SOS prototype vessel was 3D printed in PLA and coated with several layers of epoxy. High-density polyethylene (HDPE) lid extensions were bolted onto the vessel. The sponge funnel was fabricated using 3D printed templates. First, a 1 cm thick circular sheet was formed by pressing the uncured PCS into a 3D printed template and the vent hole was cut out of the center of the sheet. A large extended cone-shaped salt porogen was fabricated by mixing salt with water, molding, and microwaving to harden (Figure A.11, Appendix A). The porogen was placed on the PCS sheet over the top of a large hole in the center and covered with PCS leaving a small 5 cm diameter hole at the tip of the large cone-shaped porogen. The sponge funnel was cured and placed in water to remove the salt porogen, cleaned with ethanol, and dried. To assemble the SOS, the sponge funnel was placed into the vessel and the lid and vent component was placed on top with the vent through the vent hole on the sponge funnel. The top HDPE sheet was placed on top of the lid and tied to the HDPE sheets bolted onto the vessel on both ends. Rope handles were added to facilitate SOS deployment and oil tubing was connected underneath the vessel.

5.2.5 SOS Testing

The SOS prototype with a CB15P9 sponge funnel was deployed in several 30 mm thick simulated oil spills to measure the oil extraction rate at each oil layer thickness. The sponge funnel designs tested (sheet thicknesses = 1 cm): (i) small-diameter circular sponge sheet (diameter = 21 cm), (ii)

large-diameter circular sponge sheet (diameter = 31 cm), and (iii) large-diameter flower-shaped sponge sheet (diameter = 31 cm; 60 pedals). The reusability of a sponge funnel with a small sponge sheet was determined by repeating simulated gasoline spill extraction tests with relevant sponge funnel reuse conditions. Lastly, the SOS with the large-diameter sponge sheet was tested in a diesel fuel and crude oil simulated oil spill.

5.3 Results and Discussion

5.3.1 SOS Inspiration, Design, and Functionality

The continuous oil extraction capabilities of the SOS were enabled by three key features: (i) the sponge funnel geometry, (ii) the oil sorbent material properties, and (iii) the vessel. The SOS design was conceptualized after preliminary experiments focused on scaling up PDMS sponges that have been limited to small-scale experiments largely due to the fabrication methods widely used including the sugar cube templating method, first shown by Choi et al. [176]. In this study, PCS was used to fabricate sorbent sponges that allowed for facile molding of several complex geometries. The PCS was used to encase a large spherical salt porogen to create a hollow sponge or shell structure (Figure A.12, Appendix A). During deployment of the spherical sponge shell in a small-scale simulated oil spill, the inner core of the shell structure below the oil layer filled with oil due to gravity (Figure A.13, Appendix A). Next, a pump was connected underneath the spherical sponge shell to extract the oil from the hollow sorbent (Figure A.14, Appendix A). While this approach was novel, the sponge shell collapsed during extraction, demonstrated a slow absorption rate due to a small surface area of sorbent in contact with the thin oil layer, and struggled to maintain vertical alignment. To solve these issues, the sponge funnel was designed and fabricated to include a hollow funnel-shaped sponge shell connected to a large sponge sheet with

a vent hole for high surface area contact with the oil layer (Figure A.15, Appendix A). A vessel was incorporated with the sponge funnel to maintain vertical alignment and encase the separated oil. This design enabled rapid oil extraction with a peristaltic pump connected to the vessel underneath the sponge funnel.

The SOS prototype design used in this study included only counterweights, however, a ballast tank may be implemented to control the buoyancy of the device (Figure A.16, Appendix A). The SOS prototype design, shown in Figure 5.1(a), utilized lid extensions due to the limited build volume of the 3D printer used to fabricate the vessel and to account for the expansion of the sponge funnel during oil absorption. The lid was tied down securely as seen in Figure 5.1(b) to create a leakproof seal between the oil sorbent and vessel. No water could leak into the vessel with a sufficiently hydrophobic sponge funnel during oil extraction tests shown in Figure 5.1(c). The gravity-driven oil/water separation mechanism of the novel oil skimmer illustrated in Figure 5.1(d) required no energy input. This design may allow for an array of SOS devices connected to one peristaltic pump for highly energy-efficient and rapid extraction of large-scale oil spills as seen in Figure 5.1(e).

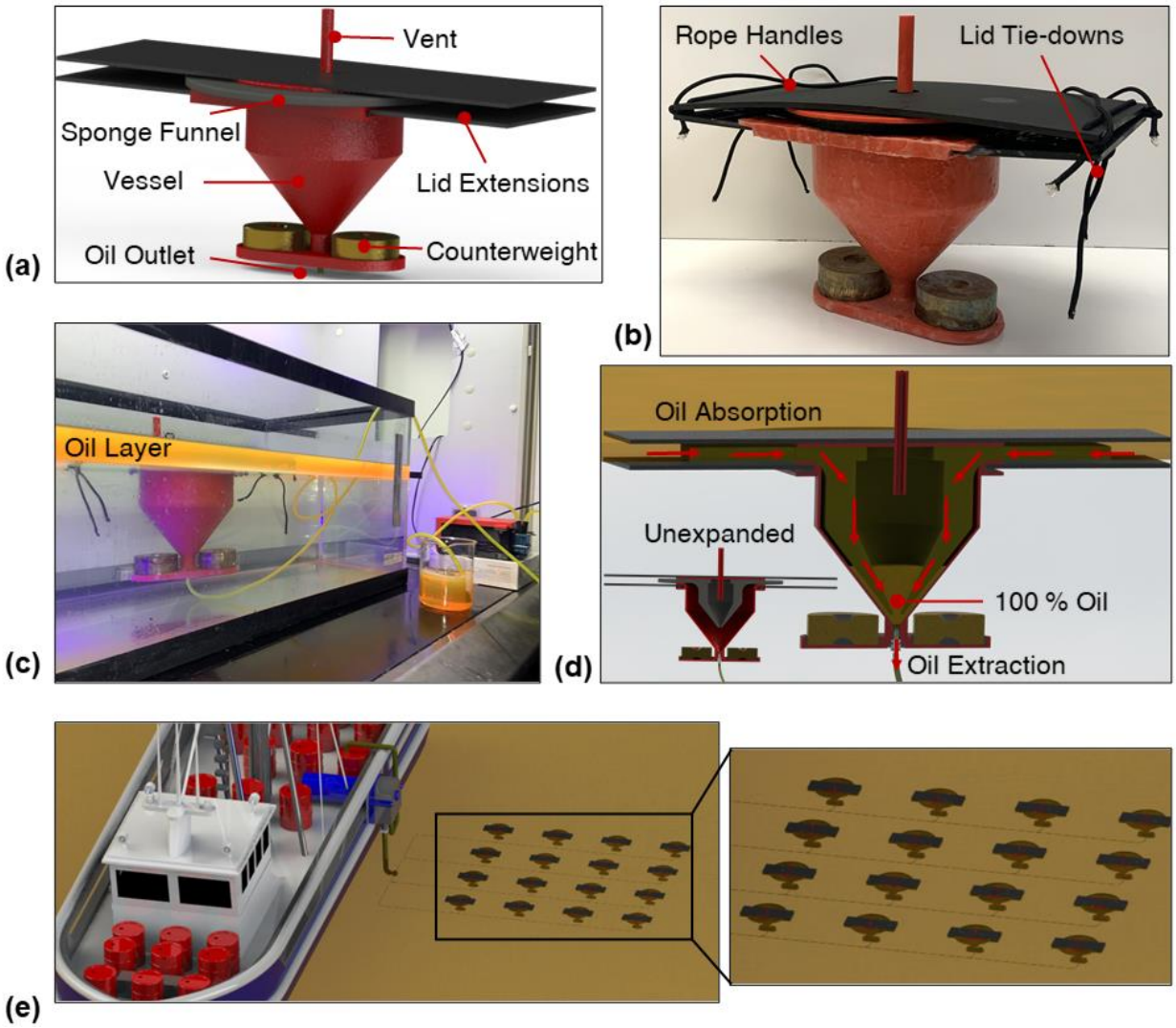

Figure 5.1: *(a) The SOS design, pictures of (b) the fully constructed SOS prototype and (c) the SOS continuously extracting gasoline from the water surface, (d) a schematic of gravity-driven oil extraction functionality of the SOS, and (e) a conceptual image of an SOS array connected to one peristaltic pump.*

5.3.2 Development and Characterization of Sorbent Material

The PCS mixture was used to fabricate sponge cubes consisting of CB dispersed within a PDMS matrix for material characterization. Several studies in the field attached nanoparticles to the surface of highly porous sponges to impart superhydrophobic or multifunctional properties like magnetism [177-179]. However, van der Waals forces between nanofillers and PDMS are

relatively weak [180], and dip-coating and other nanoparticle attachment methods were deemed difficult to implement on the large-scale sponge funnel, therefore it was not explored in this study. Nanoparticle detachment and wash out would lead to a decrease in sorbent material properties over time [181], and would contaminate the aquatic environment and extracted oil. Therefore, the nanofiller was dispersed within the polymer matrix to minimize the potential for nanoparticle detachment in this study. The desired traits for a sorbent material used in the SOS: (i) facile fabrication of large-scale funnel-shaped geometries, (ii) rapid oil absorption (oleophilic), (iii) high water contact angle (hydrophobic), (iv) durability and reusability, and (v) Joule heating capabilities for highly viscous oil absorption. The PCS mixture with various salt porogen:PDMS/CB prepolymer ratios and CB loadings were used to fabricate small and large sponge cubes for detailed material characterization to determine the optimal nanocomposite sorbent formulation for use in the SOS. First, the porosities of each sponge cube fabricated in this study were measured and the results can be seen in Figure 5.2(a) and Figure 5.2(b). As expected, a larger amount of salt porogen in the PCS mixture increased the porosity of the sponge fabricated from 76.7±0.4 % for CB15P4 up to 89.3±0.3 % for CB15P9. Sponges with varying CB loadings did not have a significant difference in the porosity. However, SEM images are shown in Figure 5.2(d) – Figure 5.2(k) and revealed that varying CB loadings did have a noticeable effect on the microstructure of the nanocomposite sponges.

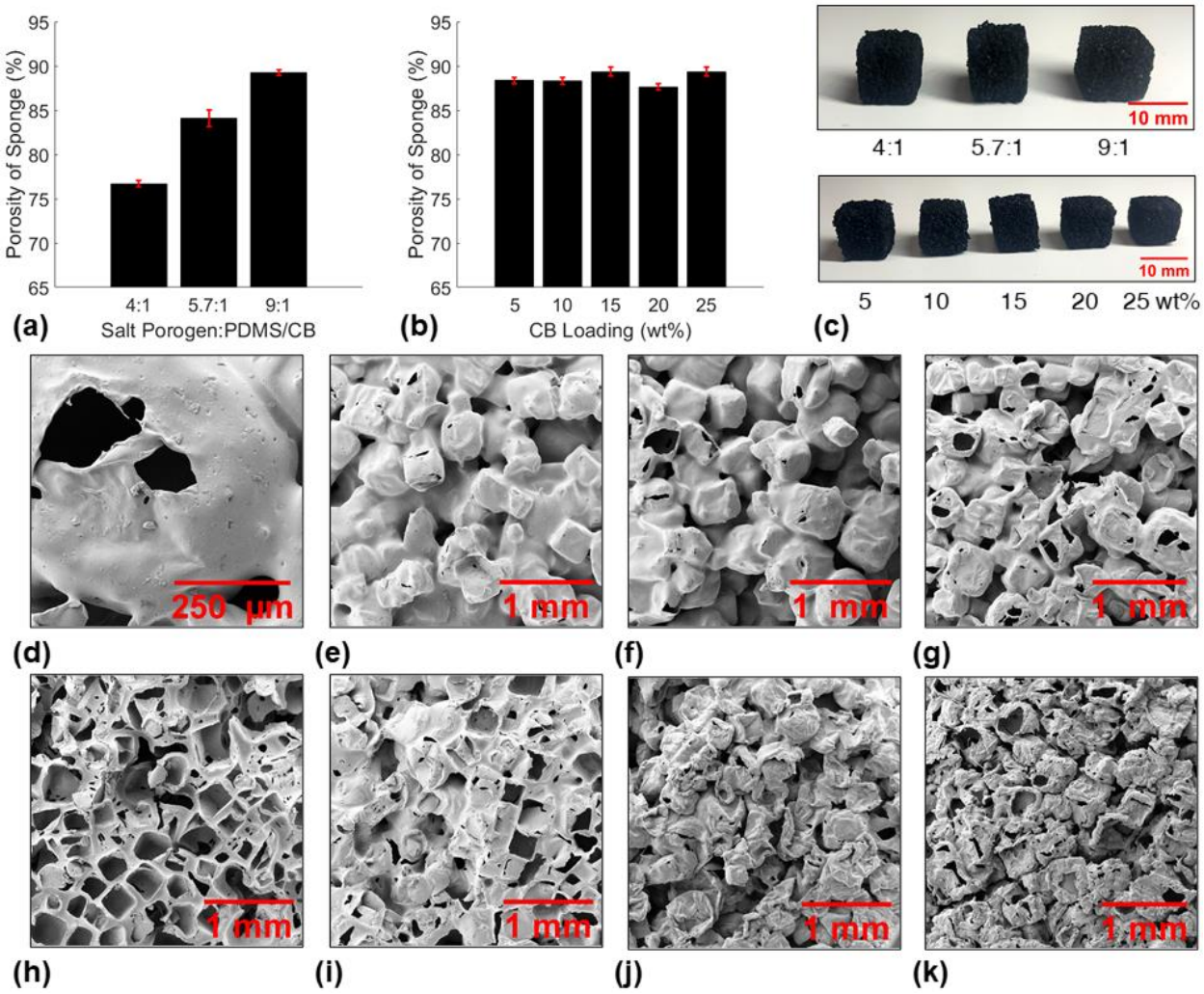

Figure 5.2: *Porosities of sponges fabricated with varying (a) salt porogen:PDMS/CB prepolymer ratios and (b) CB loadings. (c) Pictures of the small sponge cubes fabricated for sorbent material characterization (top: CB15P4, CB15P6, and CB15P9; bottom: CB5P9, CB10P9, CB15P9, CB20P9, and CB25P9). SEM images of (d) pores in a CB5P9 sponge and the microstructures of (e) CB15P4, (f) CB15P6, (g) CB15P9, (h) CB5P9, (i) CB10P9, (j) CB20P9, and (k) CB25P9 sponges.*

Next, the oleophilic properties and reusability of the fabricated sponges were characterized. The small CB15P9 sponge cubes were deployed in various oils and organic solvents at room temperature and allowed to fully sorb as seen in Figure 5.3(a). The mass sorption capacities of the sorbent material are shown in Figure 5.3(b), demonstrating the capability of absorbing a wide range of oils and organic solvents. Notably, Figure 5.3(b) shows both uncompressed sorption

capacities and compressed sorption capacities which designate if the sponge was mechanically compressed while submerged to expel air bubbles that can become trapped during sorption. The trapped air may affect the oil flow rate through the sponge and consequently the extraction rate of the SOS. The mass sorption capacities and swelling ratios of the varying porosity small sponges deployed in gasoline are shown in Figure 5.3(c) and Figure 5.3(d), respectively. The mass sorption capacities were greater for higher porosity sponges which agreed with similar studies in the field [182-184]. The absorption rates of the varying porosity large sponge cubes were compared by incrementally measuring the mass sorption capacities during 15 min of gasoline absorption and the results are displayed in Figure 5.3(e). The results showed that higher porosity sponges absorbed oil considerably more rapidly than lower porosity sponges. The highest porosity sponge (CB15P9) was found to fully sorb with gasoline in under 1 min, while the lowest porosity sponge (CB15P4) required over 12 min to fully sorb. Therefore, PCS with the highest ratio (9:1) of salt porogen:PDMS/CB prepolymer was selected to fabricate sponges with varying CB loadings for the durability and reusability investigation.

A critical application of the SOS would be to replace single-use sorbent materials that are widely used in the oil spill cleanup industry that results in massive solid waste. To reduce or eliminate this waste, the sorbent material used in the SOS must be highly reusable. Herein, the durability and reusability of the nanocomposite sponges used in this study were investigated for 10 cycles of gasoline absorption, cleaning in ethanol, and drying in a vacuum oven. The average dry masses of the sponges before gasoline sorption, mass sorption capacities, and swelling ratios for sponges with various CB loadings between 5 – 25 wt% are shown in Figure 5.3(f) – Figure 5.3(h).

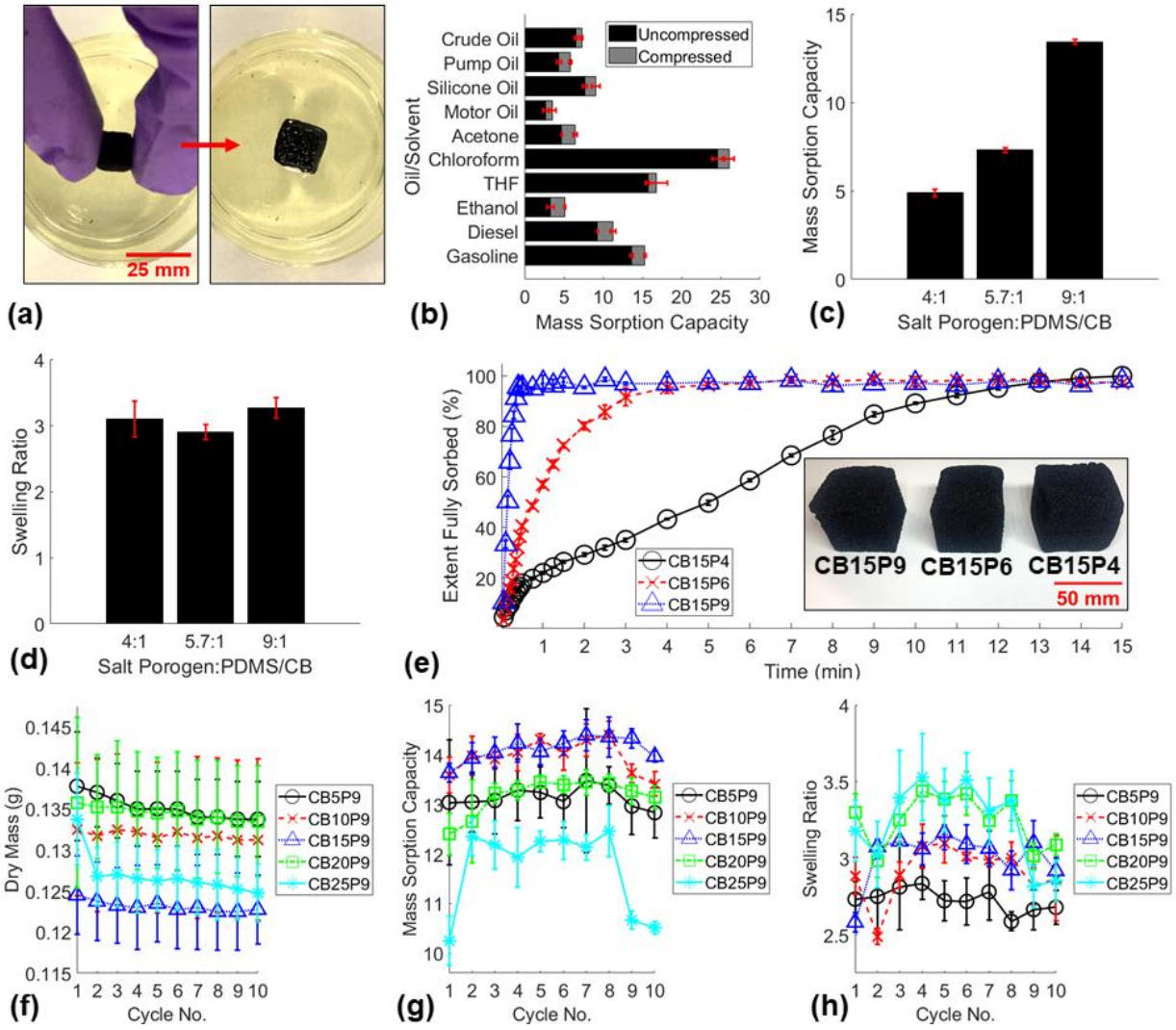

Figure 5.3: *(a) Pictures of uncompressed gasoline sorption test before and after deploying a small CB15P9 sponge (mass sorption capacity = 13.6; swelling ratio = 3.3). (b) Mass sorption capacities of CB15P9 small sponges of various oils and organic solvents. (c) Mass sorption capacities, (d) swelling ratios, and (e) absorption rate comparison of varying porosity sponges. Durability study of the most porous sponges with varying CB loadings including 10 cycles of (f) masses of dried sponges, (g) mass sorption capacities, (h) swelling ratios.*

A significant loss of mass was observed in CB5P9 sponges due to the lack of mechanical reinforcement in the polymer leading to significant damage, and the first cycle of CB25P9 sponges possibly due to nanoparticle detachment from inadequate mixing of the high CB loading in the polymer matrix. After several cycles, noticeable damage was observed within the CB5P9,

CB10P9, and CB25P9 sponges, while the CB15P9 and CB20P9 sponges remained entirely intact. Mechanical compression tests before and after 10 cycles of gasoline absorption and SEM images confirmed the apparent damage or lack of damage to the sponges (Figure A.17, Appendix A).

The hydrophobic properties of the sponges were investigated via the water contact angle test. The water contact angles comparison for the varying porosity sponges, varying CB loading sponges, and Joule heating voltages applied to a small CB20P9 sponge are shown in Figure 5.4 and representative images are displayed in Figure A.18 (Appendix A). Higher porosity sponges demonstrated higher hydrophobicity with larger water contact angles which agreed with multiple studies in the field [182, 185]. In contrast, CB loading did not influence the hydrophobic properties of the materials, which did not align with similar studies in the field that coat the surface of PDMS sponges with carbonaceous nanoparticles [186, 187]. This finding and the SEM images of the nanostructure of the sponge surface (Figure A.19, Appendix A) both confirmed that the CB is embedded within the polymer matrix. Lastly, the water contact angles for a CB20P9 sponge with various Joule heating voltages applied were confirmed to not affect the hydrophobicity of the sponge. Therefore, Joule heating may be implemented on the sponge without compromising the vital hydrophobic behavior of the sorbent.

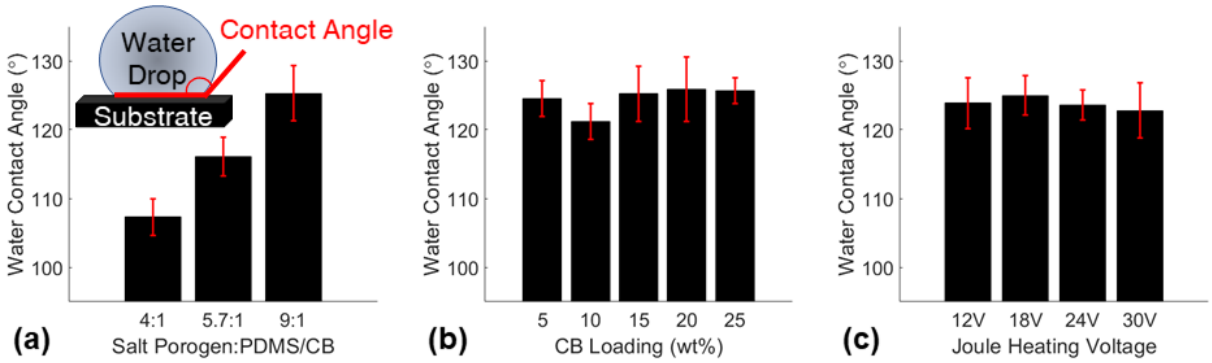

Figure 5.4: *Water contact angles for (a) varying porosity sponges, (b) varying CB loading sponges, and (c) various Joule heating voltages applied to small CB20P9 sponges.*

5.3.3 Sponge Joule Heating for Viscous Oil Absorption

Highly viscous oil spills are exceedingly difficult to remove from water with sorbent materials as sorbents typically require a low viscosity fluid to readily absorb through the microstructure of the material. Many researchers have recently investigated the heating capabilities of nanocomposite sorbent materials via simulated sunlight (photothermal effect) [188] and Joule heating [189] to increase the local temperature and reduce the viscosity to rapidly absorb the nearby oil. The measured viscosities of the most viscous oil obtained, motor oil, are exhibited in Figure 5.5(a) to confirm the expected decrease in viscosity as the oil temperature increased. Joule heating functionality was enabled when a sufficient CB loading was dispersed within the polymer matrix.

The semiconductive behaviors of the nanocomposite sponges with varying CB loadings used in this study were characterized by measuring the resistances of the small sponges and the results can be seen in Figure 5.5(b). The sponges with CB loadings between 5 wt% - 15 wt% did not demonstrate Joule heating functionality for the voltages investigated. Also, CB25P9 sponges proved difficult to scale up due to the inadequate hand-mixing process of the highly viscous nanocomposite prepolymer with the salt porogen (Figure A.20, Appendix A). Therefore, CB20P9

sponges were selected as the ideal nanocomposite sorbent material formulation to explore Joule heating capabilities.

The mass sorption capacities of the small CB20P9 sponges for motor oil at various temperatures are shown in Figure 5.5(c) to verify the sorbent absorbed the oil more readily at higher temperatures. The pictures shown in Figure 5.5(d) summarize a microscopy experiment that was conducted with no voltage applied and 30 V applied to a small CB20P9 sponge to compare the time required for the full absorption of a motor oil droplet. The experiment proved that Joule heating offered over an order of magnitude improvement in the time required to absorb the viscous motor oil droplet if the sponge was Joule heated to temperatures near 100 ℃ (Figure A.20, Appendix A). A large CB20P9 sponge seen in the picture in Figure 5.5(e) was Joule heated with various voltages to investigate the heating rate of larger sorbents. Higher voltages resulted in faster heating rates and higher maximum sorbent temperatures that reached 38 ℃, 71 ℃, 98 ℃, 117 ℃, and 127 ℃ for 12 V, 24 V, 36 V, 48 V, and 60 V, respectively. The longevity of the Joule heating functionality was investigated for reusability by Joule heating the sponge for 50 cycles shown in Figure 5.5(f), and endurance by continuously heating the sponge for 12 h, as seen in Figure 5.5(g). The maximum and minimum temperatures over 50 cycles remained consistent at 111±2 ℃ and 22.1±0.5 ℃ respectively which demonstrated the essential reusability of the Joule heating functionality. Additionally, the endurance experiment proved the sorbent can maintain a steady temperature of 112±3.2 ℃ over 12 h of constant Joule heating. These experiments proved the ability of the nanocomposite sorbent material used in the SOS to be Joule heated for consistent and reliable rapid absorption of viscous oils. While Joule heating the sponge funnel in the SOS was not within the scope of this study, this sorbent heating functionality may be utilized on the SOS for continuous extraction of highly viscous oils from water.

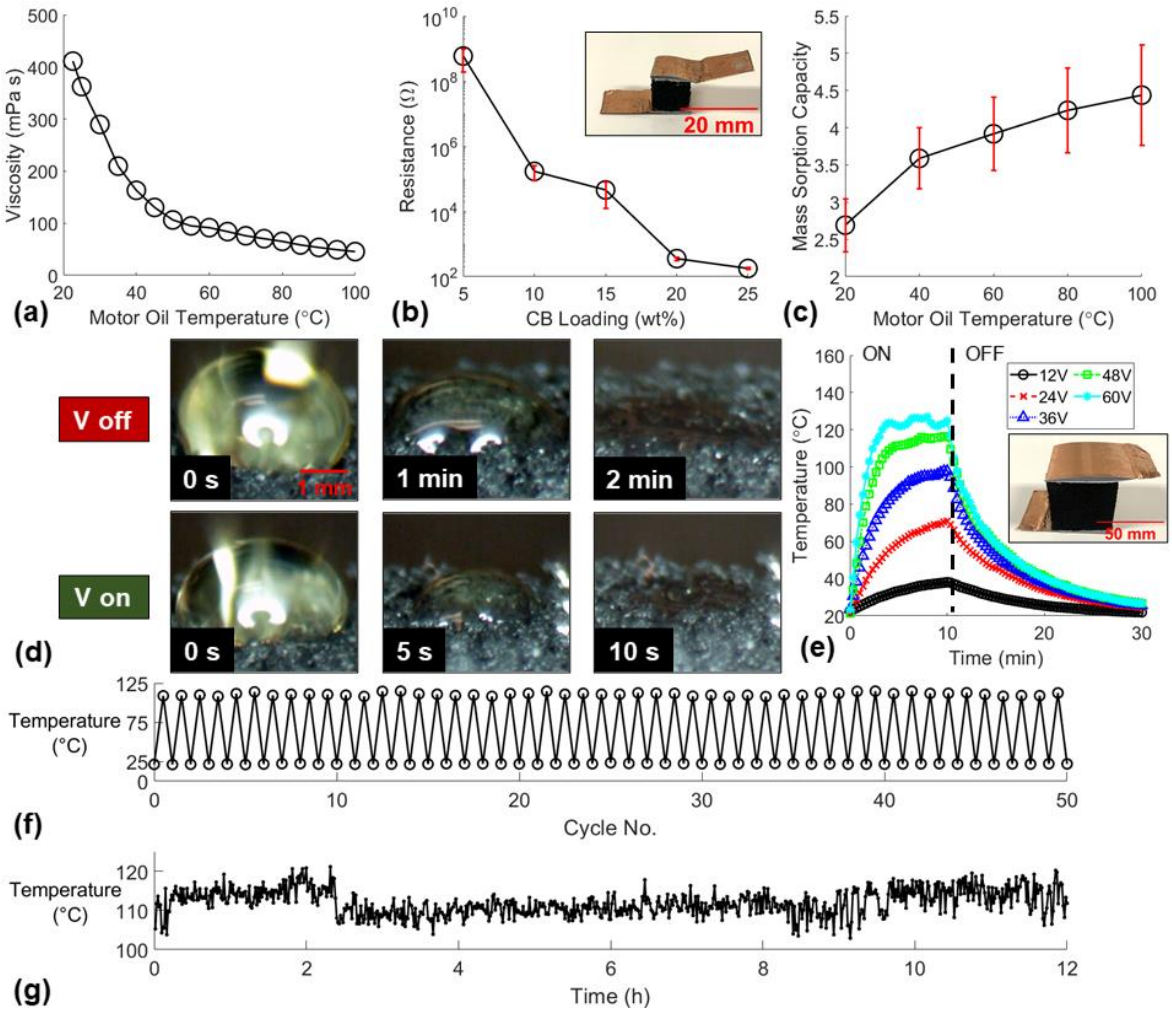

Figure 5.5: *(a) Motor oil change in viscosity due to change in oil temperature. (b) Resistances of small sponges with varying CB loadings (CB5P9, CB10P9, CB15P9, CB20P9, and CB25P9). (c) Mass sorption capacities of small CB20P9 sponges due to motor oil temperature change. (d) Microscopy images demonstrating a CB20P9 sponge rapidly absorbing viscous motor oil due to Joule heating. (e) Joule heating temperatures of a large CB20P9 sponge at various applied voltages. Joule heating durability study including (f) 50 cycles of maximum and minimum temperatures and (g) 12 h of continuous 30 V applied to a small CB20P9 sponge.*

5.3.4 Oil Spill Cleanup Demonstrations

After characterizing the oleophilic, hydrophobic, durability, reusability, and Joule heating properties of the nanocomposite sponge, it was necessary to test the viability of the material to

absorb oil spilled in water. First, a sheet of nanocomposite sponge was deployed in a small-scale simulated gasoline spill in water and the experiment is displayed as time-based pictures in Figure 5.6. The sponge rapidly expanded and absorbed the small oil spill in seconds and was easily removed. This experiment demonstrated the oil/water separation capabilities of the sponge material. Many studies in this field demonstrated similar small-scale oil/water separation capabilities of their sorbent material [190-193]. However, very few explore solutions to scale up this technology beyond this experiment, a step that is vital to real-world oil spill cleanup applications.

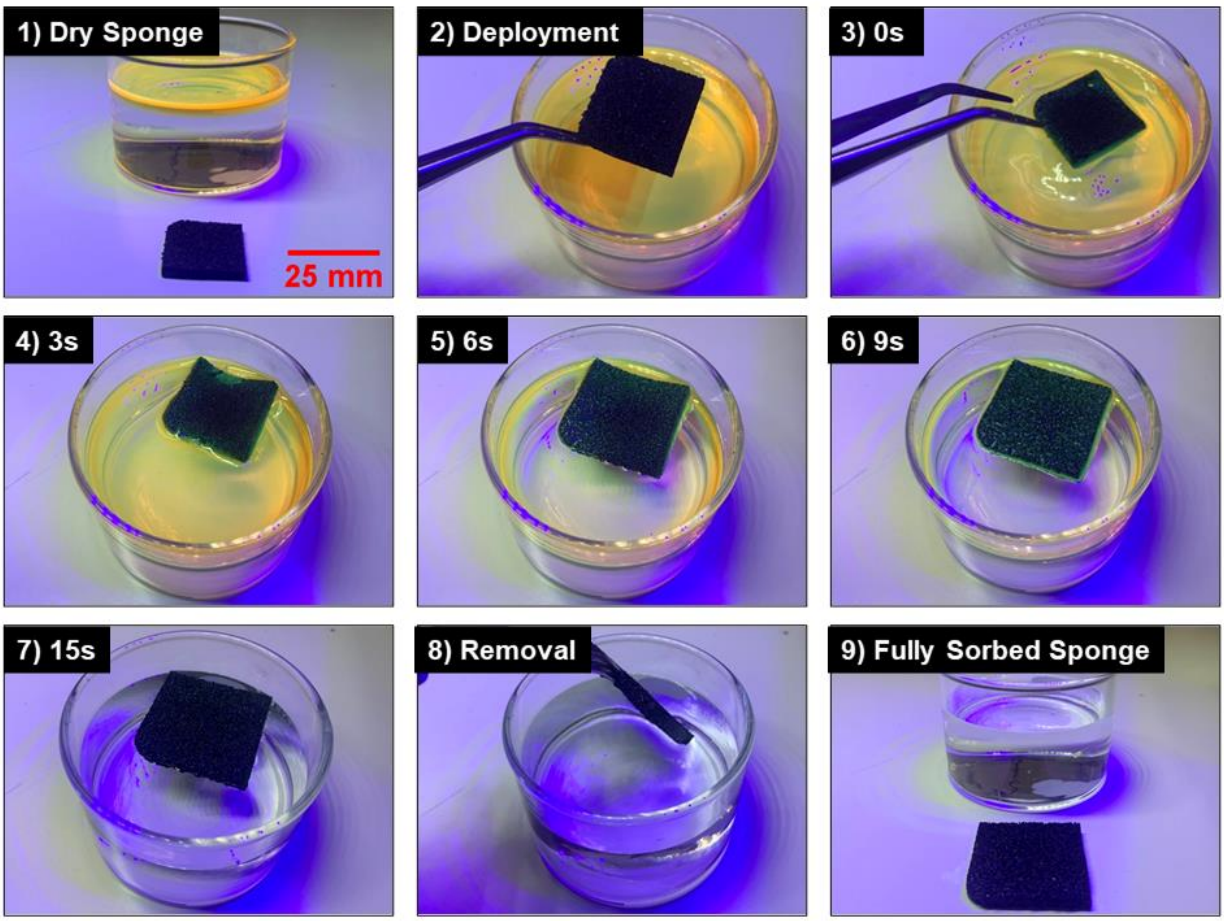

Figure 5.6: *Time-based pictures demonstrating the oil/water separation capability of a CB15P9 sponge.*

Pictures demonstrating the sponge funnel functionality are shown in Figure 5.7 to visualize the gravity-driven oil/water separation mechanism. A transparent vessel was submerged in a simulated gasoline spill in water such that the oil layer height was near the level of the top rim of the clear vessel. The sponge funnel, SOS lid and vent component, and a small weight were deployed on the clear vessel. The sponge funnel rapidly expanded while absorbing gasoline, and in about 5 min the sponge funnel was sorbed and began releasing gasoline from the hollow core of the sponge into the clear vessel in a steady and constant stream (Figure A.21, Appendix A). This process continued for about 30 min until the entire oil spill was separated from the water surface into the vessel. Notably, the oil layer was just below the brim of the vessel to begin the experiment. Therefore, the sorbent material demonstrated the ability to pull the gasoline through the microstructure of the sponge and above the brim of the vessel via capillary action, owing to the impressive oleophilic properties of the sponge material. This visually proved the oil/water separation mechanism of the sponge funnel deployed in a vertically aligned vessel, demonstrating the feasibility of the SOS design.

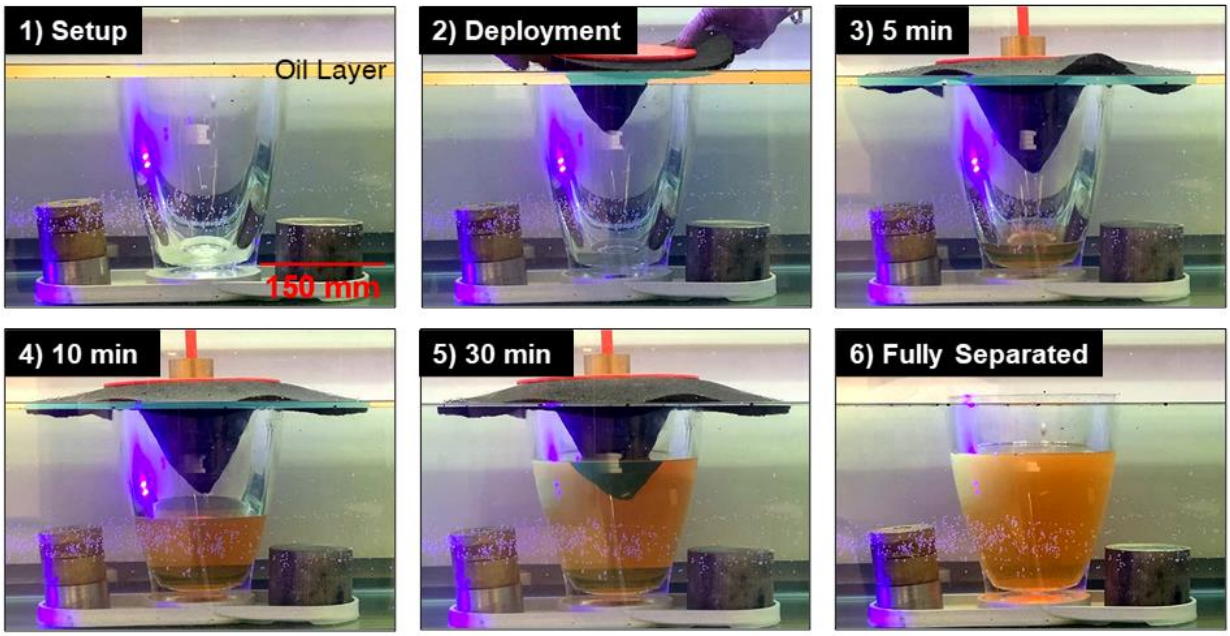

Figure 5.7: *Time-based pictures of a sponge funnel demonstrating gravity-driven oil/water separation to absorb oil from the water surface and fill a vessel.*

Lastly, Figure 5.8(a) depicts the fully assembled floating SOS system deployed in simulated oil spills of 3 gallons of gasoline to determine the extraction rate at various oil layer thicknesses. The SOS was easily deployed via rope handles into the oil spill, the peristaltic pump connected underneath the floating vessel was turned on, and continuous oil extraction began within 5 min. In under 90 min, the SOS had extracted the 30 mm thick oil spill from the water. Notably, no water was observed in the extracted oil. This observation indicated that the SOS likely demonstrated an oil recovery efficiency (volume ratio of oil removed to the total fluid removed) near 100 %. This apparent water-free oil extraction capability is remarkable and unique to the SOS as a vast majority of traditional oil skimmers report a significantly lower recovery efficiency [194]. The following experiments were aimed at testing the extraction rate of the SOS at different sponge funnel reuse conditions, various designs of the sponge funnel, and for various types of oil spilled on water.

The SOS containing the small diameter sheet sponge funnel was tested at various reuse conditions and the extraction rates and efficiencies at each oil layer thickness are shown in Figure 5.8(b). Each test demonstrated the maximum extraction rate at the thickest oil layer (30 mm) likely due to gravity increasing the rate of absorption on the top surface of the sponge sheet submerged in the thick oil layer. As the oil layer became thinner during extraction, the SOS progressively decreased in oil extraction rate and efficiency, as this is a common issue faced by oil skimmers [124]. This was likely attributable to the reduction of gravitational influence and sponge surface area in contact with the thin oil layer. The first test and the thoroughly cleaned and dried sponge funnel demonstrated the highest efficiency and extraction rate throughout the tests which demonstrated the reusability of the entire SOS system. When the sponge funnel had not been adequately cleaned with ethanol and dried completely, the extraction efficiency decreased noticeably. For each reuse condition investigated, the sponge funnel had undergone previous expansion of the polymer such that significant air pockets formed within the microstructure of the sponge when removed from the oil spill and exposed to the atmosphere. The three mechanisms that formed these air pockets in the sponge funnel: (i) evaporation, (ii) gravity-driven oil separation from the sponge funnel, or (iii) compression and paper towel absorption. The mass sorption capacities of the large CB15P9 sponges were measured at each of the reuse conditions tested. The results showed that the general trend of the mass sorption capacities matched the extraction rate trend for the various sponge reuse conditions (Figure A.22, Appendix A). Therefore, when more air pockets were trapped within the sponge funnel (lower mass sorption capacity) there was a significant loss in flow rate through the microstructure of the sponge that reduced the SOS extraction rate.

The purpose of the sponge sheet in the sponge funnel design was to introduce a sorbent with a high surface area in contact with the spilled oil for rapid extraction. To explore the potential of

increasing the surface area of the sponge sheet to increase the extraction rate, a sponge funnel with a larger diameter, and one with a flower-shaped design were fabricated and tested. The results in Figure 5.8(c) show that the larger the surface area of the circular sponge sheet demonstrated a faster extraction rate than the smaller circular sponge sheet sponge funnel. Surprisingly, the flower-shaped design displayed the slowest oil extraction rate despite having the largest total surface area in contact with the oil layer. This was likely due to a significant reduction in gravitational influence as the flower-shaped sponge sheet floated on the oil layer more readily and the top surface area in contact with the oil was reduced with this design. However, the flower-shaped sponge funnel retained its extraction efficiency for very thin oil layers compared to the circular sheets likely due to increased surface area in contact with the thin oil sheens. Lastly, the results of the large-diameter circular sponge funnel tested in higher viscosity diesel fuel and crude oil simulated spills are displayed in Figure 5.8(d). While the SOS was able to continuously extract the higher viscosity oils, the extraction rate was significantly reduced showing the potential to improve the SOS design by incorporating sorbent Joule heating.

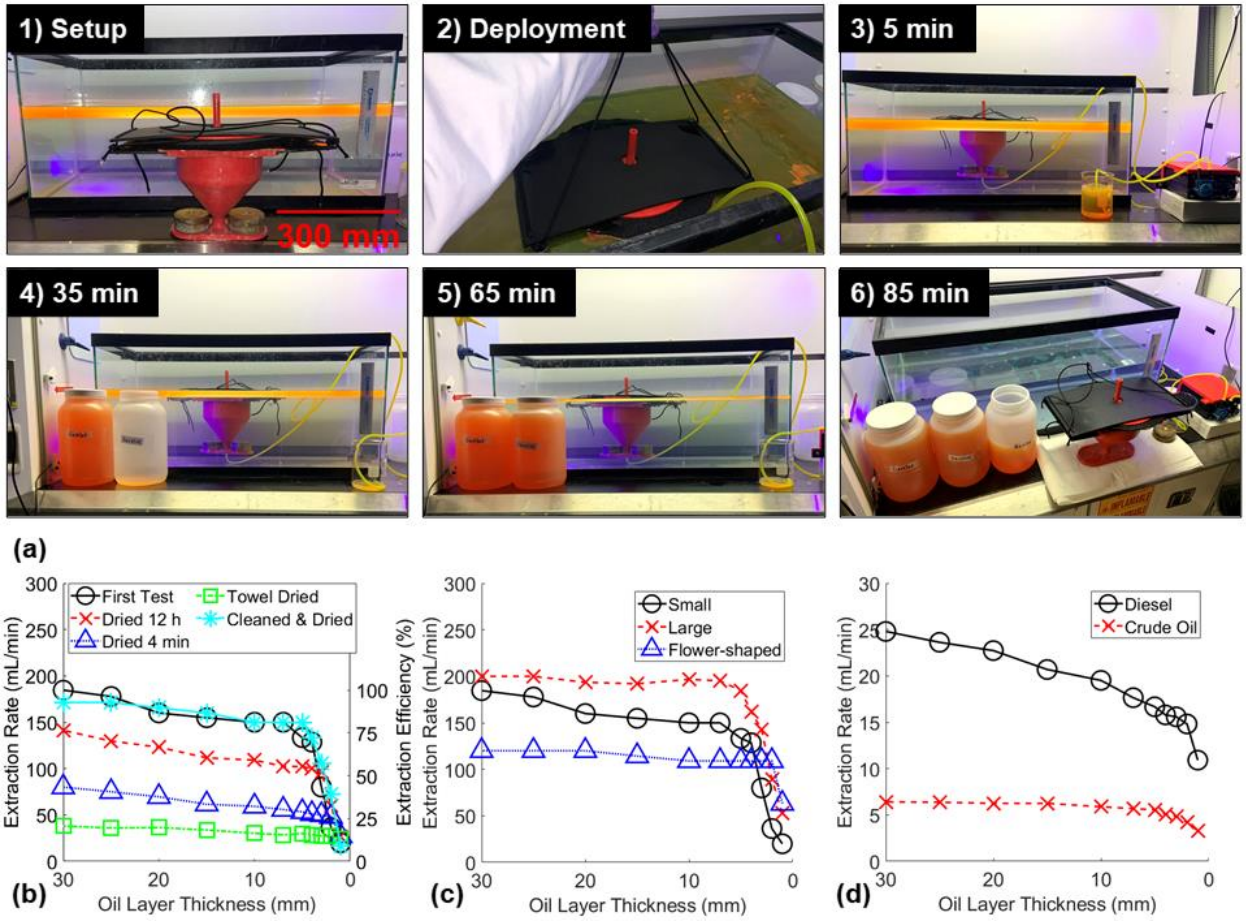

Figure 5.8: *(a) Time-based pictures of the SOS continuous extraction of oil from water, (b) the SOS extraction rate for gasoline at various layer thicknesses for various sorbent reuse conditions and (c) for varying sponge funnel designs, and (d) the SOS extraction rate of diesel fuel and crude oil at various oil layer thicknesses.*

5.4 Conclusions

In conclusion, a novel energy-efficient oil skimmer was developed and tested. For the first time, a highly reusable, floating vessel-type oil collecting device was constructed with continuous oil extraction capabilities. The parameters of the facile sorbent fabrication method including the amount of porogen and CB loadings were investigated to determine the ideal nanocomposite sponge formulations. The desired characteristics of the sponge included a rapid oil absorption rate, sufficient hydrophobicity, durability for reuse, and Joule heating for viscous oil absorption. The

ideal sponge types for use in the SOS were determined to be CB15P9 for low viscosity oil spills, and CB20P9 to incorporate Joule heating functionality for viscous oil absorption. The SOS device demonstrated great reusability, a high oil extraction rate, and the ability to extract multiple types of oils. The SOS is a promising new oil spill cleanup technology that may help solve the problem of massive amounts of solid waste produced by single-use sorbents during oil spill cleanup, in addition to other applicable large-scale oil skimming applications.

CHAPTER 6: CONCLUSIONS AND FUTURE WORK

6.1 Conclusions

6.1.1 Microwave-curing CNT Nanocomposites

The most noteworthy benefit of microwave-curing PDMS/CNT nanocomposites is the ability to reduce the curing time by at least 96 %. Notably, as CNT loading increases, the time required to thermally-cure the material in an oven increases drastically. With the microwave-curing method, the curing time decreases noticeably as CNT loading increases, with conductivity being the most relevant consideration for the rate of microwave heating and curing. This finding may prove highly advantageous to future researchers and engineers in the field to consider microwave-curing as a viable rapid fabrication technique. This work found that microwave-curing CNT-based nanocomposite elastomers increased the electrical conductivity, lowered the compressive modulus, and unaffected the compressive piezoresistive sensitivity of the material. Improved nanofiller dispersion and likely CNT alignment in the microwave-cured nanocomposites likely explained the drastic increase in electrical conductivity.

6.1.2 Flexible Sensors for Human Motion Detection

In this work, highly versatile piezoresistive sensors were developed for skin-attachable human motion detection applications. While the bulk PDMS/CNT cylinders displayed sensing behavior and could be used for human motion detection, the high stiffness of the material was not ideal for functionality or comfortability for this application. The low modulus Ecoflex sensors demonstrated high conformability with the user's skin and extremely high tensile stretchability for a highly

versatile large human motion monitoring. As expected in tension, the lowest conductive CNT loading (1.5 wt%) displayed higher piezoresistive sensitivity or gauge factor. Additionally, higher curing temperatures and a nozzle inner diameter of 0.41 mm displayed the highest gauge factor likely due to improved CNT dispersion and alignment in the cured nanocomposite sensing element. The piezoresistive sponge compression sensors developed and investigated in this work were easy to manufacture and displayed high usability for detecting different human motions. The simple fabrication method used allowed the manufacturer to control the electrical and mechanical properties of the sponges. The CNTs were well embedded within the PDMS matrix to avoid nanoparticle detachment to keep the user safe during use. A novel rapid microwave-based porogen removal method was used to efficiently remove the porogen from the sponge samples. The least porous and most conductive (CNT3P70) sponges demonstrated the highest compressive piezoresistive sensitivity, most reliable contact with the electrodes, and had the most consistent piezoresistive behavior. Overall, the flexible sensors developed in this work were safely skin-attachable and highly versatile for human motion detection applications.

6.1.3 Developing the SOS

The sorbent material used in the SOS prototype consisted of a PDMS sponge with embedded CB. The formulation of the nanocomposite sponge was heavily studied to optimize the durability, rate of oil absorption, hydrophobicity, and Joule heating functionality. The CB15P9 sponge material was ideal for low-cost testing of the SOS prototype and was used to fabricate the sponge funnels in this work. However, the CB20P9 sponge material performed comparably to CB15P9, except it contained a sufficiently high CB loading for effectively Joule heating the sorbent for rapid viscous oil absorption that was explored and demonstrated in the small-scale. The SOS prototype demonstrated a high maximum rate of gasoline extraction of 200 mL/min. The oil/water separation

mechanism demonstrated in the SOS was entirely gravity-driven. Therefore, no energy input was required for oil/water separation, unlike most traditional oil skimmers. The SOS was highly reusable and demonstrated the potential to help solve the issue of massive solid waste produced by single-use sorbents used widely for oil spill cleanup.

6.2 Future Work

6.2.1 Microwave-curing Effects and Applications

Further examination of the microwave-curing effects on the degree of cure and tensile properties should be explored to expand upon the studies reported in this work. It is expected that the crosslinking density is lower in rapidly microwave-cured thermoset resins compared to thermally-cured counterparts. This would explain the lower compressive modulus found in this work and the likely lower tensile modulus expected through future investigations. Additional experiments to better understand the likely CNT alignment effect caused by microwave-curing may also be explored via coating CNTs with fluorescent nanoparticles like quantum dots to image the transparent polymer matrix nanocomposite via confocal microscopy. Another method may be to microwave-cure a very thin film of PDMS/CNT prepolymer for light microscopy imaging. More work needs to be done to investigate the material property impact of microwave-curing CNT-based nanocomposites to fully understand the benefits and downsides of using this rapid manufacturing method. One important application of microwave-curing is the potential to incorporate the technique with DIW of thermoset materials to rapidly cure the thermoset materials and enable true large-scale 3D printing of thermoset parts.

6.2.2 Improvements in Flexible Sensor Designs

The biggest limitation of the skin-attachable flexible sensors developed was the electrodes. Silver epoxy and copper tape or wires were used in this work and have been widely used in the field to collect piezoresistive data from flexible sensors. However, additional work is required to improve the durability and consistency of electrical contact between the conductive metal electrodes with the semiconductive polymer nanocomposite. The e-3DP approach could be utilized to embed a silver nanocomposite thermoset paste into the polymer and attach a wire to the silver electrode for reliable contact with the sensing material. To improve the sensing element design, a cured Ecoflex substrate containing embedded silver electrodes may be stretched to a high strain such as 100 % (up to 500 %) as illustrated in Figure 6.1(a). While the substrate is held in tension, parallel lines of a high CNT loading elastomeric nanocomposite ink may be printed perpendicular to the strain axis and between and on the two silver electrodes with a small, predetermined space between each line. If the CNT loading is sufficiently high for the filamentary extrusion to maintain a highly cylindrical shape, the fully cured sample when released to 0 % strain would have highly overlapped nanocomposite lines connecting the two embedded silver electrodes (low resistance). The simplified piezoresistive strain sensing mechanism is shown in Figure 6.1 and the top view of the full sensor design is displayed in Figure 6.2. Overall, this novel fabrication method may be used to fabricate skin-attachable strain sensors with greatly improved sensitivity, significant improvements in reliable connection of the electrodes, and the ability to tailor the detectable strain range. Modeling the fabrication process should be utilized to customize the manufacturing parameters to accurately design and 3D print sensors with very high sensitivity in a strain range determined by the desired application for the human motion detection sensor.

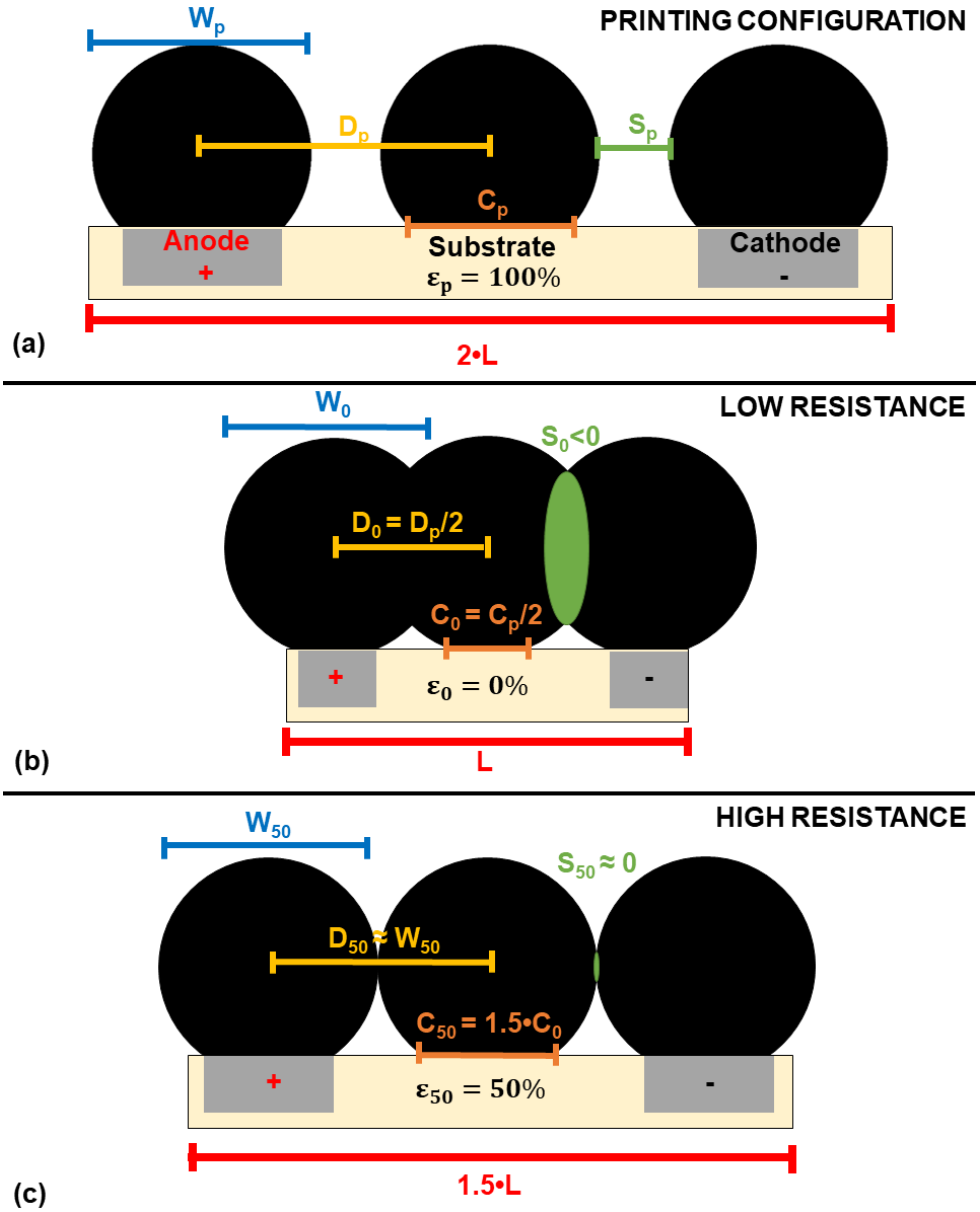

Figure 6.1: *Simplified schematic illustration of the cross-sectional view of the proposed sensor (a) after printing on the stretched substrate, (b) at rest, and (c) strained to its assumed (not calculated/simulated) maximum detectable strain.*

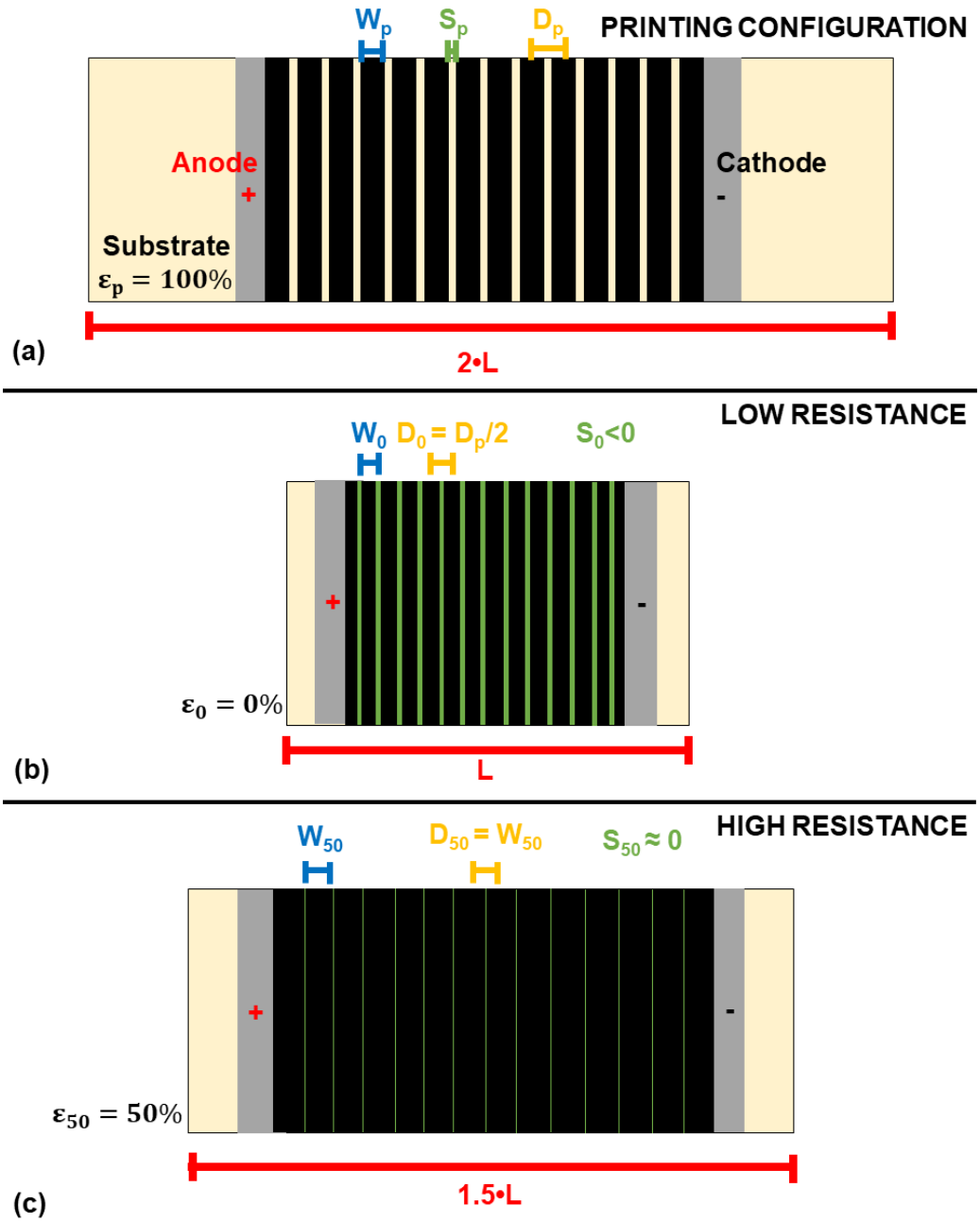

Figure 6.2: *Schematic illustration of the top view of the proposed sensor (a) after printing on the stretched substrate, (b) at rest, and (c) strained to its assumed (not calculated/simulated) maximum detectable strain.*

6.2.3 SOS Embodiments and Applications

The SOS may demonstrate improved functionality or oil extraction rate depending on the design.

Several different geometries of the sponge funnel may include altering the shape of the sponge

sheet, sponge shell, or vessel. For example, a crescent or horseshoe-shaped sponge sheet could be used to enable collecting a thin sheen of spilled oil by corralling the oil as the SOS moves across the water surface like an oil boom. Notably, the flower-shaped sponge sheet investigated in this work maintained a higher extraction efficiency for thin oil sheens due to a higher surface area of sponge remaining in contact with the oil, while the flat cylindrical sheets demonstrated an overall faster extraction rate due to the larger top surface of the sponge benefiting from gravity-driven oil absorption. These two designs could be used in conjunction such that the top surface area is larger, and the in-plane surface area is also high to rapidly extract oil and maintain a higher extraction efficiency for thin oil layers. Additionally, the SOS system design requires considerable improvements to be applicable for commercial use. One such improvement may include the incorporation of strategically placed water sensors and a snorkel connected to the ballast tank and a low-pressure blower to utilize a control loop to create a self-balancing SOS. This self-balancing or standalone flotation capability may also be achieved by incorporating the SOS design with a Weir-type oil skimmer that uses three surrounding ballast tanks to maintain the desired semi-submerged state of the device. The addition of an oil collection chamber, controllable propulsion, and drone ship functionality offers the potential for the SOS to be entirely standalone and sweep through the spilled oil slicks. Overall, considerable R&D will be required to fully unlock this innovation as we have only begun to *skim the surface* of what the SOS may be capable of.

APPENDIX A: SUPPORTING INFORMATION

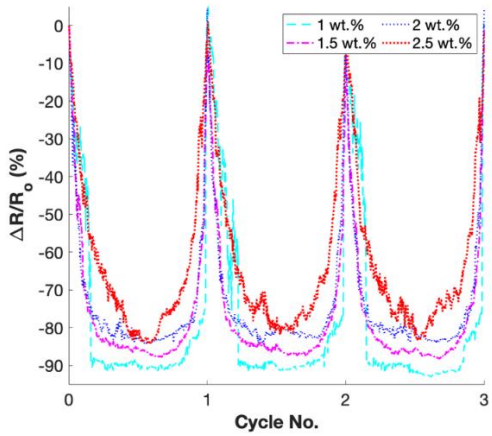

Figure A.1: *Piezoresistive sensing comparison of varying CNT loadings of m-PDMS/CNT.*

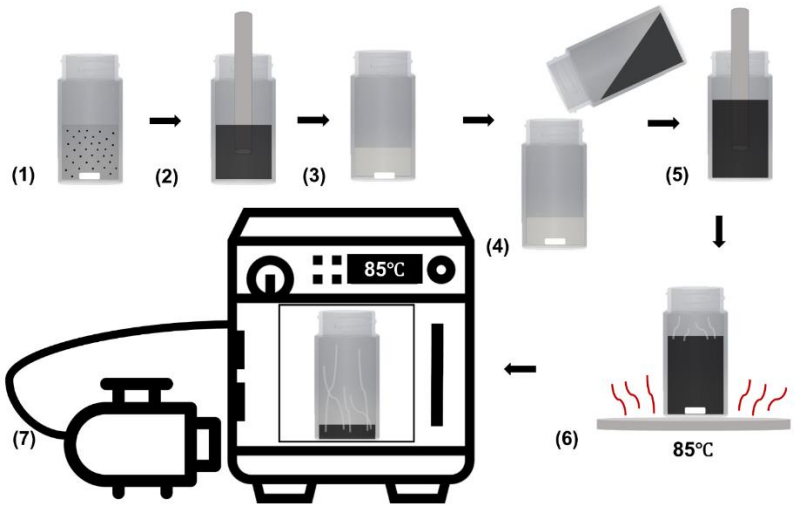

Figure A.2: *Schematic of solvent-based probe tip sonication method used to disperse CNTs in Ecoflex Part A to prepare the nanocomposite ink.*

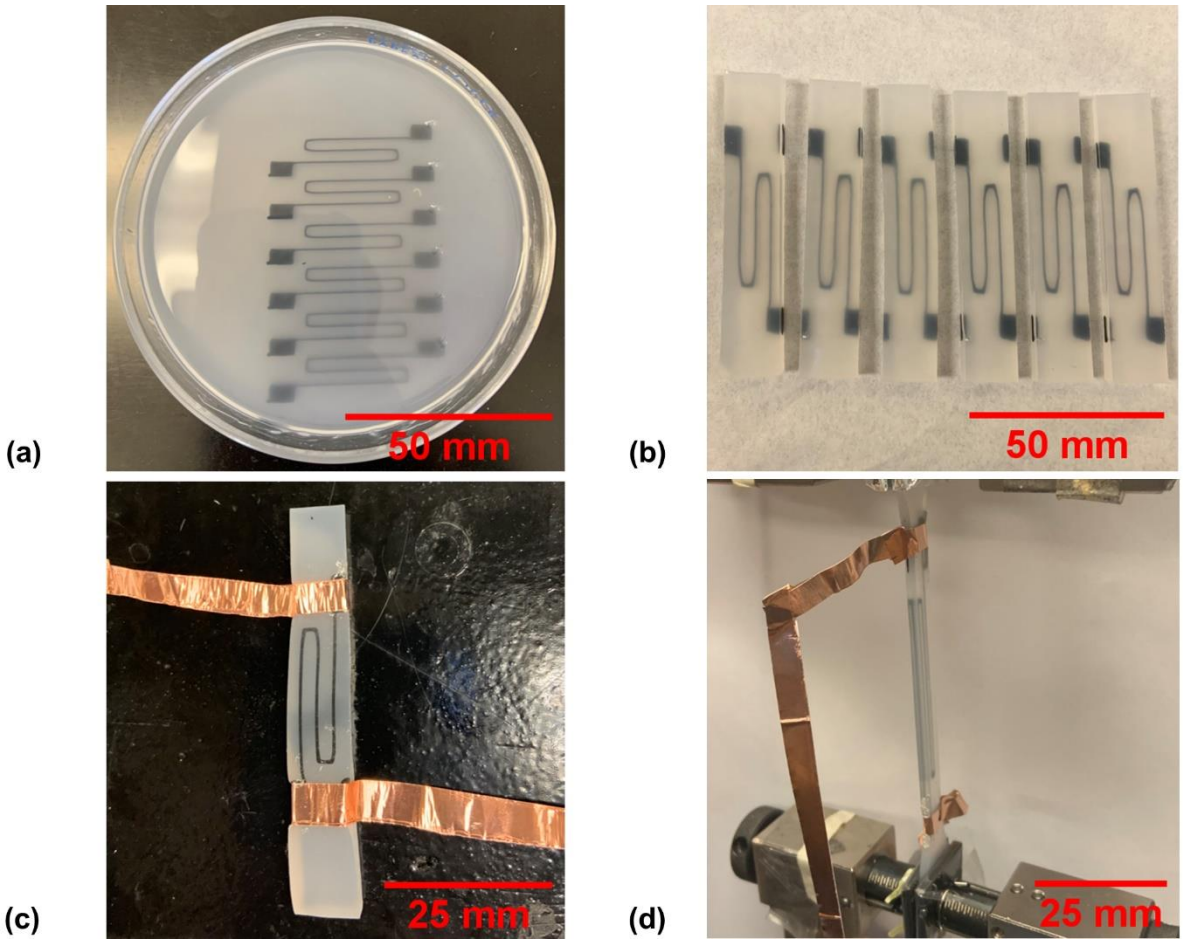

Figure A.3: *Pictures of (a) uncured Ecoflex resin bath containing six embedded printed nanocomposite sensors, (b) fully cured sensors after being cut lengthwise along the nanocomposite electrodes, (c) prepared embedded nanocomposite sensor with silver epoxy and copper tape electrodes, and (d) embedded sensor extended to 120 % strain to tighten copper tape around the sample.*

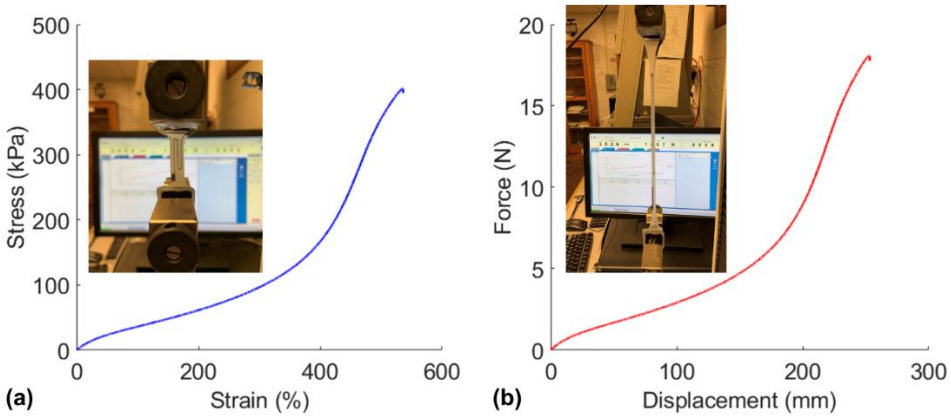

Figure A.4: *Embedded sensor fracture test: (a) Stress-strain curve and a picture of the embedded sensor unstretched. (b) Force-displacement curve and a picture of the sensor stretched to over 500 % strain before failure.*

Table A.1: *Designation of CNT Nanocomposite Sponge Materials Investigated*

Sponge Material Designation	Sugar Porogen Amount (wt%)	CNT Loading (wt%)
CNT1.5P70	70	1.5
CNT2P70	70	2
CNT2.5P70	70	2.5
CNT3P70	70	3
CNT3P75	75	3
CNT3P80	80	3
CNT3P85	85	3

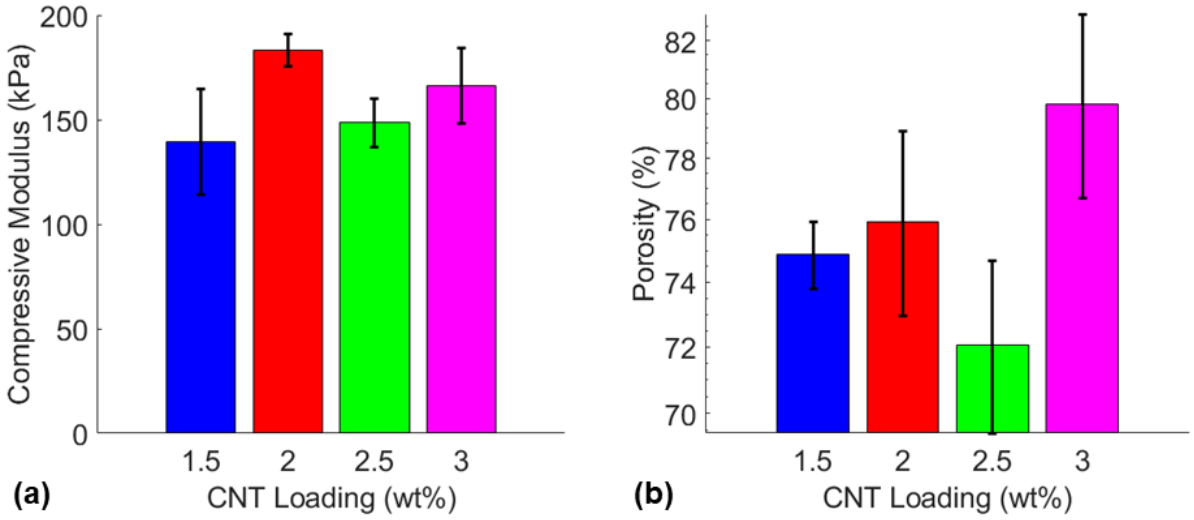

Figure A.5: *Comparison of the (a) compressive modulus and (b) the measured porosities of the CNT1.5P70, CNT2P70, CNT2.5P70, and CNT3P70 sponges.*

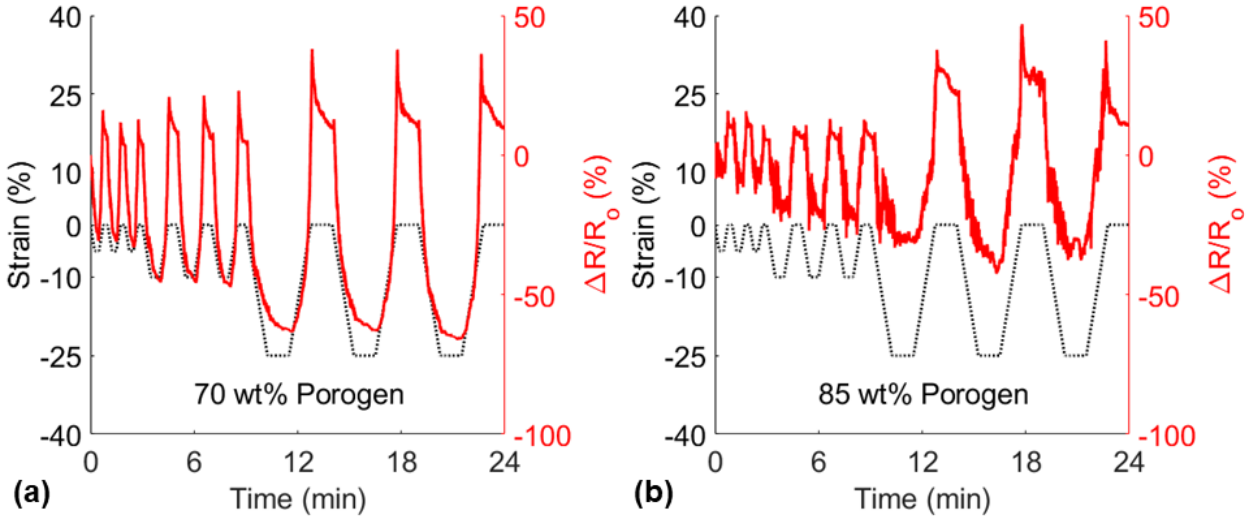

Figure A.6: *Piezoresistive stepwise sensing comparison of (a) the lowest porosity sponge (CNT3P70) and (b) the highest porosity sponge (CNT3P85) for 5 %, 10 %, and 25 % compressive strains.*

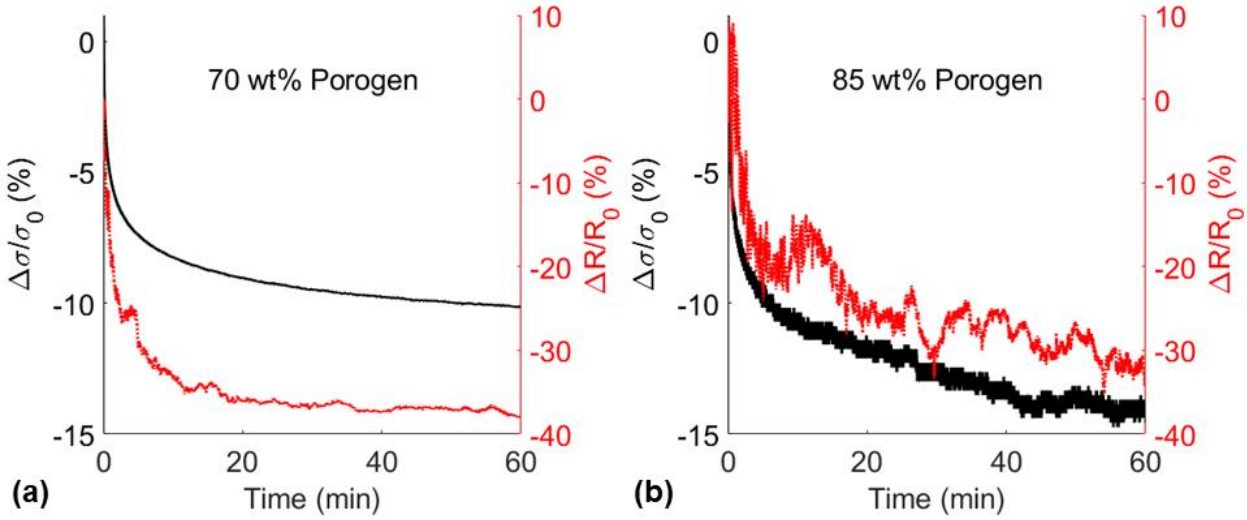

Figure A.7: *Viscoelastic creep comparison of the piezoresistive and stress response for (a) the lowest porosity sponge (CNT3P70) and (b) the highest porosity sponge (CNT3P85) held at 50 % compressive strain for 1 h.*

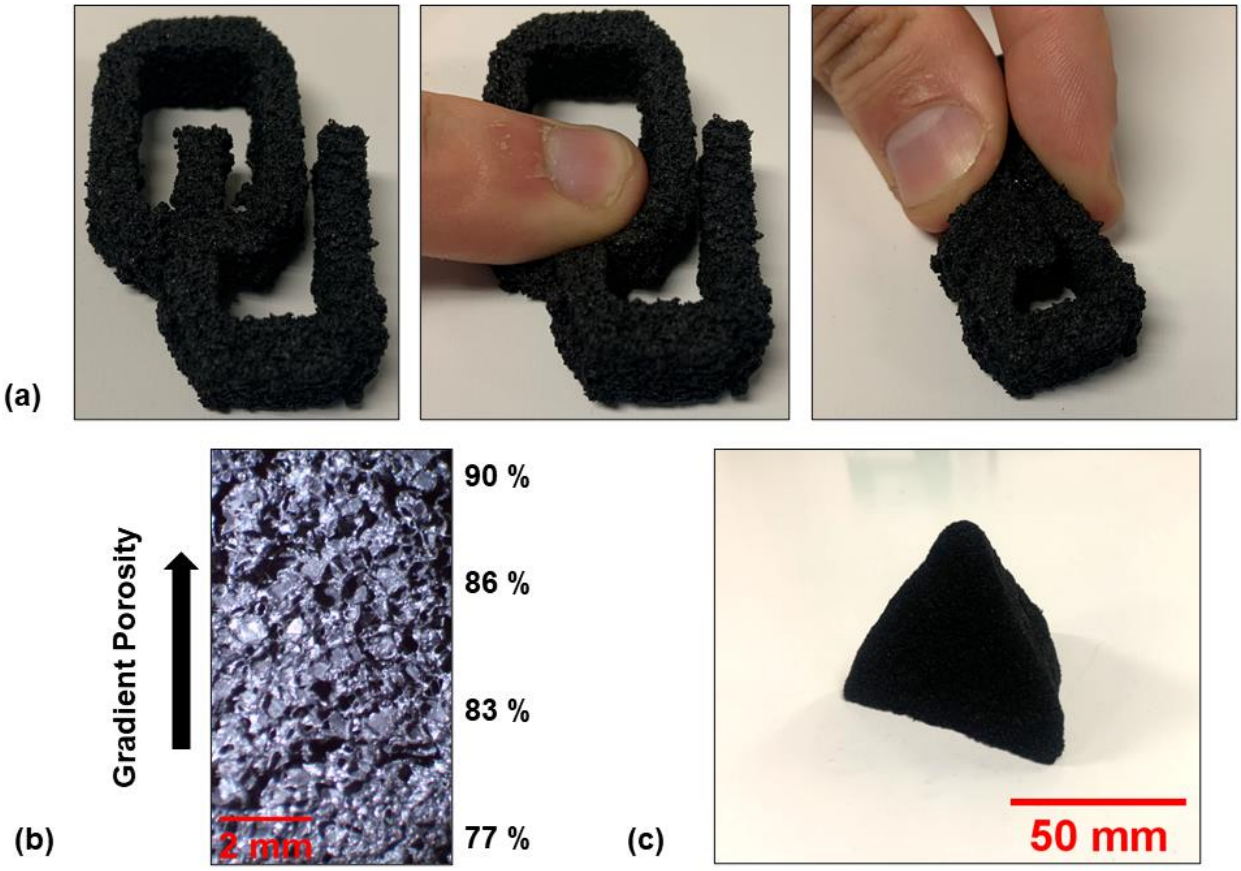

Figure A.8: *Pictures of fabricated nanocomposite sponges including (a) the University of Oklahoma logo, (b) a sample with gradient porosity, and (c) a triangular pyramid.*

Table A.2: *Designation of CB Nanocomposite Sponge Materials Investigated*

Sponge Material Designation	Salt Porogen:PDMS/CB Prepolymer	CB Loading (wt%)
CB15P4	4:1	15
CB15P6	5.7:1	15
CB15P9	9:1	15
CB5P9	9:1	5
CB10P9	9:1	10
CB20P9	9:1	20
CB25P9	9:1	25

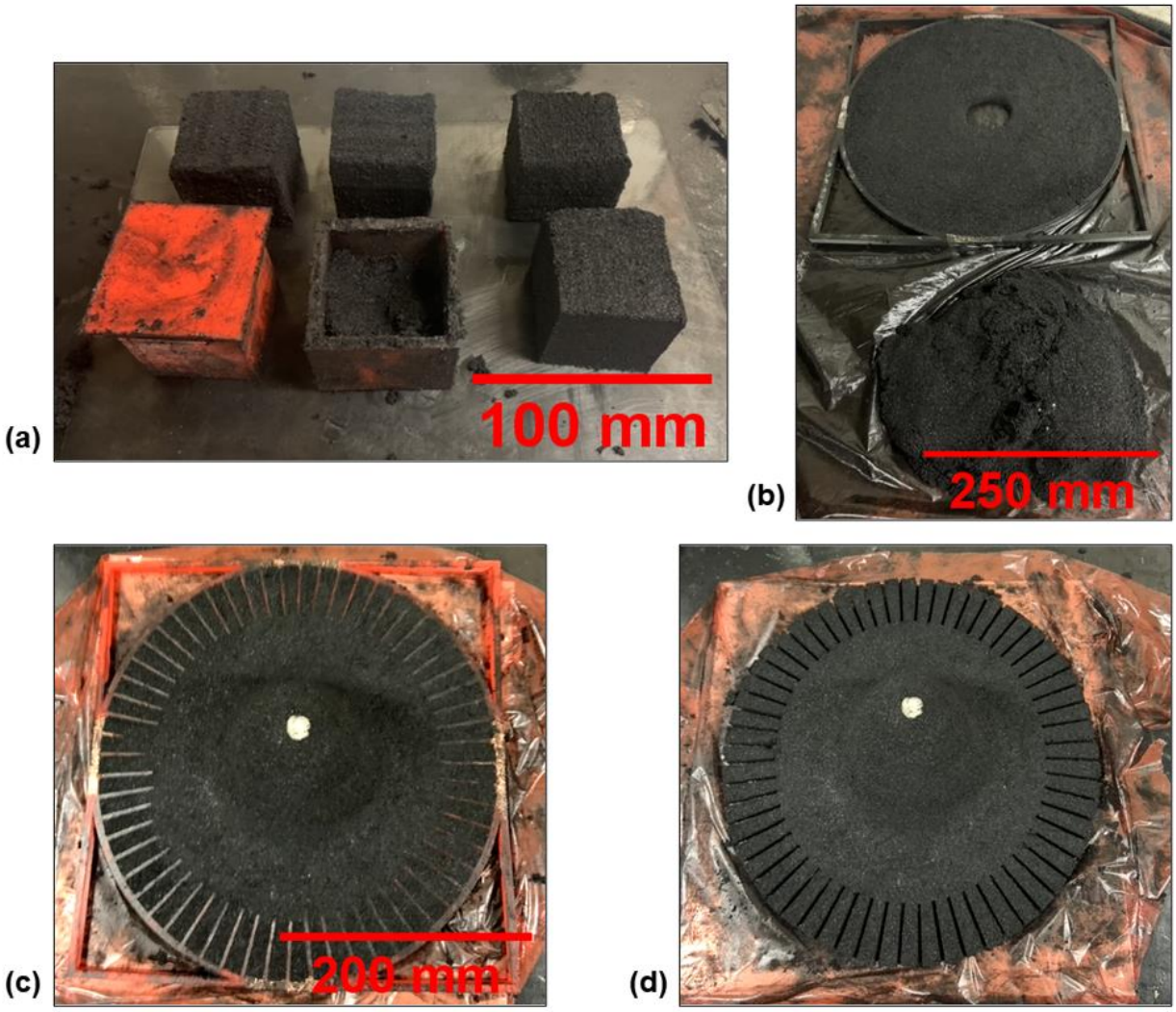

Figure A.9: *Pictures of the PCS templating fabrication methods used (a) to fabricate sponge cubes, (b) a circular sponge sheet, and (c, d) the flower-shaped sponge funnel with 60 pedals.*

(a) 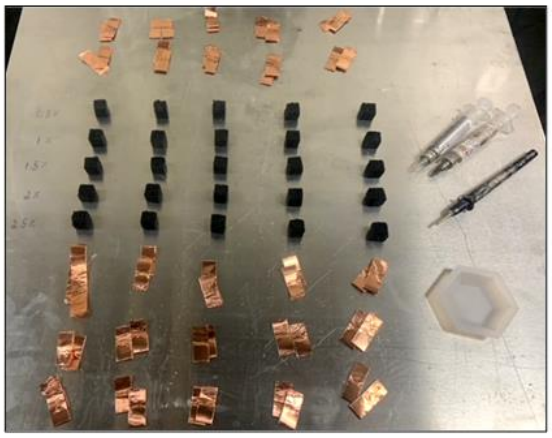 (b) 

Figure A.10: *Pictures of the (a) small cube sponges and tools and materials used to attach electrodes and (b) the multimeter measuring the resistance of a small cube sponge.*

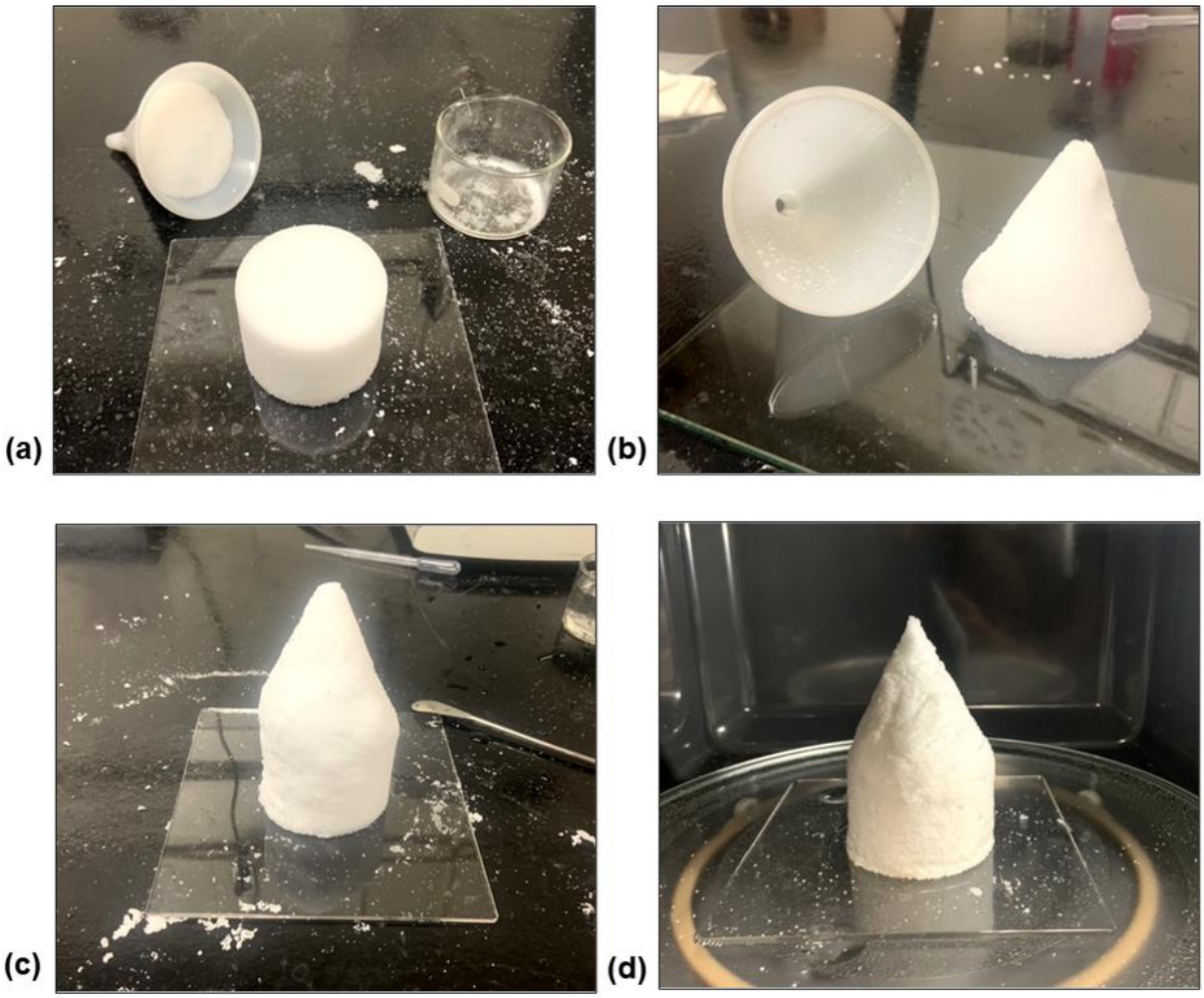

Figure A.11: *Pictures of the large salt porogen fabrication method including (a) molding the cylindrical base and (b) the cone top, (c) stacking the cone onto the cylindrical base, and (d) hardening the extended cone-shaped porogen in a commercial microwave.*

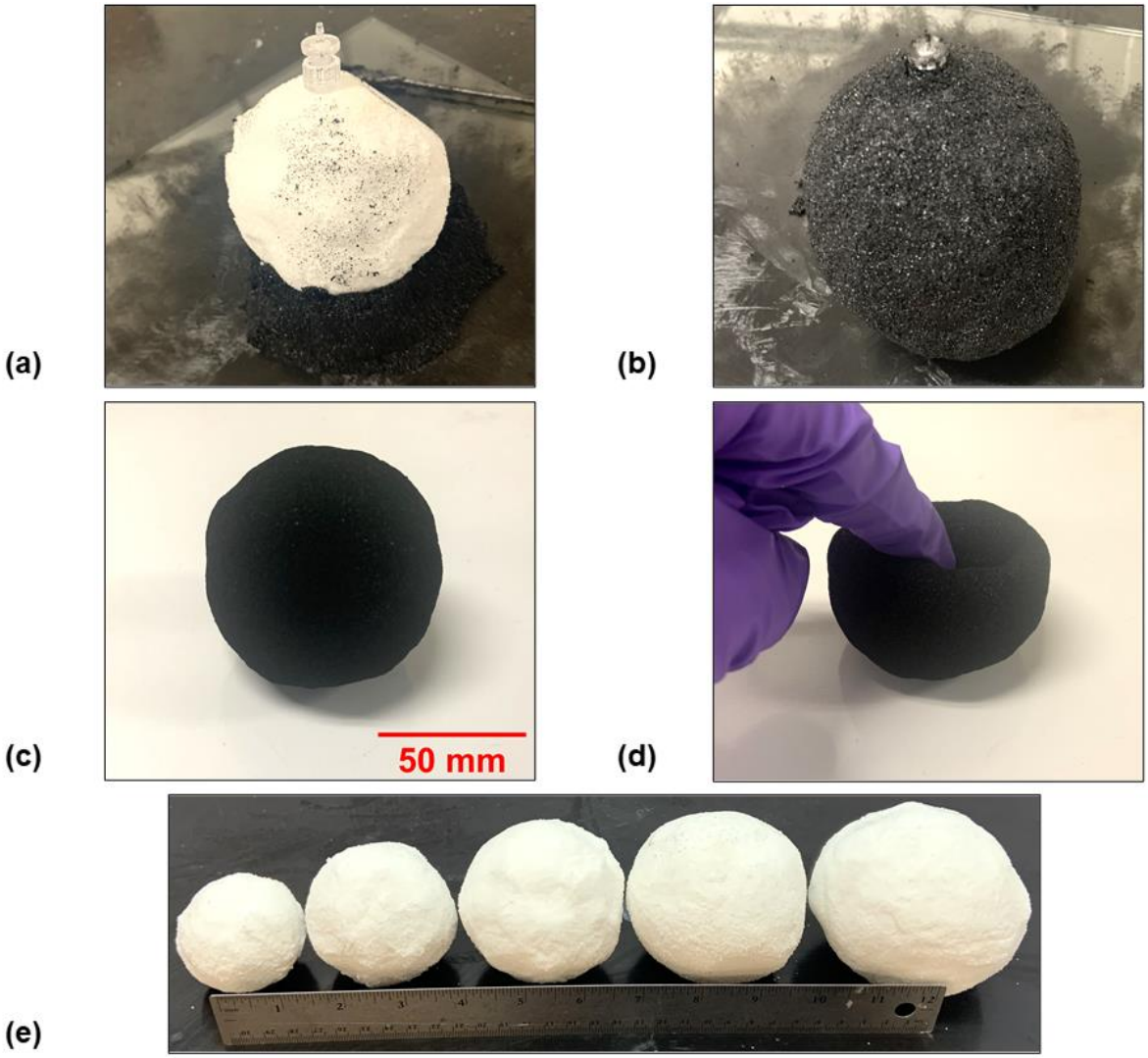

Figure A.12: *Picture of the preliminary investigation of spherical shell-structured PDMS sponge sorbents including the (a, b) the fabrication method of covering the salt ball with PCS, (c, d) a fabricated hollow spherical sponge, and e) the scalability of the salt ball porogen.*

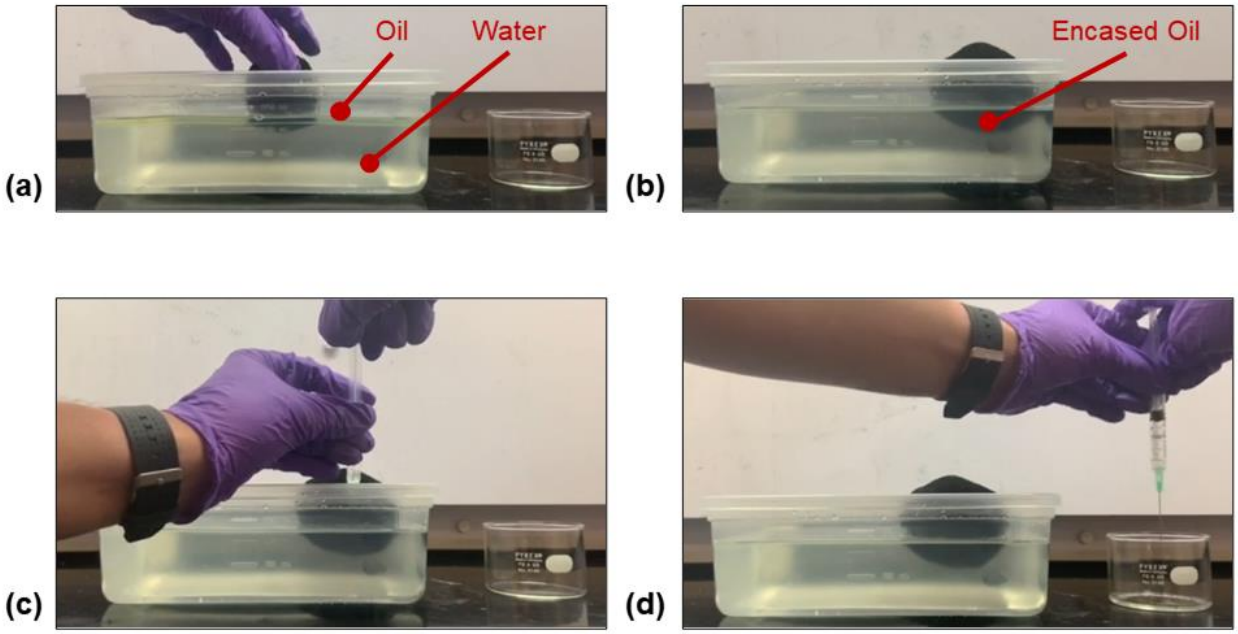

Figure A.13: *Picture of the preliminary spherical hollow shell sponge oil absorption in water experiment including (a) deployment, (b) oil absorption and separation from water, (c) extraction of the encased oil inside the shell sponge, and (d) depositing extracted oil into a separate container.*

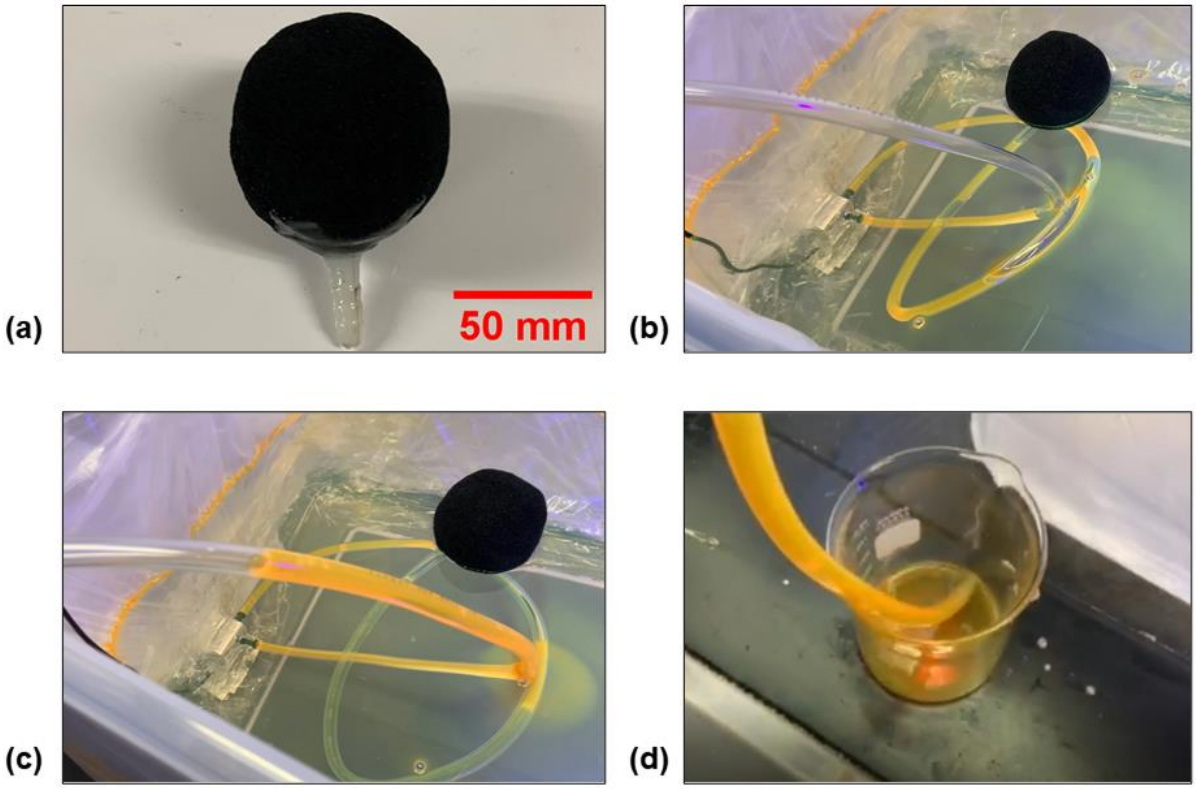

Figure A.14: *Pictures of (a) fabricated spherical shell sponge with attached connector for oil extraction, (b) deployment of the hollow sponge device in a simulated oil spill, (c) pumping to remove oil, and (d) proof of oil extraction from water.*

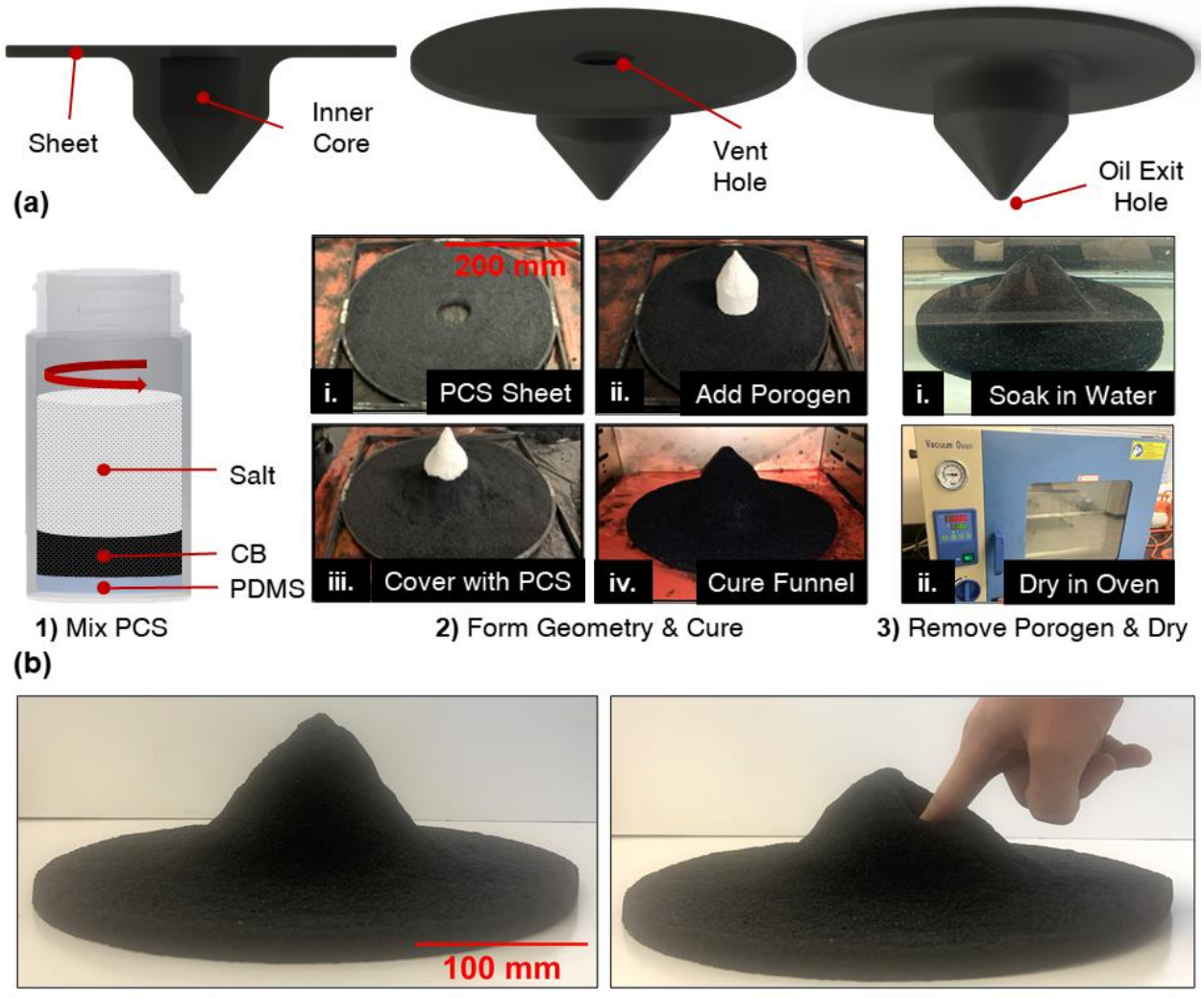

Figure A.15: *(a) The design of the nanocomposite sponge funnel, (b) the steps to fabricate the sponge funnel, and (c) pictures of a fabricated sponge funnel.*

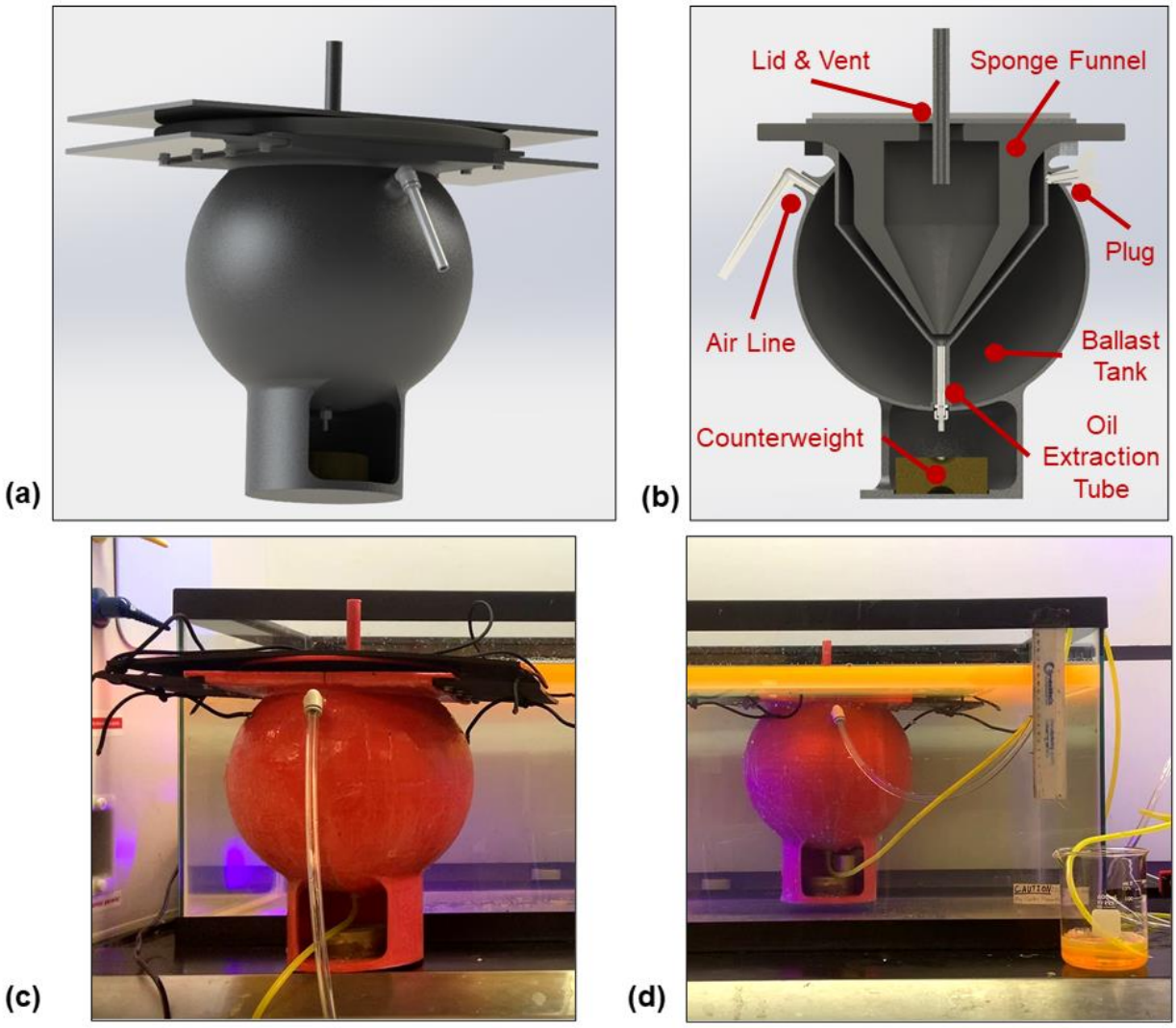

Figure A.16: *(a) Design of the first SOS prototype and (b) the labeled cross-section including a ballast tank to control the buoyancy. Pictures of the fabricated SOS prototype with a ballast tank (c) before and (d) after deployment in a simulated oil spill.*

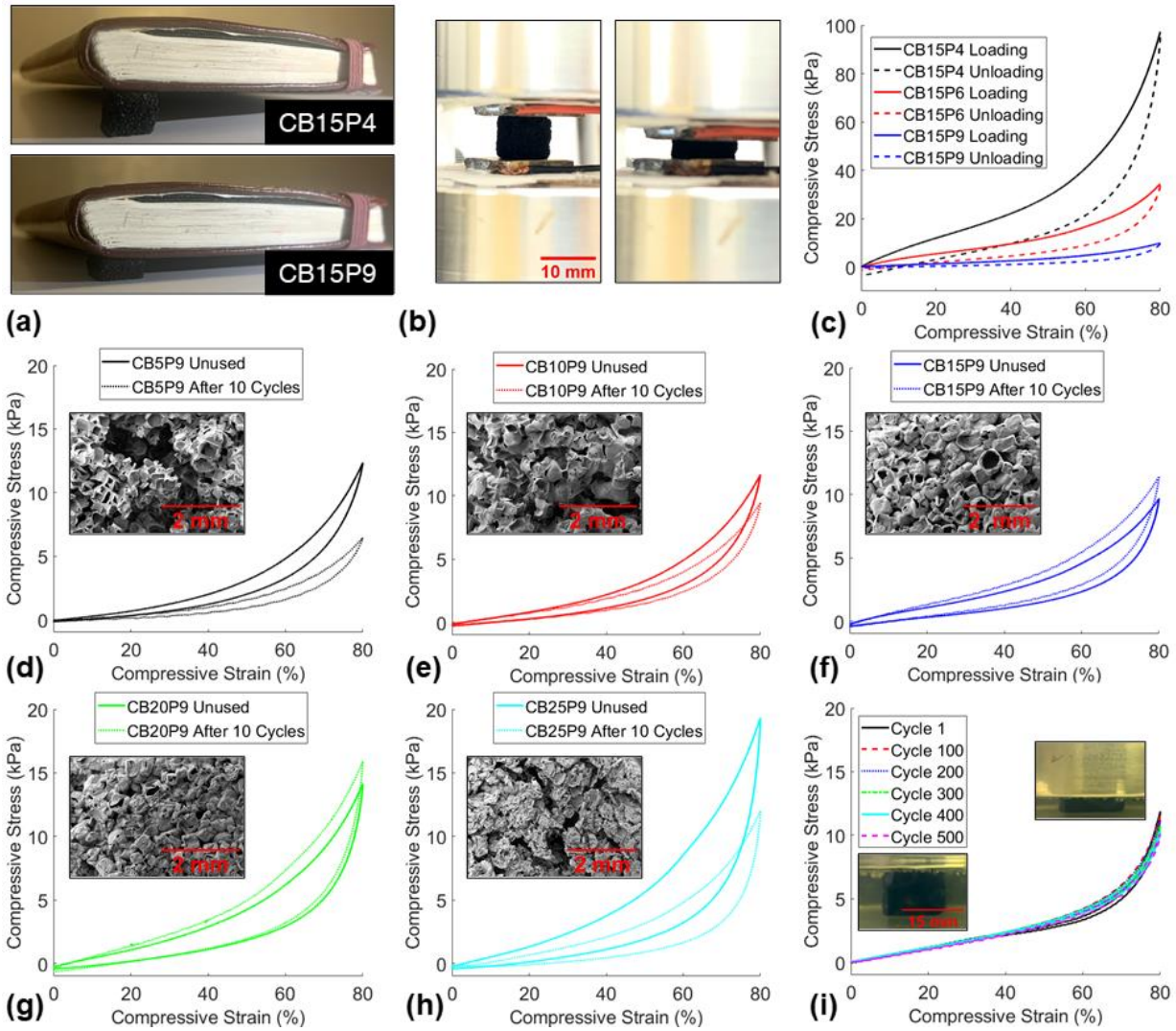

Figure A.17: *(a) Pictures of the least porous sponge (top) and the most porous sponge (bottom) under compression from a 120 g book. (b) Pictures of a small cube sponge uncompressed (left) and compressed to 80 % compressive strain. (c) Stress-strain curves of the varying porosity sponges. (d-h) Stress-strain curves of varying CB loading sponges before and after 10 cycles of gasoline sorption and SEM images of the sponge microstructure after 10 cycles. (i) Representative stress-strain curves of 500 cycles of CB15P9 submerged in gasoline.*

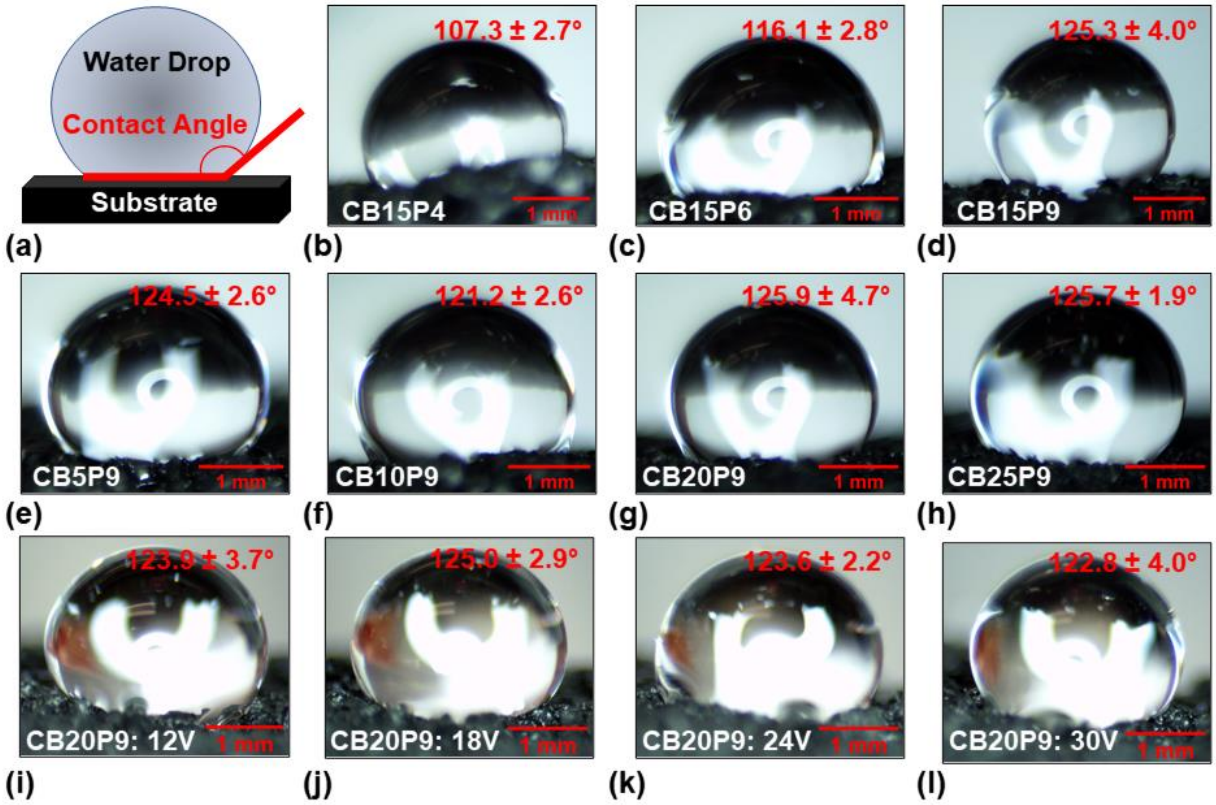

Figure A.18: *(a) Schematic showing the water contact angle of a droplet on a substrate. Representative light microscopy images of a water droplet deposited on the (b-d) varying porosity sponges, (e-h) varying CB loading sponges, and (i-l) varying Joule heating voltages applied to a CB20P9 sponge.*

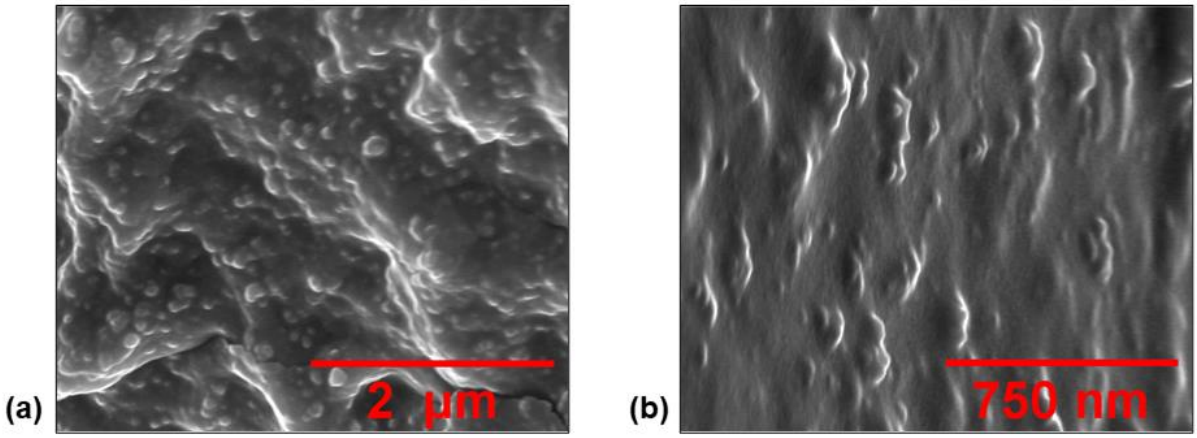

Figure A.19: *(a, b) High magnification SEM images of the surface of a CB15P9 sponge that shows the CB embedded within the PDMS matrix.*

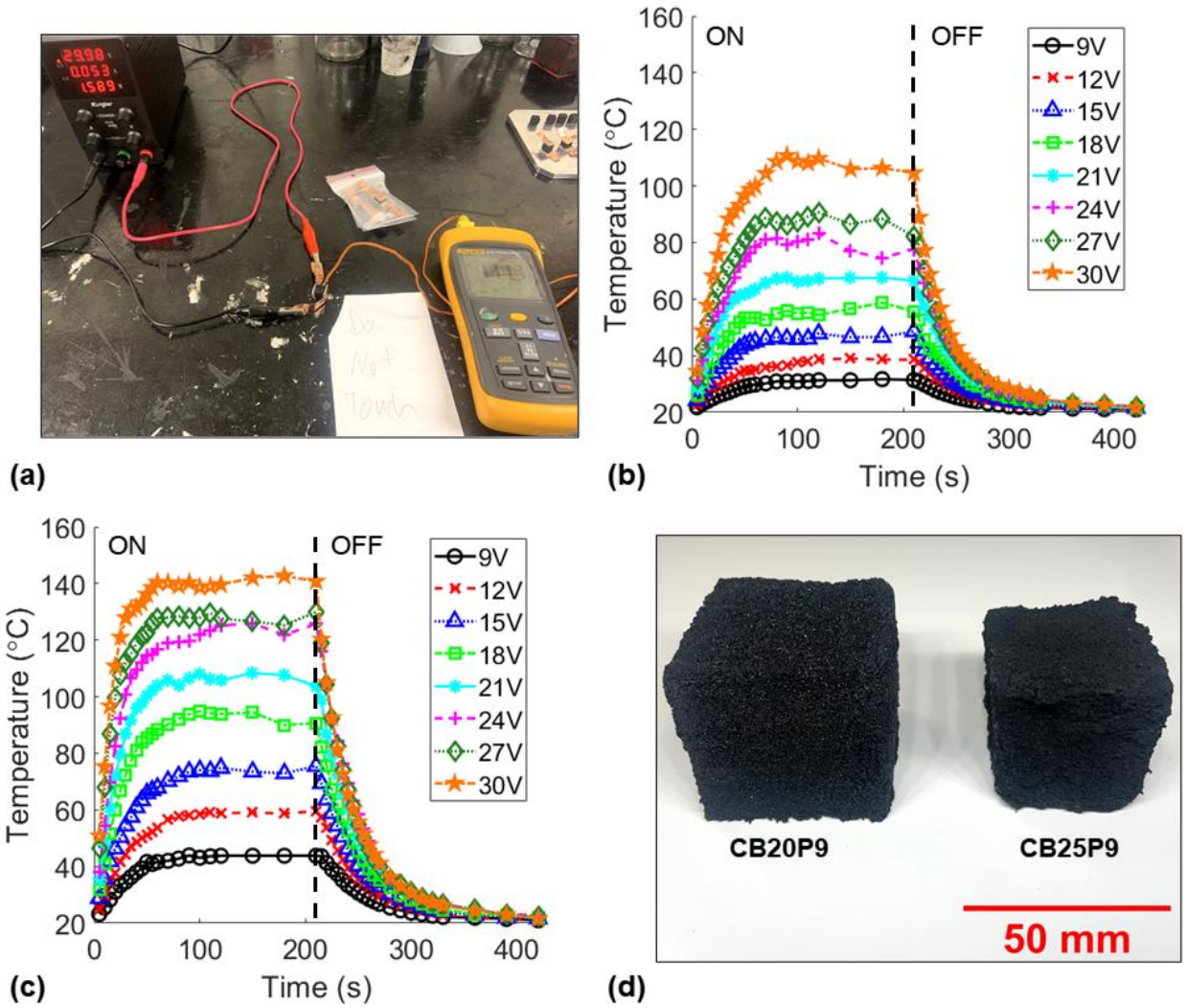

Figure A.20: *(a) Picture of the Joule heating experimental setup and measured temperature change due to 3 min of various voltages applied to a (b) CB20P9 and (c) CB25P9 small cube sponge. (d) Picture of the CB20P9 and CB25P9 large cube sponges showing the shrinkage of sponges fabricated with a 25 wt% CB loading due to the difficulty of mixing the viscous prepolymer with the salt porogen.*

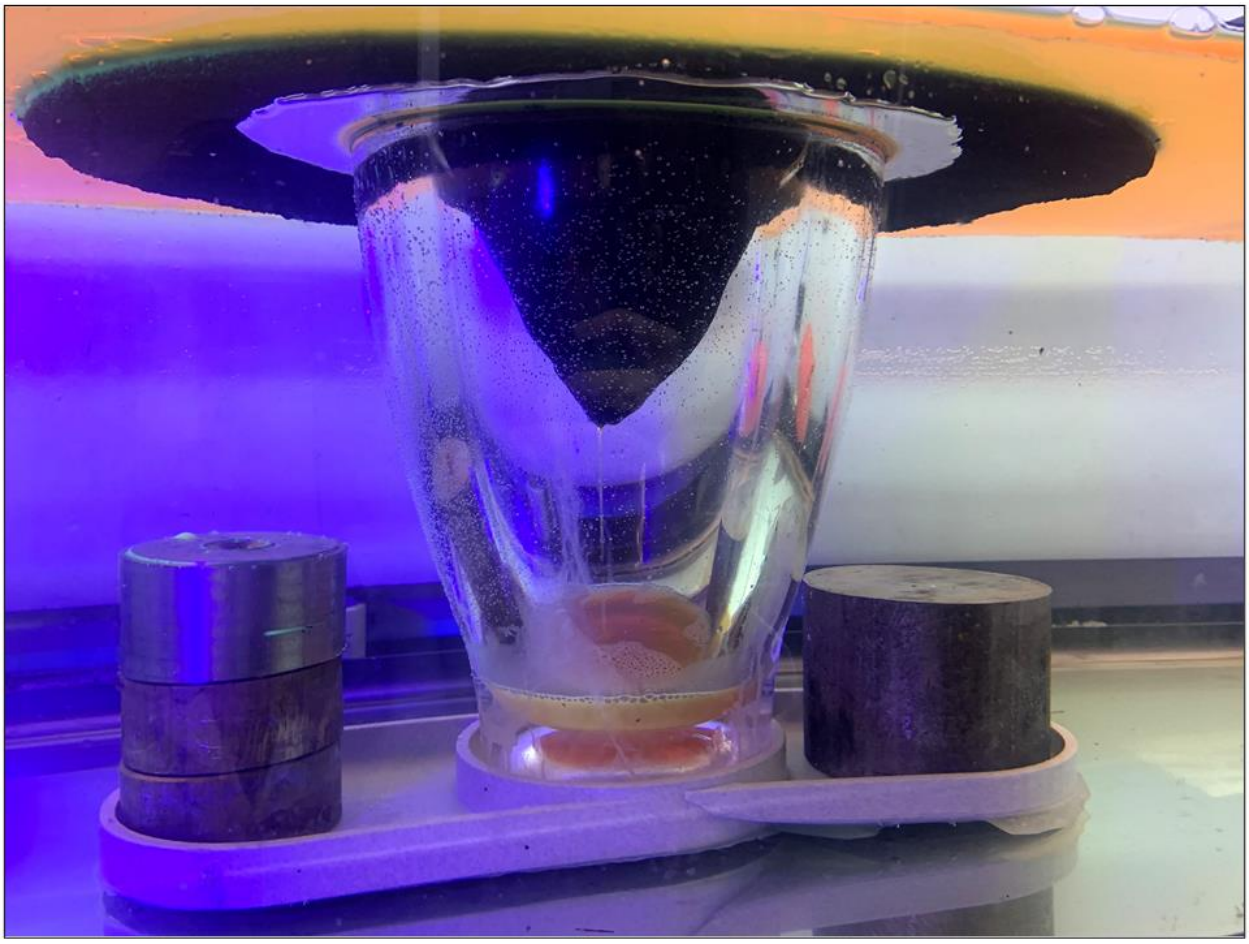

Figure A.21: *A picture of the nanocomposite sponge funnel demonstrating the gravity-driven oil/water separation capabilities in a simulated gasoline spill in water.*

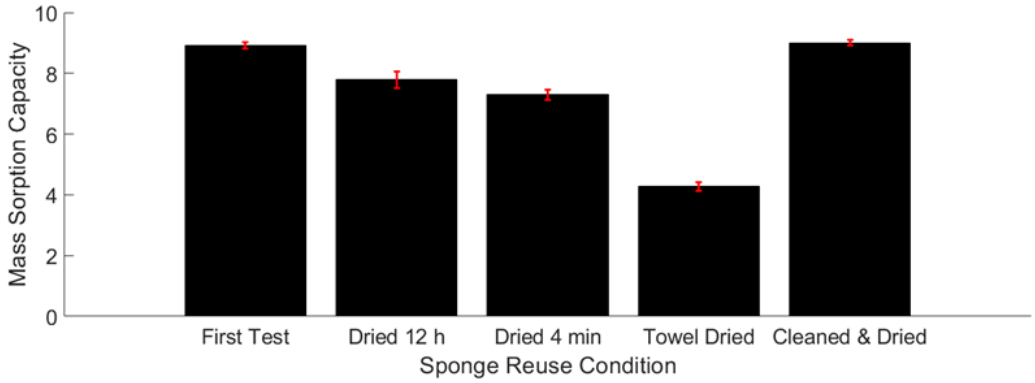

Figure A.22: *Mass sorption capacities of large CB15P9 sponges in gasoline with the same sponge reuse conditions as the sponge funnel reuse conditions tested in the SOS gasoline extraction from water experiments.*

REFERENCES

[1] Joo Y, Byun J, Seong N, Ha J, Kim H, Kim S, et al. Silver nanowire-embedded PDMS with a multiscale structure for a highly sensitive and robust flexible pressure sensor. Nanoscale. 2015;7(14):6208-15.

[2] Gong S, Schwalb W, Wang Y, Chen Y, Tang Y, Si J, et al. A wearable and highly sensitive pressure sensor with ultrathin gold nanowires. Nature communications. 2014;5(1):1-8.

[3] Liu W, Jiang H, Ru Y, Zhang X, Qiao J. Conductive Graphene–Melamine Sponge Prepared via Microwave Irradiation. ACS applied materials & interfaces. 2018;10(29):24776-83.

[4] Ding T, Wang L, Wang P. Changes in electrical resistance of carbon-black-filled silicone rubber composite during compression. Journal of polymer science part b: Polymer physics. 2007;45(19):2700-6.

[5] Charara M, Luo W, Saha MC, Liu Y. Investigation of Lightweight and Flexible Carbon Nanofiber/Poly Dimethylsiloxane Nanocomposite Sponge for Piezoresistive Sensor Application. Advanced Engineering Materials. 2019;21(5):1801068.

[6] Chowdhury SA, Saha MC, Patterson S, Robison T, Liu Y. Highly conductive polydimethylsiloxane/carbon nanofiber composites for flexible sensor applications. Advanced Materials Technologies. 2019;4(1):1800398.

[7] Chowdhury S, Olima M, Liu Y, Saha M, Bergman J, Robison T. Poly dimethylsiloxane/carbon nanofiber nanocomposites: fabrication and characterization of electrical and thermal properties. International Journal of Smart and Nano Materials. 2016;7(4):236-47.

[8] Abshirini M, Charara M, Liu Y, Saha M, Altan MC. 3D Printing of Highly Stretchable Strain Sensors Based on Carbon Nanotube Nanocomposites. Advanced Engineering Materials. 2018;20(10):1800425.

[9] Zhang R, Deng H, Valenca R, Jin J, Fu Q, Bilotti E, et al. Strain sensing behaviour of elastomeric composite films containing carbon nanotubes under cyclic loading. Composites Science and Technology. 2013;74:1-5.

[10] Kim M-K, Kim M-S, Kwon H-B, Jo S-E, Kim Y-J. Wearable triboelectric nanogenerator using a plasma-etched PDMS–CNT composite for a physical activity sensor. RSC advances. 2017;7(76):48368-73.

[11] Gojny FH, Wichmann MH, Fiedler B, Schulte K. Influence of different carbon nanotubes on the mechanical properties of epoxy matrix composites–a comparative study. Composites Science and Technology. 2005;65(15-16):2300-13.

[12] Han Z, Fina A. Thermal conductivity of carbon nanotubes and their polymer nanocomposites: A review. Progress in polymer science. 2011;36(7):914-44.

[13] Bauhofer W, Kovacs JZ. A review and analysis of electrical percolation in carbon nanotube polymer composites. Composites Science and Technology. 2009;69(10):1486-98.

[14] Min C, Shen X, Shi Z, Chen L, Xu Z. The electrical properties and conducting mechanisms of carbon nanotube/polymer nanocomposites: A review. Polymer-Plastics Technology and Engineering. 2010;49(12):1172-81.

[15] Ramalingame R, Hu Z, Gerlach C, Rajendran D, Zubkova T, Baumann R, et al. Flexible piezoresistive sensor matrix based on a carbon nanotube PDMS composite for dynamic pressure distribution measurement. J Sens Sens Syst. 2019;8(1):1-7.

[16] Kumar S, Pavelyev V, Mishra P, Tripathi N. A review on chemiresistive gas sensors based on carbon nanotubes: Device and technology transformation. Sensor Actuat a-Phys. 2018;283:174-86.

[17] Di Bartolomeo A, Sarno M, Giubileo F, Altavilla C, Iemmo L, Piano S, et al. Multiwalled carbon nanotube films as small-sized temperature sensors. J Appl Phys. 2009;105(6).

[18] Xie XL, Mai YW, Zhou XP. Dispersion and alignment of carbon nanotubes in polymer matrix: A review. Mat Sci Eng R. 2005;49(4):89-112.

[19] Lan Y, Wang Y, Ren Z. Physics and applications of aligned carbon nanotubes. Advances in Physics. 2011;60(4):553-678.

[20] Chen X, Saito T, Yamada H, Matsushige K. Aligning single-wall carbon nanotubes with an alternating-current electric field. Applied physics letters. 2001;78(23):3714-6.

[21] Bubke K, Gnewuch H, Hempstead M, Hammer J, Green ML. Optical anisotropy of dispersed carbon nanotubes induced by an electric field. Applied physics letters. 1997;71(14):1906-8.

[22] Lu JP. Novel magnetic properties of carbon nanotubes. Physical review letters. 1995;74(7):1123.

[23] Rao SG, Huang L, Setyawan W, Hong S. Large-scale assembly of carbon nanotubes. Nature. 2003;425(6953):36-7.

[24] Seemann KM, Ebbecke J, Wixforth A. Alignment of carbon nanotubes on pre-structured silicon by surface acoustic waves. Nanotechnology. 2006;17(17):4529.

[25] Jin L, Bower C, Zhou O. Alignment of carbon nanotubes in a polymer matrix by mechanical stretching. Applied physics letters. 1998;73(9):1197-9.

[26] Herren B, Gu T, Tang Q, Saha M, Liu Y. 3D Printing and Stretching Effects on Alignment Microstructure in PDMS/CNT Nanocomposites. ASME 2019 International Mechanical

Engineering Congress and Exposition: American Society of Mechanical Engineers Digital Collection; 2019.

[27] Goh GL, Agarwala S, Yeong WY. Directed and On-Demand Alignment of Carbon Nanotube: A Review toward 3D Printing of Electronics. Advanced Materials Interfaces. 2019;6(4):1801318.

[28] Khan SU. Effects of carbon nanotube alignment on electrical and mechanical properties of epoxy nanocomposites. Composites. 2013;v. 49:pp. 26-34-2013 v.49.

[29] Lee WI, Springer GS. Microwave curing of composites. Journal of Composite Materials. 1984;18(4):387-409.

[30] Thostenson ET, Chou TW. Microwave and conventional curing of thick-section thermoset composite laminates: Experiment and simulation. Polymer composites. 2001;22(2):197-212.

[31] Boey F, Lye S. Void reduction in autoclave processing of thermoset composites: Part 2: Void reduction in a microwave curing process. Composites. 1992;23(4):266-70.

[32] Degamber B, Fernando G. Microwave processing of thermosets: non-contact cure monitoring and fibre optic temperature sensors. Plastics, rubber and composites. 2003;32(8-9):327-33.

[33] Fotiou I, Baltopoulos A, Vavouliotis A, Kostopoulos V. Microwave curing of epoxy polymers reinforced with carbon nanotubes. Journal of Applied Polymer Science. 2013;129(5):2754-64.

[34] Menéndez J, Arenillas A, Fidalgo B, Fernández Y, Zubizarreta L, Calvo EG, et al. Microwave heating processes involving carbon materials. Fuel Processing Technology. 2010;91(1):1-8.

[35] Ye Z, Deering WD, Krokhin A, Roberts JA. Microwave absorption by an array of carbon nanotubes: A phenomenological model. Physical Review B. 2006;74(7):075425.

[36] Vazquez E, Prato M. Carbon Nanotubes and Microwaves: Interactions, Responses, and Applications. Acs Nano. 2009;3(12):3819-24.

[37] Chang J, Liang G, Gu A, Cai S, Yuan L. The production of carbon nanotube/epoxy composites with a very high dielectric constant and low dielectric loss by microwave curing. Carbon. 2012;50(2):689-98.

[38] Ma P-C, Liu M-Y, Zhang H, Wang S-Q, Wang R, Wang K, et al. Enhanced Electrical Conductivity of Nanocomposites Containing Hybrid Fillers of Carbon Nanotubes and Carbon Black. Acs Appl Mater Inter. 2009;1(5):1090-6.

[39] Wichmann O, Ahonen K, Sillanpää R. Uranyl (VI) complexes with a diaminobisphenol from eugenol and N-(2-aminoethyl) morpholine: Syntheses, structures and extraction studies. Polyhedron. 2011;30(3):477-85.

[40] Li C, Thostenson ET, Chou T-W. Effect of nanotube waviness on the electrical conductivity of carbon nanotube-based composites. Composites Science and Technology. 2008;68(6):1445-52.

[41] Bai J, Allaoui A. Effect of the length and the aggregate size of MWNTs on the improvement efficiency of the mechanical and electrical properties of nanocomposites—experimental investigation. Composites Part A: applied science and manufacturing. 2003;34(8):689-94.

[42] Martin C, Sandler J, Shaffer M, Schwarz M-K, Bauhofer W, Schulte K, et al. Formation of percolating networks in multi-wall carbon-nanotube–epoxy composites. Composites Science and Technology. 2004;64(15):2309-16.

[43] Gong S, Zhu Z, Meguid S. Carbon nanotube agglomeration effect on piezoresistivity of polymer nanocomposites. Polymer. 2014;55(21):5488-99.

[44] Chen L, Liu Y, Leng J. Microwave responsive epoxy nanocomposites reinforced by carbon nanomaterials of different dimensions. Journal of Applied Polymer Science. 2018;135(2):45676.

[45] Kwak M, Robinson P, Bismarck A, Wise R. Microwave curing of carbon–epoxy composites: penetration depth and material characterisation. Composites Part A: Applied Science and Manufacturing. 2015;75:18-27.

[46] Rangari VK, Bhuyan MS, Jeelani S. Microwave processing and characterization of EPON 862/CNT nanocomposites. Materials Science and Engineering: B. 2010;168(1):117-21.

[47] Sung P-C, Chiu T-H, Chang S-C. Microwave curing of carbon nanotube/epoxy adhesives. Composites Science and Technology. 2014;104:97-103.

[48] Muth JT, Vogt DM, Truby RL, Mengüç Y, Kolesky DB, Wood RJ, et al. Embedded 3D printing of strain sensors within highly stretchable elastomers. Advanced Materials. 2014;26(36):6307-12.

[49] Abshirini M, Charara M, Marashizadeh P, Saha MC, Altan MC, Liu YT. Functional nanocomposites for 3D printing of stretchable and wearable sensors. Appl Nanosci. 2019;9(8):2071-83.

[50] Herren B, Charara M, Saha MC, Altan MC, Liu Y. Rapid Microwave Polymerization of Porous Nanocomposites with Piezoresistive Sensing Function. Nanomaterials. 2020;10(2):233.

[51] Zhu D, Handschuh-Wang S, Zhou X. Recent progress in fabrication and application of polydimethylsiloxane sponges. Journal of Materials Chemistry A. 2017;5(32):16467-97.

[52] Yang J, Ye Y, Li X, Lü X, Chen R. Flexible, conductive, and highly pressure-sensitive graphene-polyimide foam for pressure sensor application. Composites Science and Technology. 2018;164:187-94.

[53] Wu S, Zhang J, Ladani RB, Ravindran AR, Mouritz AP, Kinloch AJ, et al. Novel electrically conductive porous PDMS/carbon nanofiber composites for deformable strain sensors and conductors. ACS applied materials & interfaces. 2017;9(16):14207-15.

[54] Sengupta D, Pei Y, Kottapalli AGP. Ultralightweight and 3D Squeezable Graphene-Polydimethylsiloxane Composite Foams as Piezoresistive Sensors. ACS applied materials & interfaces. 2019;11(38):35201-11.

[55] Liang S, Li Y, Yang J, Zhang J, He C, Liu Y, et al. 3D Stretchable, Compressible, and Highly Conductive Metal-Coated Polydimethylsiloxane Sponges. Advanced Materials Technologies. 2016;1(7):1600117.

[56] Rinaldi A, Tamburrano A, Fortunato M, Sarto MS. A flexible and highly sensitive pressure sensor based on a PDMS foam coated with graphene nanoplatelets. Sensors. 2016;16(12):2148.

[57] Chen H, Miao L, Su Z, Song Y, Han M, Chen X, et al. Fingertip-inspired electronic skin based on triboelectric sliding sensing and porous piezoresistive pressure detection. Nano Energy. 2017;40:65-72.

[58] Fan YJ, Meng XS, Li HY, Kuang SY, Zhang L, Wu Y, et al. Stretchable Porous Carbon Nanotube-Elastomer Hybrid Nanocomposite for Harvesting Mechanical Energy. Advanced Materials. 2017;29(2):1603115.

[59] Beccai L, Roccella S, Arena A, Valvo F, Valdastri P, Menciassi A, et al. Design and fabrication of a hybrid silicon three-axial force sensor for biomechanical applications. Sensors and Actuators A: Physical. 2005;120(2):370-82.

[60] Tong YX, Kucukdeger E, Halper J, Cesewski E, Karakozoff E, Haring AP, et al. Low-cost sensor-integrated 3D-printed personalized prosthetic hands for children with amniotic band syndrome: A case study in sensing pressure distribution on an anatomical human-machine interface (AHMI) using 3D-printed conformal electrode arrays. Plos One. 2019;14(3).

[61] Laszczak P, Jiang L, Bader DL, Moser D, Zahedi S. Development and validation of a 3D-printed interfacial stress sensor for prosthetic applications. Medical engineering & physics. 2015;37(1):132-7.

[62] Kaur G, Adhikari R, Cass P, Bown M, Gunatillake P. Electrically conductive polymers and composites for biomedical applications. Rsc Advances. 2015;5(47):37553-67.

[63] Chortos A, Liu J, Bao Z. Pursuing prosthetic electronic skin. Nature materials. 2016;15(9):937-50.

[64] Wang HB, Totaro M, Beccai L. Toward Perceptive Soft Robots: Progress and Challenges. Adv Sci. 2018;5(9).

[65] Amjadi M, Kyung K-U, Park I, Sitti M. Stretchable, Skin-Mountable, and Wearable Strain Sensors and Their Potential Applications: A Review. Advanced Functional Materials. 2016;26(11):1678-98.

[66] Gupta TK, Singh BP, Mathur RB, Dhakate SR. Multi-walled carbon nanotube–graphene–polyaniline multiphase nanocomposite with superior electromagnetic shielding effectiveness. Nanoscale. 2014;6(2):842-51.

[67] Makireddi S, S S, Kosuri G, Varghese FV, Balasubramaniam K. Electro-elastic and piezoresistive behavior of flexible MWCNT/PMMA nanocomposite films prepared by solvent casting method for structural health monitoring applications. Composites Science and Technology. 2015;118:101-7.

[68] Rice JA, Mechitov K, Sim S-H, Nagayama T, Jang S, Kim R, et al. Flexible smart sensor framework for autonomous structural health monitoring. Smart structures and Systems. 2010;6(5-6):423-38.

[69] Stoppa M, Chiolerio A. Wearable Electronics and Smart Textiles: A Critical Review. Sensors-Basel. 2014;14(7):11957-92.

[70] Yamada T, Hayamizu Y, Yamamoto Y, Yomogida Y, Izadi-Najafabadi A, Futaba DN, et al. A stretchable carbon nanotube strain sensor for human-motion detection. Nature Nanotechnology. 2011;6:296.

[71] Atalay A, Sanchez V, Atalay O, Vogt DM, Haufe F, Wood RJ, et al. Batch fabrication of customizable silicone-textile composite capacitive strain sensors for human motion tracking. Advanced Materials Technologies. 2017;2(9):1700136.

[72] Sha F, Cheng X, Li S, Xu D, Huang S, Liu R, et al. Nondestructive evaluation on strain sensing capability of piezoelectric sensors for structural health monitoring. Research in Nondestructive Evaluation. 2017;28(2):61-75.

[73] Hu N, Fukunaga H, Atobe S, Liu Y, Li J. Piezoresistive strain sensors made from carbon nanotubes based polymer nanocomposites. Sensors. 2011;11(11):10691-723.

[74] Amjadi M, Kyung KU, Park I, Sitti M. Stretchable, skin-mountable, and wearable strain sensors and their potential applications: a review. Adv Funct Mater. 2016;26(11):1678-98.

[75] Li J, Bao RR, Tao J, Peng YY, Pan CF. Recent progress in flexible pressure sensor arrays: from design to applications. J Mater Chem C. 2018;6(44):11878-92.

[76] Zhang JH, Chen JX, Li M, Ge YX, Wang TT, Shan P, et al. Design, Fabrication, and Implementation of an Array-Type MEMS Piezoresistive Intelligent Pressure Sensor System. Micromachines-Basel. 2018;9(3).

[77] Zheng YJ, Li YL, Dai K, Wang Y, Zheng GQ, Liu CT, et al. A highly stretchable and stable strain sensor based on hybrid carbon nanofillers/polydimethylsiloxane conductive composites for large human motions monitoring. Composites Science and Technology. 2018;156:276-86.

[78] Kang D, Pikhitsa PV, Choi YW, Lee C, Shin SS, Piao LF, et al. Ultrasensitive mechanical crack-based sensor inspired by the spider sensory system. Nature. 2014;516(7530):222-6.

[79] Du FM, Fischer JE, Winey KI. Effect of nanotube alignment on percolation conductivity in carbon nanotube/polymer composites. Phys Rev B. 2005;72(12).

[80] Goh GL, Agarwala S, Yeong WY. Directed and On-Demand Alignment of Carbon Nanotube: A Review toward 3D Printing of Electronics. Adv Mater Interfaces. 2019;6(4).

[81] Zhang XM, Yang XL, Wang KY. Electrical Conductivity Enhancement of Epoxy by Hybrid Carbon Nanotubes and Self-made Silver Nanoparticles. Fiber Polym. 2019;20(7):1480-5.

[82] Li J, Ma PC, Chow WS, To CK, Tang BZ, Kim JK. Correlations between percolation threshold, dispersion state, and aspect ratio of carbon nanotubes. Adv Funct Mater. 2007;17(16):3207-15.

[83] Amjadi M, Turan M, Clementson CP, Sitti M. Parallel Microcracks-based Ultrasensitive and Highly Stretchable Strain Sensors. ACS Applied Materials & Interfaces. 2016;8(8):5618-26.

[84] Hoang PT, Salazar N, Porkka TN, Joshi K, Liu T, Dickens TJ, et al. Engineering Crack Formation in Carbon Nanotube-Silver Nanoparticle Composite Films for Sensitive and Durable Piezoresistive Sensors. Nanoscale Res Lett. 2016;11.

[85] Park SJ, Kim J, Chu M, Khine M. Flexible Piezoresistive Pressure Sensor Using Wrinkled Carbon Nanotube Thin Films for Human Physiological Signals. Adv Mater Technol-Us. 2018;3(1).

[86] Lee J, Pyo S, Kwon DS, Jo E, Kim W, Kim J. Ultrasensitive Strain Sensor Based on Separation of Overlapped Carbon Nanotubes. Small. 2019;15(12).

[87] Chen Y-F, Li J, Tan Y-J, Cai J-H, Tang X-H, Liu J-H, et al. Achieving highly electrical conductivity and piezoresistive sensitivity in polydimethylsiloxane/multi-walled carbon nanotube

composites via the incorporation of silicon dioxide micro-particles. Composites Science and Technology. 2019;177:41-8.

[88] Zhang S, Liu H, Yang S, Shi X, Zhang D, Shan C, et al. Ultrasensitive and Highly Compressible Piezoresistive Sensor Based on Polyurethane Sponge Coated with a Cracked Cellulose Nanofibril/Silver Nanowire Layer. Acs Appl Mater Inter. 2019;11(11):10922-32.

[89] Liu WL, Jiang HB, Ru Y, Zhang XH, Qiao JL. Conductive Graphene-Melamine Sponge Prepared via Microwave Irradiation. Acs Appl Mater Inter. 2018;10(29):24776-83.

[90] Song Y, Chen HT, Su ZM, Chen XX, Miao LM, Zhang JX, et al. Highly Compressible Integrated Supercapacitor-Piezoresistance-Sensor System with CNT-PDMS Sponge for Health Monitoring. Small. 2017;13(39).

[91] Seshadri DR, Li RT, Voos JE, Rowbottom JR, Alfes CM, Zorman CA, et al. Wearable sensors for monitoring the physiological and biochemical profile of the athlete. NPJ digital medicine. 2019;2(1):1-16.

[92] Yan T, Wang Z, Pan Z-J. Flexible strain sensors fabricated using carbon-based nanomaterials: A review. Current Opinion in Solid State and Materials Science. 2018;22(6):213-28.

[93] Zheng Y, Li Y, Dai K, Wang Y, Zheng G, Liu C, et al. A highly stretchable and stable strain sensor based on hybrid carbon nanofillers/polydimethylsiloxane conductive composites for large human motions monitoring. Composites Science and Technology. 2018;156:276-86.

[94] Ge G, Huang W, Shao J, Dong X. Recent progress of flexible and wearable strain sensors for human-motion monitoring. Journal of Semiconductors. 2018;39(1):011012.

[95] Park JJ, Hyun WJ, Mun SC, Park YT, Park OO. Highly stretchable and wearable graphene strain sensors with controllable sensitivity for human motion monitoring. ACS applied materials & interfaces. 2015;7(11):6317-24.

[96] Yu G, Hu J, Tan J, Gao Y, Lu Y, Xuan F. A wearable pressure sensor based on ultra-violet/ozone microstructured carbon nanotube/polydimethylsiloxane arrays for electronic skins. Nanotechnology. 2018;29(11):115502.

[97] Sun B, Long Y-Z, Chen Z-J, Liu S-L, Zhang H-D, Zhang J-C, et al. Recent advances in flexible and stretchable electronic devices via electrospinning. J Mater Chem C. 2014;2(7):1209-19.

[98] Lan L, Yin T, Jiang C, Li X, Yao Y, Wang Z, et al. Highly conductive 1D-2D composite film for skin-mountable strain sensor and stretchable triboelectric nanogenerator. Nano Energy. 2019;62:319-28.

[99] Yang Y, Cao Z, He P, Shi L, Ding G, Wang R, et al. Ti3C2Tx MXene-graphene composite films for wearable strain sensors featured with high sensitivity and large range of linear response. Nano Energy. 2019;66:104134.

[100] Gogurla N, Roy B, Park J-Y, Kim S. Skin-contact actuated single-electrode protein triboelectric nanogenerator and strain sensor for biomechanical energy harvesting and motion sensing. Nano Energy. 2019;62:674-81.

[101] Pan Z, Yang J, Li L, Gao X, Kang L, Zhang Y, et al. All-in-one stretchable coaxial-fiber strain sensor integrated with high-performing supercapacitor. Energy Storage Materials. 2020;25:124-30.

[102] Pegan JD, Zhang J, Chu M, Nguyen T, Park S-J, Paul A, et al. Skin-mountable stretch sensor for wearable health monitoring. Nanoscale. 2016;8(39):17295-303.

[103] Amjadi M, Yoon YJ, Park I. Ultra-stretchable and skin-mountable strain sensors using carbon nanotubes–Ecoflex nanocomposites. Nanotechnology. 2015;26(37):375501.

[104] Dhakar L, Pitchappa P, Tay FEH, Lee C. An intelligent skin based self-powered finger motion sensor integrated with triboelectric nanogenerator. Nano Energy. 2016;19:532-40.

[105] Chen J, Zheng J, Gao Q, Zhang J, Zhang J, Omisore OM, et al. Polydimethylsiloxane (PDMS)-based flexible resistive strain sensors for wearable applications. Applied Sciences. 2018;8(3):345.

[106] Lu N, Lu C, Yang S, Rogers J. Highly sensitive skin-mountable strain gauges based entirely on elastomers. Advanced Functional Materials. 2012;22(19):4044-50.

[107] Yamada T, Hayamizu Y, Yamamoto Y, Yomogida Y, Izadi-Najafabadi A, Futaba DN, et al. A stretchable carbon nanotube strain sensor for human-motion detection. Nature nanotechnology. 2011;6(5):296.

[108] Johnston ID, McCluskey DK, Tan CKL, Tracey MC. Mechanical characterization of bulk Sylgard 184 for microfluidics and microengineering. J Micromech Microeng. 2014;24(3).

[109] Mai H, Mutlu R, Tawk C, Alici G, Sencadas V. Ultra-stretchable MWCNT–Ecoflex piezoresistive sensors for human motion detection applications. Composites Science and Technology. 2019;173:118-24.

[110] Heikenfeld J, Jajack A, Rogers J, Gutruf P, Tian L, Pan T, et al. Wearable sensors: modalities, challenges, and prospects. Lab on a Chip. 2018;18(2):217-48.

[111] Shintake J, Piskarev E, Jeong SH, Floreano D. Ultrastretchable Strain Sensors Using Carbon Black-Filled Elastomer Composites and Comparison of Capacitive Versus Resistive Sensors. Advanced Materials Technologies. 2018;3(3):1700284.

[112] Lim GH, Lee NE, Lim B. Highly sensitive, tunable, and durable gold nanosheet strain sensors for human motion detection. J Mater Chem C. 2016;4(24):5642-7.

[113] Shintake J, Piskarev E, Jeong SH, Floreano D. Ultrastretchable strain sensors using carbon black-filled elastomer composites and comparison of capacitive versus resistive sensors. Advanced Materials Technologies. 2018;3(3):1700284.

[114] Oliva-Avilés AI, Avilés F, Sosa V. Electrical and piezoresistive properties of multi-walled carbon nanotube/polymer composite films aligned by an electric field. Carbon. 2011;49(9):2989-97.

[115] Rahman R, Servati P. Effects of inter-tube distance and alignment on tunnelling resistance and strain sensitivity of nanotube/polymer composite films. Nanotechnology. 2012;23(5):055703.

[116] Parmar K, Mahmoodi M, Park C, Park SS. Effect of CNT alignment on the strain sensing capability of carbon nanotube composites. Smart materials and structures. 2013;22(7):075006.

[117] Chen J, Guo H, He X, Liu G, Xi Y, Shi H, et al. Enhancing performance of triboelectric nanogenerator by filling high dielectric nanoparticles into sponge PDMS film. ACS applied materials & interfaces. 2016;8(1):736-44.

[118] Shin JH, Heo J-H, Jeon S, Park JH, Kim S, Kang H-W. Bio-inspired hollow PDMS sponge for enhanced oil–water separation. Journal of hazardous materials. 2019;365:494-501.

[119] Song Y, Chen H, Su Z, Chen X, Miao L, Zhang J, et al. Highly compressible integrated supercapacitor–piezoresistance-sensor system with CNT–PDMS sponge for health monitoring. Small. 2017;13(39):1702091.

[120] Francis AP, Devasena T. Toxicity of carbon nanotubes: A review. Toxicology and industrial health. 2018;34(3):200-10.

[121] Chen J, Zhang W, Wan Z, Li S, Huang T, Fei Y. Oil spills from global tankers: Status review and future governance. Journal of Cleaner Production. 2019;227:20-32.

[122] Ferguson A, Solo-Gabriele H, Mena K. Assessment for oil spill chemicals: Current knowledge, data gaps, and uncertainties addressing human physical health risk. Marine pollution bulletin. 2020;150:110746.

[123] Ekperusi AO, Onyena AP, Akpudo MY, Peter CC, Akpoduado CO, Ekperusi OH. In-situ burning as an oil spill control measure and its effect on the environment. SPE Nigeria Annual International Conference and Exhibition: Society of Petroleum Engineers; 2019.

[124] McKinney K, Caplis J, DeVitis D, Van Dyke K. Evaluation of oleophilic skimmer performance in diminishing oil slick thicknesses. International Oil Spill Conference Proceedings: International Oil Spill Conference; 2017. p. 1366-81.

[125] Wadsworth T. Comparison and Assessment of Waste Generated during Oil Spills. International Oil Spill Conference Proceedings: American Petroleum Institute; 2014. p. 1647-58.

[126] Hadji EM, Fu B, Abebe A, Bilal HM, Wang J. Sponge-based materials for oil spill cleanups: A review. Frontiers of Chemical Science and Engineering. 2020;14(5):749-62.

[127] Ge J, Zhao HY, Zhu HW, Huang J, Shi LA, Yu SH. Advanced sorbents for oil-spill cleanup: recent advances and future perspectives. Advanced materials. 2016;28(47):10459-90.

[128] Yang Y, Deng Y, Tong Z, Wang C. Multifunctional foams derived from poly (melamine formaldehyde) as recyclable oil absorbents. Journal of Materials Chemistry A. 2014;2(26):9994-9.

[129] Turco A, Malitesta C, Barillaro G, Greco A, Maffezzoli A, Mazzotta E. A magnetic and highly reusable macroporous superhydrophobic/superoleophilic PDMS/MWNT nanocomposite for oil sorption from water. Journal of Materials Chemistry A. 2015;3(34):17685-96.

[130] Gui X, Zeng Z, Lin Z, Gan Q, Xiang R, Zhu Y, et al. Magnetic and highly recyclable macroporous carbon nanotubes for spilled oil sorption and separation. ACS applied materials & interfaces. 2013;5(12):5845-50.

[131] Ge J, Shi L-A, Wang Y-C, Zhao H-Y, Yao H-B, Zhu Y-B, et al. Joule-heated graphene-wrapped sponge enables fast clean-up of viscous crude-oil spill. Nature Nanotechnology. 2017;12(5):434-40.

[132] Wu MB, Huang S, Liu TY, Wu J, Agarwal S, Greiner A, et al. Compressible Carbon Sponges from Delignified Wood for Fast Cleanup and Enhanced Recovery of Crude Oil Spills by Joule Heat and Photothermal Effect. Advanced Functional Materials. 2020:2006806.

[133] Wu X, Lei Y, Li S, Huang J, Teng L, Chen Z, et al. Photothermal and Joule heating-assisted thermal management sponge for efficient cleanup of highly viscous crude oil. Journal of Hazardous Materials.403:124090.

[134] Xie A, Chen Y, Cui J, Lang J, Li C, Yan Y, et al. Facile and green fabrication of superhydrophobic sponge for continuous oil/water separation from harsh environments. Colloids and Surfaces A: Physicochemical and Engineering Aspects. 2019;563:120-9.

[135] Xu J, Cao R, Li M, Chen G, Tian J. Superhydrophobic and superoleophilic cuttlebone with an inherent lamellar structure for continuous and effective oil spill cleanup. Chemical Engineering Journal. 2020:127596.

[136] Kong Z, Wang J, Lu X, Zhu Y, Jiang L. In situ fastening graphene sheets into a polyurethane sponge for the highly efficient continuous cleanup of oil spills. Nano Research. 2017;10(5):1756-66.

[137] Chen X, Weibel JA, Garimella SV. Continuous oil–water separation using polydimethylsiloxane-functionalized melamine sponge. Industrial & Engineering Chemistry Research. 2016;55(12):3596-602.

[138] Yan C, Ji Z, Ma S, Wang X, Zhou F. 3D printing as feasible platform for on-site building oil-skimmer for oil collection from spills. Advanced Materials Interfaces. 2016;3(13):1600015.

[139] Liu Z, Wang X, Gao M, Song J, Huang L, Liu J, et al. Unpowered oil absorption by a wettability sponge based oil skimmer. RSC advances. 2016;6(91):88001-9.

[140] Kim T, Lee JS, Lee G, Seo DK, Baek Y, Yoon J, et al. Autonomous graphene vessel for suctioning and storing liquid body of spilled oil. Scientific reports. 2016;6:22339.

[141] Xu X, Mredha MTI, Cui J, Vlassak JJ, Jeon I. Hydrogel bowls for cleaning oil spills on water. Water research. 2018;145:640-9.

[142] Xue C-H, Li Y-R, Hou J-L, Zhang L, Ma J-Z, Jia S-T. Self-roughened superhydrophobic coatings for continuous oil–water separation. Journal of Materials Chemistry A. 2015;3(19):10248-53.

[143] Deng D, Prendergast DP, MacFarlane J, Bagatin R, Stellacci F, Gschwend PM. Hydrophobic meshes for oil spill recovery devices. ACS applied materials & interfaces. 2013;5(3):774-81.

[144] Cheng M, Ju G, Jiang C, Zhang Y, Shi F. Magnetically directed clean-up of underwater oil spills through a functionally integrated device. Journal of Materials Chemistry A. 2013;1(43):13411-6.

[145] Herren B, Larson P, Saha MC, Liu YT. Enhanced Electrical Conductivity of Carbon Nanotube- Based Elastomer Nanocomposites Prepared by Microwave Curing. Polymers-Basel. 2019;11(7).

[146] Herren B, Saha MC, Liu Y. Carbon Nanotube-Based Piezoresistive Sensors Fabricated by Microwave Irradiation. Advanced Engineering Materials. 2019:1901068.

[147] Song YS, Youn JR. Influence of dispersion states of carbon nanotubes on physical properties of epoxy nanocomposites. Carbon. 2005;43(7):1378-85.

[148] Chang JF, Liang GZ, Gu AJ, Cai SD, Yuan L. The production of carbon nanotube/epoxy composites with a very high dielectric constant and low dielectric loss by microwave curing. Carbon. 2012;50(2):689-98.

[149] Luo W, Charara M, Saha MC, Liu Y. Fabrication and characterization of porous CNF/PDMS nanocomposites for sensing applications. Applied Nanoscience. 2019;9(6):1309–17.

[150] Rangari VK, Bhuyan MS, Jeelani S. Microwave processing and characterization of EPON 862/CNT nanocomposites. Mater Sci Eng B-Adv. 2010;168(1-3):117-21.

[151] Herren B, Saha MC, Altan MC, Liu Y. Development of Ultrastretchable and Skin Attachable Nanocomposites for Human Motion Monitoring via Embedded 3D Printing. Composites Part B: Engineering. 2020:108224.

[152] Chang F-Y, Wang R-H, Yang H, Lin Y-H, Chen T-M, Huang S-J. Flexible strain sensors fabricated with carbon nano-tube and carbon nano-fiber composite thin films. Thin Solid Films. 2010;518(24):7343-7.

[153] Hu N, Karube Y, Arai M, Watanabe T, Yan C, Li Y, et al. Investigation on sensitivity of a polymer/carbon nanotube composite strain sensor. Carbon. 2010;48(3):680-7.

[154] Lozano-Pérez C, Cauich-Rodríguez JV, Avilés F. Influence of rigid segment and carbon nanotube concentration on the cyclic piezoresistive and hysteretic behavior of multiwall carbon nanotube/segmented polyurethane composites. Composites Science and Technology. 2016;128:25-32.

[155] Panozzo F, Zappalorto M, Quaresimin M. Analytical model for the prediction of the piezoresistive behavior of CNT modified polymers. Composites Part B: Engineering. 2017;109:53-63.

[156] Martin CA, Sandler JKW, Shaffer MSP, Schwarz MK, Bauhofer W, Schulte K, et al. Formation of percolating networks in multi-wall carbon-nanotube–epoxy composites. Composites Science and Technology. 2004;64(15):2309-16.

[157] Lewicki JP, Rodriguez JN, Zhu C, Worsley MA, Wu AS, Kanarska Y, et al. 3D-printing of meso-structurally ordered carbon fiber/polymer composites with unprecedented orthotropic physical properties. Scientific reports. 2017;7(1):1-14.

[158] Ren M, Zhou Y, Wang Y, Zheng G, Dai K, Liu C, et al. Highly stretchable and durable strain sensor based on carbon nanotubes decorated thermoplastic polyurethane fibrous network with aligned wave-like structure. Chemical Engineering Journal. 2019;360:762-77.

[159] Gao J, Li B, Huang X, Wang L, Lin L, Wang H, et al. Electrically conductive and fluorine free superhydrophobic strain sensors based on SiO2/graphene-decorated electrospun nanofibers for human motion monitoring. Chemical Engineering Journal. 2019;373:298-306.

[160] Zhang S, Sun K, Liu H, Chen X, Zheng Y, Shi X, et al. Enhanced Piezoresistive Performance of Conductive WPU/CNT Composite Foam Through Incorporating Brittle Cellulose Nanocrystal. Chemical Engineering Journal. 2020:124045.

[161] Duan L, D'hooge DR, Cardon L. Recent progress on flexible and stretchable piezoresistive strain sensors: from design to application. Progress in Materials Science. 2019:100617.

[162] Li CH, Guan GY, Reif R, Huang ZH, Wang RKK. Determining elastic properties of skin by measuring surface waves from an impulse mechanical stimulus using phase-sensitive optical coherence tomography. J R Soc Interface. 2012;9(70):831-41.

[163] Giffney T, Bejanin E, Kurian AS, Travas-Sejdic J, Aw K. Highly stretchable printed strain sensors using multi-walled carbon nanotube/silicone rubber composites. Sensors and Actuators A: Physical. 2017;259:44-9.

[164] Lam C-w, James JT, McCluskey R, Arepalli S, Hunter RL. A review of carbon nanotube toxicity and assessment of potential occupational and environmental health risks. Critical reviews in toxicology. 2006;36(3):189-217.

[165] Herren B, Webster V, Davidson E, Saha MC, Altan MC, Liu Y. PDMS Sponges with Embedded Carbon Nanotubes as Piezoresistive Sensors for Human Motion Detection. Nanomaterials. 2021;11(7):1740.

[166] Li Q, Duan T, Shao J, Yu H. Fabrication method for structured porous polydimethylsiloxane (PDMS). Journal of Materials Science. 2018;53(16):11873-82.

[167] Lee KY, Chun J, Lee JH, Kim KN, Kang NR, Kim JY, et al. Hydrophobic sponge structure-based triboelectric nanogenerator. Advanced materials. 2014;26(29):5037-42.

[168] King M, Baragwanath A, Rosamond M, Wood D, Gallant A. Porous PDMS force sensitive resistors. Procedia Chemistry. 2009;1(1):568-71.

[169] Wang J, Guo J, Si P, Cai W, Wang Y, Wu G. Polydopamine-based synthesis of an In (OH) 3–PDMS sponge for ammonia detection by switching surface wettability. RSC advances. 2016;6(6):4329-34.

[170] Zhang S, Guo J, Ma X, Peng X, Qiu Z, Ying J, et al. Smart PDMS sponge with switchable pH-responsive wetting surface for oil/water separation. New Journal of Chemistry. 2017;41(17):8940-6.

[171] Yu C, Yu C, Cui L, Song Z, Zhao X, Ma Y, et al. Facile Preparation of the Porous PDMS Oil-Absorbent for Oil/Water Separation. Advanced Materials Interfaces. 2017;4(3):1600862.

[172] Pang Y, Tian H, Tao L, Li Y, Wang X, Deng N, et al. Flexible, highly sensitive, and wearable pressure and strain sensors with graphene porous network structure. ACS applied materials & interfaces. 2016;8(40):26458-62.

[173] Li J, Liu X, Crook JM, Wallace GG. Development of a porous 3D graphene-PDMS scaffold for improved osseointegration. Colloids and Surfaces B: Biointerfaces. 2017;159:386-93.

[174] Zhao X, Wang T, Li Y, Huang L, Handschuh-Wang S. Polydimethylsiloxane/nanodiamond composite sponge for enhanced mechanical or wettability performance. Polymers-Basel. 2019;11(6):948.

[175] Savolainen K, Pylkkänen L, Norppa H, Falck G, Lindberg H, Tuomi T, et al. Nanotechnologies, engineered nanomaterials and occupational health and safety–A review. Safety science. 2010;48(8):957-63.

[176] Choi S-J, Kwon T-H, Im H, Moon D-I, Baek DJ, Seol M-L, et al. A polydimethylsiloxane (PDMS) sponge for the selective absorption of oil from water. ACS applied materials & interfaces. 2011;3(12):4552-6.

[177] Tran DN, Kabiri S, Sim TR, Losic D. Selective adsorption of oil–water mixtures using polydimethylsiloxane (PDMS)–graphene sponges. Environmental Science: Water Research & Technology. 2015;1(3):298-305.

[178] Rattanaumpa T, Naowanon W, Amnuaypanich S, Amnuaypanich S. Polydimethylsiloxane sponges incorporated with mesoporous silica nanoparticles (PDMS/H-MSNs) and their selective solvent absorptions. Industrial & Engineering Chemistry Research. 2019;58(46):21142-54.

[179] Liu L, Lei J, Li L, Zhang R, Mi N, Chen H, et al. A facile method to fabricate the superhydrophobic magnetic sponge for oil-water separation. Materials Letters. 2017;195:66-70.

[180] Halake K, Bae S, Lee J, Cho Y, Jo H, Heo J, et al. Strategies for Fabrication of Hydrophobic Porous Materials Based on Polydimethylsiloxane for Oil-Water Separation. Macromolecular Research. 2019;27(2):109-14.

[181] Zhang X, Liu D, Ma Y, Nie J, Sui G. Super-hydrophobic graphene coated polyurethane (GN@ PU) sponge with great oil-water separation performance. Applied Surface Science. 2017;422:116-24.

[182] Bentini R, Pola A, Rizzi LG, Athanassiou A, Fragouli D. A highly porous solvent free PVDF/expanded graphite foam for oil/water separation. Chemical Engineering Journal. 2019;372:1174-82.

[183] Zhang A, Chen M, Du C, Guo H, Bai H, Li L. Poly (dimethylsiloxane) oil absorbent with a three-dimensionally interconnected porous structure and swellable skeleton. ACS applied materials & interfaces. 2013;5(20):10201-6.

[184] Zhang L, Zhang Y, Chen P, Du W, Feng X, Liu B-F. Paraffin oil based soft-template approach to fabricate reusable porous pdms sponge for effective oil/water separation. Langmuir. 2019;35(34):11123-31.

[185] Singh S, Jelinek R. Solar-mediated oil-spill cleanup by a carbon dot-polyurethane sponge. Carbon. 2020;160:196-203.

[186] Guo Z, Long B, Gao S, Luo J, Wang L, Huang X, et al. Carbon nanofiber based superhydrophobic foam composite for high performance oil/water separation. Journal of Hazardous Materials. 2021;402:123838.

[187] Nguyen DD, Tai N-H, Lee S-B, Kuo W-S. Superhydrophobic and superoleophilic properties of graphene-based sponges fabricated using a facile dip coating method. Energy & Environmental Science. 2012;5(7):7908-12.

[188] Chang J, Shi Y, Wu M, Li R, Shi L, Jin Y, et al. Solar-assisted fast cleanup of heavy oil spills using a photothermal sponge. Journal of Materials Chemistry A. 2018;6(19):9192-9.

[189] Gong C, Lao J, Wang B, Li X, Li G, Gao J, et al. Fast and all-weather cleanup of viscous crude-oil spills with Ti 3 C 2 TX MXene wrapped sponge. Journal of Materials Chemistry A. 2020;8(38):20162-7.

[190] Phanthong P, Reubroycharoen P, Kongparakul S, Samart C, Wang Z, Hao X, et al. Fabrication and evaluation of nanocellulose sponge for oil/water separation. Carbohydrate polymers. 2018;190:184-9.

[191] Guselnikova O, Barras A, Addad A, Sviridova E, Szunerits S, Postnikov P, et al. Magnetic polyurethane sponge for efficient oil adsorption and separation of oil from oil-in-water emulsions. Separation and Purification Technology. 2020;240:116627.

[192] Peng L, Yuan S, Yan G, Yu P, Luo Y. Hydrophobic sponge for spilled oil absorption. Journal of Applied Polymer Science. 2014;131(20).

[193] Liu Y, Ma J, Wu T, Wang X, Huang G, Liu Y, et al. Cost-effective reduced graphene oxide-coated polyurethane sponge as a highly efficient and reusable oil-absorbent. ACS applied materials & interfaces. 2013;5(20):10018-26.

[194] Meyer P, Schmidt W, Delgado J-e, Devitis D, Haugstad E, Potter S, et al. Application of the American Society of Testing and Materials'(ASTM) New Skimmer Test Protocol. 2009.